Artificial Nonlinear Stiffness and Artificial Vacuum for Wide-Bandwidth High-Q Resonance Behavior

by

Yingsong Han

A dissertation submitted to the Graduate Faculty of
Auburn University
in partial fulfillment of the
requirements for the Degree of
Doctor of Philosophy

Auburn, Alabama
Aug 5, 2023

Keywords: Performance control, PODMEMS, electrostatic force feedback control, artificial stiffness, artificial damping, thermal drift

Approved by

Jason V. Clark, Chair, Visiting Professor, Electrical and Computer Engineering
John Y. Hung, Professor Emeritus, Electrical and Computer Engineering
Robert N. Dean, McWane Endowed Professor, Electrical and Computer Engineering
Masoud Mahjouri-Samani, Assistant Professor, Electrical and Computer Engineering

Abstract

This dissertation explores the use of electrostatic force feedback to generate artificial performance characteristics in a microdevice that would otherwise not be possible. As a test case, a non-vacuumed microresonator that is limited to small-amplitude linear-spring displacements and subject to thermal drift is transformed by electrostatic force feedback to behave as if it were in a vacuum and subject to highly nonlinear spring displacements that are insensitive to thermal drift. Thermal drift is the most significant challenge faced by microscale vibratory gyroscopes.

A real-time performance-control technology is presented for correcting or manipulating the performance of microelectromechanical systems (MEMS) devices that are subject to process variations, temperature fluctuations, packaging stresses, or limited by manufacturing materials or geometry. This is done by using electrostatic force feedback to artificially increase or decrease the effective mass, damping, or stiffness of the MEMS device.

When subject to identical excitations, process variations in the fabrication of MEMS devices cause two identically designed MEMS devices to perform differently, such as having different resonance frequencies. A shift in resonance frequency due to a variation in temperature will cause a frequency mismatch between the electrically driven excitation frequency and structural resonance frequency. This variation in temperature results in small changes in geometry, material properties, and packaging stress, causing significant drift in sensor reading from the MEMS device. For instance, readings of a three-axis vibratory MEMS gyroscope resting on a stationary table will drift by incorrectly sensing motion in the stationary table. Efforts by others to reduce drift sensitivity include using temperature-dependent drive frequency to match the drift of structural resonance frequency, creating structural designs that are less

sensitive to temperature variations, encapsulating the MEMS in a thermal reservoir to maintain a constant temperature, etc.

Applying our real-time performance-control technology to our test case, we address the abovementioned problems as follows. To ensure all identically fabricated devices can achieve identical resonance frequencies, the devices are structurally designed to have a resonance frequency that is below the desired resonance frequency. Two electrostatic force feedbacks are applied to each device. The first feedback (proportional to negative velocity) greatly narrows the bandwidth and increases the resonance amplitude, i.e. an artificial vacuum for a high-quality factor. The second feedback (proportional to cubed displacement) bends the amplitude response curve over the desired resonance frequency; i.e. an artificial nonlinear stiffness for wide bandwidth within 3dB of the preferred amplitude. Ultimately, this enables all devices to resonate precisely at the applied electronic excitation frequency and be insensitive to the process variations and thermal drift that would have overwise affected their structural resonance frequencies. This real-time performance-control technology is called performance-on-demand MEMS, or PODMEMS.

Our analytical and simulation results show that the effective stiffness, quality factor, and nonlinearity of the device can be easily tuned by just changing the gain of the feedback circuit. While applying these technologies to the application of a low-cost MEMS gyroscope, the result shows that for a temperature variation of 80^{o}C, the output amplitude of the gyro is only attenuated by 0.4dB, which is 94.4dB smaller than the gyro without the feedback control.

Acknowledgments

I would like to express my deepest gratitude and appreciation to all those who have supported and contributed to the successful completion of this Ph.D. dissertation. Their guidance, encouragement, and assistance have been invaluable throughout this journey.

First and foremost, I am profoundly grateful to my advisor, Prof. Jason V. Clark, for his unwavering support, patience, and expertise. His mentorship and insightful feedback have been instrumental in shaping the direction and quality of this research. I am truly fortunate to have had such an exceptional mentor who constantly challenged me to push the boundaries of my knowledge.

I extend my heartfelt thanks to the members of my dissertation committee, Prof. Robert N. Dean, Prof. John Y. Hung, and Prof. Masoud Mahjouri-Samani for their valuable input, critical evaluation, and constructive suggestions. Their expertise in their respective fields greatly enriched the content of this dissertation and broadened my perspective on the subject matter.

Finally, I would like to express my heartfelt gratitude to my spouse, Xiaodan, and my family for their unwavering love, encouragement, and understanding throughout this Ph.D. journey. Their belief in my abilities and their constant support has been the driving force behind my perseverance and determination to reach this milestone.

Table of Contents

Abstract ii

Acknowledgments iv

List of Tables viii

List of Figures ix

List of Abbreviations xi

Chapter 1 Introduction 1

Chapter 2 Survey of Literature 6

2.1 Process Variation Compensation 6

2.1.1 Mechanical Tuning Methods 6

2.1.2 Electrical Tuning Methods 8

2.2 Thermal Drift Compensation 9

2.2.1 Passive Compensation Methods 9

2.2.2 Active Compensation Methods 11

2.3 Summary 12

Chapter 3 PODMEMS Theory 14

3.1. Steady-State Analysis of Linear PODMEMS 14

3.2. Steady-State Analysis of Nonlinear PODMEMS 18

3.3. Stability Analysis 21

3.4. Conclusion 24

Chapter 4 Artificial Linear Stiffness 25

4.1 Analytical Model 26

4.1.1 MEMS resonator 26

4.1.2 Artificial Stiffness Tunning Principle 29
4.2 Simulation 34
4.3 Conclusion 38
Chapter 5 Artificial Nonlinear Stiffness 40
5.1 The design of the artificial nonlinear stiffness resonator system 40
5.2 Simulation 44
5.2.1 Transient behavior 45
5.2.2 The frequency characteristic 47
5.2.3 Thermal drift 48
5.3 Conclusion 49
Chapter 6 Artificial Vacuum and Nonlinear Stiffness 50
6.1. Electronic feedback components for artificial nonlinear stiffness 54
6.2. System integration verification 65
6.3. Nonlinear stiffness Results 67
6.4. Conclusion 70
Chapter 7 Application to Thermal Drift 71
7.1. Background 72
7.2. Vibratory MEMS gyroscope test case 77
7.3. Nonlinear feedback and frequency match control system 79
7.3.1. Electrostatic Force Feedback Circuit 79
7.3.2 Generating nonlinear stiffness behavior in the drive mode 81
7.3.2. Generating low damping behavior in the drive mode 84
7.3.3. Excitation of the drifting sense mode 85

7.3.4. Determining the angular rate 89
7.4. Simulation 91
7.5. Conclusion..... 103
Chapter 8 Conclusion and Future Work 105
Bibliography 108

List of Tables

Table 4.1 Nomenclature of Artificial Linear Stiffness System..... 27

Table 6.1 Nomenclature of Artificial Nonlinear Stiffness and Vacuum System 51

List of Figures

Figure 3.1: MEMS + performance controller 14

Figure 3.2: Frequency response of the nonlinear system 20

Figure 3.3: The stability domains of PODMEMS 24

Figure 4.1: Layout of the MEMS resonator 26

Figure 4.2: COMSOL simulation of MEMS resonator 29

Figure 4.3: Block diagram of the stiffness tunable MEMS resonator 32

Figure 4.4: Simulation setup in MATLAB/Simulink 35

Figure 4.5: Step response of the system when with and without electrical stiffness tunning 36

Figure 4.6: Frequency response of the system with different electrical stiffness value 37

Figure 4.7: Frequency response of the system with small latency 37

Figure 4.8: Frequency response of the system with large latency 38

Figure 5.1: Block diagram of the stiffness tunable MEMS resonator 41

Figure 5.2: Simulation setup in Simulink 44

Figure 5.3: Transient simulation result 45

Figure 5.4: Result of TA when sweeping the driving frequency 46

Figure 5.5: Frequency responses of the nonlinear PODMEMS 47

Figure 5.6: Frequency response of linear and nonlinear Simulink models of PODMEMS 49

Figure 6.1: The frequency responses of linear and nonlinear MEMS resonator 54

Figure 6.2: System block diagram of the artificial damping and nonlinear stiffness system 57

Figure 6.3: MEMS equivalent circuit 58

Figure 6.4: Transimpedance amplifier (TIA) component 59

Figure 6.5: Integrator component 60

Figure 6.6: Cubic component 61
Figure 6.7: Parasitic component 62
Figure 6.8: Square root component 63
Figure 6.9: Square component 64
Figure 6.10: TA result of the artificial nonlinear stiffness and vacuum system 65
Figure 6.11: Verification of TA characteristic 67
Figure 6.12: Resonance frequency shift due to change in temperature 69
Figure 6.13: Frequency response of linear and nonlinear PODMEMS with thermal drift 70
Figure 7.1: Quality factor versus cost for MEMS gyroscopes 73
Figure 7.2: Lumped spring-mass-damper model of MEMS gyroscope 77
Figure 7.3: System block diagram of MEMS gyroscope with control system 81
Figure 7.4: Nonlinear stiffness feedback circuit 83
Figure 7.5: Damping feedback circuit. 84
Figure 7.6: PLL module 85
Figure 7.7: SIMULINK realization of the system 91
Figure 7.8: Result of VCO output frequency vs. time. 94
Figure 7.9: Displacement trajectory of nonlinear drive mode vs. time 95
Figure 7.10: Frequency responses of the drive mode and sense mode 99
Figure 7.11(a): Percentage output voltage amplitude attenuation vs. angular rate input 101
Figure 7.11(b): Percentage output voltage amplitude attenuation vs. angular rate input 102
Figure 7.12: Percentage output amplitude attenuation vs. nonlinear feedback voltage 103

List of Abbreviations

ARW	Angle Random Walk
BJT	Bipolar Junction Transistor
BW	Band Width
CCII	Current Conveyor II
CVD	Chemical Vapor Deposition
HRG	Hemispherical Resonator Gyroscope
MEMS	Micro Electro-mechanical Systems
PLL	Phase Locked Loop
POD	Performance of Demand
PVD	Physical Vapor Deposition
Q	Quality Factor
SNR	Signal-to-Noise Ratio
TA	Transient Analysis
TCEM	Temperature Coefficient of Elastic Modulus
TCF	Temperature Coefficient of Frequency
TCSF	Temperature Coefficient of Scale Factor
TDB	Temperature Drift Bias
WNGR	Wide Narrow Gap Rati

Chapter 1

Introduction

Since microelectromechanical systems (MEMS) often generate small electrostatic forces and small static deflections, resonance is often used to achieve larger deflections for improved signal-to-noise ratios (SNR) for greater sensitivities. Examples of MEMS devices that use resonance include filters, gyroscopes, mass sensors, timers, etc. The resonance frequency of a MEMS device most significantly depends on the structure's geometric design and material properties. Nevertheless, due to the variations in fabrication processing, packaging, and ambient conditions, the identically-designed and fabricated devices that are subject to identical excitation will perform differently.

The conventional methods of tuning the resonant frequency of MEMS resonators due to process variation have primarily involved post-processing with mechanical techniques or electrical tuning techniques. The mechanical tuning methods can be further divided into additive methods and subtractive methods. The additive methods can be achieved by deposition [1], surface coating [2], and electroplating [3]. In [4], through selective polysilicon deposition, the cross-section of a suspension beam is increased from 6 to $9.4\mu m^2$, which results in the resonate frequency increased by 1.96% from its initial value of 86.6kHz. Different from additive methods, subtractive methods use chemical etching [5], laser ablation [6], ion milling [7], and mechanical milling [8] methods to remove material from the resonator to change the stiffness. In [9], the resonant frequency of the vibratory MEMS gyroscope is changed from 3200Hz to 3209Hz by trimming the mass with laser trimming. On the other hand, electrical tuning techniques can be generally divided into categories of electrostatic actuation and feedback control. The electrical

actuation methods are achieved by applying an electrostatic force to the resonator, causing a deflection and thereby altering the effective stiffness. By varying the voltage applied to the electrodes, the electrostatic force can be adjusted, enabling tunability of the resonator's stiffness [10]–[12]. In [13], by applying a 14.903V electrostatic-tuning voltage to the comb-drive MEMS gyroscope, the mismatch frequency of 497Hz between the drive and sense mode is eliminated, which results in mechanical sensitivity increased by 238.9%. While the electrostatic actuation methods can tune the stiffness by changing the applied voltages, feedback control methods provide more dynamic flexibility, which involves sensing the displacement or frequency response of the resonator and employing feedback control to adjust the actuation forces accordingly [14]–[16]. In [17], the displacement feedback control is adopted to tune the mode mismatching of a DSP-based MEMS gyroscope. As a result, the mode mismatching is reduced to less than 0.01Hz. While these approaches have proven effective to some extent, they often exhibit limitations in terms of controllability, responsiveness, and adaptability. Therefore, there is a need for innovative techniques that provide greater dynamic control over the stiffness of MEMS resonators.

Another major factor influencing the performance of the MEMS device is the temperature change. Semiconductor conductivity increases with temperature due to increased conduction band charge carriers; ceramic resistor conductivity decreases with increased temperature due to increased scattering, and capacitance increases with temperature due to thermal expansion [18]. MEMS structural volume increases with temperature due to thermal expansion, and Young’s modulus decreases with an increase in temperature due to a widening of the potential wells between lattice sites [19]. For example, [20] reported a shift in the natural frequency of a MEMS accelerometer by 10Hz due to an increase in an ambient temperature of

20^{o}C. Besides, temperature variation will also result in changes in resistor and capacitor values in analog circuits. Such disturbances cause the resonance frequency of the MEMS device to drift. The amplitude at resonance is proportional to the quality factor (Q), which is inversely proportional to the resonance bandwidth (*BW*) for high-Q devices. The initial challenge is to tune the driving frequency with the structural resonance frequency. Thermally induced structural resonance at zero-state can sometimes be sensed to determine the driving frequency. The second challenge is updating the driving frequency to match the drifting structural resonance frequency. For slight mismatches between the drive frequency and structural resonance frequency, there will be significant attenuation in amplitude, resulting in a much smaller SNR. For example, [21] describes a MEMS resonator with $Q > 10^5$, w_r = 911kHz, and BW = 47.7Hz, where a frequency mismatch between the driving force and the structure on the order of a millionth of resonance reduced the amplitude by a factor of 10, below the 3dB cutoff.

Previous methods of addressing thermal drift problems can be divided into two categories: passive compensation and active compensation. The passive compensation methods reduce the influence of temperature fluctuation by selectively choosing the materials [22]–[24], optimizing structural design [25]–[27], and packaging and thermal management [28], [29]. In [30], Hajjam et al. reported a high phosphorus-doped silicon MEMS resonator with thermal drift of frequency down to 1.5 ppm/°C, which is based on the theory that Temperature Coefficient of Elastic Modulus (TCEM) of single-crystal silicon can be compensated by high doping. While in [31], Melamud et al. proposed a Si-SiO2 composite resonator to reduce thermal drift through structural design optimization, where SiO2 covers the surface of the silicon beam to form a composite resonator beam. Because TCEMs of silicon and SiO2 are negative and positive, respectively, the Si-SiO2 composite resonator can realize the passive compensation for the

thermal drift of frequency. On the contrary, the active compensation methods actively sense and adjust the operating parameters of a MEMS resonator to counteract the effects of thermal drift. In [32], the ambient temperature of the piezoelectric MEMS resonator is sensed by measuring frequency difference between the two operating modes of the resonator, which is then used as the feedback control signal for the micro oven. The measured frequency stability is less than ±400 ppb over a wide temperature range from -40^{o}C to 80^{o}C. While in [33], Sundaresan et al. presented the method of realizing active thermal compensation with electrostatic tuning via an adjustable voltage for a capacitive MEMS device, where the frequency drift is decreased from 2830ppm to 39ppm over the temperature range of 100^{o}C. Another main category of active compensation is the electronic frequency compensation with the aid of a phase-locked loop (PLL) and a highly accurate temperature sensor [34]–[36]. In [37], the frequency stability of a MEMS-based oscillator is increased by ~33 times with the utilization of the electronic frequency compensation method.

This dissertation will explore the methods of compensating for the performance changes caused by process variation through linear electrostatic feedback force tuning and addressing the thermal drift problem by nonlinear electrostatic feedback force tuning. Chapter 2 shows a comprehensive literature review that presents different methods for solving the process variation and thermal drift problems. Then, the backgrounds of the proposed methods, PODMEMS, will be introduced in **Chapter 3**, covering the mechanism of the MEMS resonator, feedback control theory, and stability analysis. With the background covered, **Chapter 4** and **Chapter 5** will then introduce the application of artificial stiffness and artificial nonlinear stiffness to a MEMS resonator separately. Then in **Chapter 6**, the MEMS resonator with artificial high quality and artificial nonlinear stiffness is developed. In **Chapter 7**, a test case of applying artificial stiffness,

damping, and nonlinear stiffness control to a MEMS gyroscope will be demonstrated. **Chapter 8** Concludes this investigation.

Chapter 2

Survey of Literature

This chapter reviews the literature on the methods for addressing process variation and thermal drift in microelectromechanical systems (MEMS) resonators. The chapter begins is divided into two parts: process variation compensation and thermal drift compensation, which begin by highlighting the challenges posed by process variation and temperature fluctuations. Then the review explores the existing methods of compensating for these challenges, including both passive and active compensation techniques. The chapter concludes by emphasizing the need for innovative techniques that provide greater dynamic control over the performance of MEMS devices.

2.1 Process Variation Compensation

The inherent variability that occurs during the fabrication process led to deviations in the physical dimensions, material properties, and overall performance of MEMS devices. These variations can arise from various sources, including lithography [38], etching [39], deposition [40], doping [41], and assembly processes. Process variation poses significant challenges to the consistent and reliable production of MEMS devices, as it can affect their functionality, performance, and yield.

2.1.1 Mechanical Tuning Methods

The mechanical tuning methods can be classified into additive and subtractive approaches. Additive methods add materials to the surface of the MEMS device to modify the resonator's structure. One commonly used additive method is selective deposition, which uses

Chemical Vapor Deposition (CVD) or Physical Vapor Deposition (PVD) to add material to the structure. CVD involves the reaction of precursor gases on the surface, resulting in the deposition of a desired material [42]. Selective CVD allows targeted deposition on specific regions of the device to modify its properties [43]. In [44], a metal layer is deposited onto the surface of a MEMS resonator, resulting in the resonance frequency being shifted by 11%. The advantages of using CVD methods include having a conformal coating, high-purity films, and precise control [45]. But the deposition time is usually longer than other methods [46], and therefore decreases the throughput of the production. While PVD methods, on the other hand, will have the benefit of requiring less deposition time [47]. Sputtering and evaporation techniques are usually used for PVD. Sputtering involves bombarding a target material with high-energy ions, causing atoms to be ejected and deposited on the substrate [48]. Evaporation involves heating a solid material, allowing the vaporized atoms to condense onto the substrate surface [49].

Another important method of additive mechanical tuning is electroplating. Electroplating is an electrochemical process that involves depositing a metal or alloy coating onto a conductive surface. It utilizes an electrolyte solution and an electrical current to facilitate the deposition of the desired material onto the MEMS structure.

Contrary to additive methods, subtractive methods use techniques such as chemical etching, laser ablation, ion milling, and mechanical milling to remove material from the MEMS device to tune the structure sizes. Chemical etching is a widely used technique in the fabrication of MEMS due to its benefits of low cost and high precision [50], which is achieved by selectively removing material from the substrate using chemical reactions. Commonly used etchant for MEMS are Potassium hydroxide (KOH) [51], Hydrofluoric acid (HF) [52], Hot phosphoric acid (H3PO4) [53], and so on. In [54], chemical etching reduces the frequency split

between the identical designed and fabricated cylindrical resonator gyroscope from 2.2Hz to less than 0.05Hz.

2.1.2 Electrical Tuning Methods

The review then discusses electrical tuning methods for compensating for process variation. Various electrical tuning methods have been developed, such as electrothermal, electrostatic, magnetic, piezoelectric, dielectric excitation, etc. Among those methods, electrostatic methods are of particular interest because of their benefits of virtually nonexistent current loss, high energy density, and large force at the micro-scale [55].

Electrostatic actuation methods involve applying an electrostatic force to the resonator to induce deflection and modify its effective stiffness. This can be achieved by varying the voltage applied to the electrodes, enabling tunability of the resonator's stiffness. The electrostatic actuation tuning methods can be further divided into four categories: parallel plate [56]–[60], varying gap [61]–[64], varying overlapping surface [65]–[68], and non-interdigitated [69]. The two most commonly used tuning techniques, parallel plate tuning, and varying gap tuning mechanisms, will be discussed as follows.

For parallel plate tuning, an electrostatic force generated by applying voltage difference across two capacitive plates will be applied to the MEMS devices, causing the parallel plate to move to generate a new equilibrium between the electrostatic attraction and mechanical restoring force. Therefore, around this new equilibrium, the effective stiffness will be defined by the sum of the mechanical and electrostatic forces. The electrostatic force can be adjusted by varying the applied voltage, where higher voltages result in increased electrostatic forces, leading to higher stiffness. In [70], the resonance frequencies of a MEMS gyroscope’s drive mode and sense mode, which should be matched for generating larger output amplitude, are mismatched

(~100Hz) due to process variation and temperature. However, by tuning the effective stiffness of the sense mode by applying DC voltage on the parallel plate, the mode mismatching is significantly reduced with a normalized sense mode stiffness change by a factor of 1.3.

2.2 Thermal Drift Compensation

Another challenging issue that MEMS devices are facing is thermal drift. Due to temperature variation, the physical sizes, material properties, ambient air pressure, packaging stress, and electronic circuits will all be subject to changes, causing the performance change of MEMS devices. In [71], the temperature drift of bias (TDB) of a comb MEMS accelerator caused by thermal expansion is 1.85mg/^{o}C, and the temperature drift of scale factor (TDSF) caused by thermal expansion and stiffness-temperature dependency is -162.7ppm/^{o}C. The MEMS gyroscope is another example of a device's performance significantly degraded by thermal drift. In [72], the zero bias stability of a disk MEMS gyroscope is only 27.8^{o}/h, which the TDB and TDSF cause. This chapter then focuses on compensation methods for addressing thermal drift in MEMS resonators. Two main categories of compensation techniques are discussed: passive compensation and active compensation.

2.2.1 Passive Compensation Methods

Passive compensation methods aim to reduce the influence of temperature fluctuations on MEMS devices. These methods involve selectively choosing materials with specific temperature coefficients [73]–[76], optimizing structural designs [77]–[82], and implementing packaging and thermal management techniques [28], [83]–[85].

Materials used in MEMS structure typically involve silicon, polysilicon, silicon dioxide (AlN), and so on. The material's properties are related to temperature through the temperature

coefficient. By selectively choosing and arranging the use of materials, the thermal drift of the device can be reduced. In [86], a SiO2 overlay with a temperature coefficient of frequency (TCF) >0 and a lithium niobate substrate with TCF<0 are chosen for the design of a surface acoustic wave (SAW) resonator, which resulted in the thermal drift smaller than 200kHz p.p., where the center frequency is 800MHz.

Except selectively choosing materials with specific temperature coefficients, optimize the structure of the MEMS device to reduce the thermal drift is another way to permanently compensate for temperature variation. In [79], He et al. studied the relation between TCSF and the wide-narrow gaps ratio (WNGR), which is defined as the ratio of the asymmetric comb fingers gap distance. Results reveal that with a certain range of WNGR, increasing the WNGR will have a smaller TCSF, therefore having a smaller thermal drift.

MEMS devices are usually packaged for protection from contamination and reduced damping. Thermal management of the packaging can also reduce the thermal drift of the device, which can be realized by thermal isolation and thermal dissipation. Using insulating materials, thermal isolation methods create a thermal barrier between the MEMS device and the external environment. This prevents heat transfer from external sources, reducing the temperature fluctuations experienced by the MEMS device. In [87], the MEMS sensor is encapsulated in a plastic carrier with low thermal conductivity of 0.96W/(m.K), which increases the measurement accuracy by two times. While thermal dissipation incorporates heat sinks, heat spreaders, or thermal vias to efficiently channel heat away from the MEMS device. In [88], the MEMS dies are placed inside a copper cavity on the substrate to provide better heat dissipation.

2.2.2 Active Compensation Methods

Active compensation methods actively sense and adjust the operating parameters of MEMS resonators to counteract the effects of thermal drift, which can be divided into categories as follows: oven control [89]–[92], electrostatic feedback control [93]–[97], and estimation model of temperature drift error development [98]–[101].

Oven control compensation method is the most straightforward technique, which utilizes the temperature sensor to sense the ambient temperature of the MEMS device. Then it uses the sensed temperature signal as the feedback signal for controlling the heater to maintain the ambient temperature at a constant value. The structure of the oven-controlled MEMS device can be divided into two categories: off-chip structure and on-chip structure. The off-chip solution is to install a mass-produced commercial MEMS sensor in a larger package. In [102], Yang et al. packaged the commercial six-axis MEMS inertial measurement unit (IMU) into a larger package, which has CMOS temperature sensor and heater to realize the temperature control. By doing so, the bias stability of the IMU is increased by 345 times. On the other hand, the on-chip structure integrates all structures in a sealed first-level package, which provides the benefit of reduced package size compared with the off-chip structure. In [103], the MEMS dies is attached to a platform, which is surrounded by a heating element made up of polysilicon. Results show that the active temperature control scheme successfully reduced the TCF by five times.

Oven control methods unavoidably increase the MEMS chip's size and the packaging's complexity. However, the electrostatic force feedback method uses temperature-dependent variables such as demodulated phase or resonant frequency as the control signal for the electrostatic feedback force-generating. In [97], Zhai et al. implemented the electrostatic force

feedback control on a MEMS differential capacitive accelerometer, which reduced the standard deviation of the scale factor of the accelerometer with respect to temperature by 95.69%.

Different from oven control and electrostatic force feedback control, which substantially change the mechanical performance of the MEMS device, the estimation model of temperature drift error method uses collected data of temperature change and output of the device to train the model for estimating the relationship between temperature change and zero bias error. Therefore, the output of the MEMS device can be compensated by the model. In [98], Zhu et al. employed the radical basis function neural network to develop the temperature drift error estimation model for thermal drift compensation, which decreased the acceleration random walking by 22 times.

2.3 Summary

This chapter focuses on the methods used to address process variation and thermal drift in MEMS resonators, which are divided into two main sections: process variation compensation and thermal drift compensation.

The challenges posed by process variation in MEMS devices are highlighted in the section on process variation compensation. The review explores various mechanical tuning methods, including additive and subtractive approaches. Additive methods, such as selective deposition and electroplating, involve adding materials to modify the resonator's structure, while subtractive processes, such as chemical etching and milling, remove material from the device. The section also discusses electrical tuning methods, with a particular focus on electrostatic actuation techniques that modify the resonator's stiffness by varying the applied voltage.

The section on thermal drift compensation addresses the issue of temperature-induced variations in MEMS devices. The impact of thermal drift on device performance is discussed, with examples from accelerometers and gyroscopes. Passive compensation methods are

explored, which involve selecting materials with specific temperature coefficients, optimizing structural designs, and implementing packaging and thermal management techniques. Active compensation methods, including oven control, electrostatic feedback control, and temperature drift error estimation models, are also discussed. These active methods actively sense and adjust operating parameters to counteract the effects of thermal drift.

In conclusion, the literature review emphasizes the need for innovative techniques that provide greater dynamic control over the performance of MEMS devices. The chapter provides a comprehensive overview of existing methods for process variation and thermal drift compensation, laying the foundation for further research and development in this field.

Chapter 3

PODMEMS Theory

This chapter introduces the basic theory of the performance of demand MEMS(PODMEMS). PODMEMS is a comprehensive and accurate method of electrically tuning MEMS devices' effective mass, damping, and stiffness based on continuous force feedback [104]. The PODMEMS method can compensate for the performance variations caused by process variation, packaging stress, temperature variation, and noise. Therefore, with the proposed method, MEMS devices can fully adjust their performance on demand.

3.1. Steady-State Analysis of Linear PODMEMS

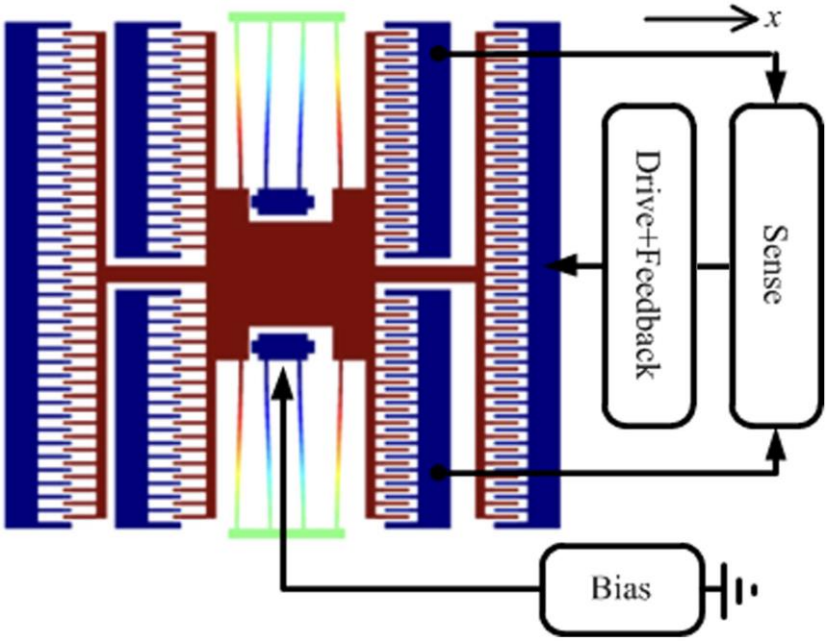

Figure 3.1: MEMS + performance controller. The structure incorporates symmetrical feedback components on both sides (left side unshown) that operate out of phase by 180°, ensuring continuous feedback response throughout each cycle. Left and right combs receive feedback forces proportional to position, velocity, and acceleration.

With the test case shown in **Figure 3.1**, the analytical expression of the effective mass, damping, and stiffness is obtained by using steady-state analysis subject to feedback latency. Assuming a sinusoidal driving force $F_{dr} = F_{dr,0}e^{jwt}$ is applied to the proof mass through the comb drives, where the $F_{dr,0}$ is the amplitude of the driving force, ω is the driving force's frequency. For the system shown in **Figure 3.1**, electrostatic feedback forces that are proportional to the displacement, velocity, and acceleration of the proof mass are applied. Therefore, the whole system can be described by eq (3.1).

$$\begin{aligned} M\ddot{x} + D\dot{x} + Kx &= F_{dr} - F_{fb}(x^{\tau_K}, \dot{x}^{\tau_D}, \ddot{x}^{\tau_M}) \\ &= F_{dr} - \left[F_K + F_D + F_M \right] \\ &= F_{dr} - \left[K_e x^{\tau_K} + D_e \dot{x}^{\tau_D} + M_e \ddot{x}^{\tau_M} \right] \end{aligned} \tag{3.1}$$

where $F_M = M_e \ddot{x}^{\tau_M}$, $F_D = D_e \dot{x}^{\tau_D}$, $F_K = K_e x^{\tau_K}$ are the feedback forces that are proportional to the sensed acceleration $\ddot{x}^{\tau_M} \equiv \ddot{x}(t - \tau_M)$, velocity $\dot{x}^{\tau_D} \equiv \dot{x}(t - \tau_D)$, and displacement $x^{\tau_K} \equiv x(t - \tau_K)$. Due to latency introduced by sensing and feeding back circuit, there will be latency τ_M, τ_D, and τ_K introduced. The quantities M_e, D_e, and K_e are the electrically-generated proportionality constants that constructively or destructively contribute to the system's effective mechanical stiffness, damping, or mass.

Assuming the steady-state solution to eq (3.1) has the form of $X(t) = x_0(\omega)e^{j(\omega t - \phi)}$, where x_0 is the amplitude of the motion displacement, ω is the angular frequency of the motion displacement, ϕ is the phase difference between the mechanical response angle and applied electrical driving angle. By substituting the solution to eq (3.1), the real and imaginary parts of the solution will be:

$$\frac{F_{dr,0}\cos(\phi)}{x_0} = -M\omega^2 + K - M_e\omega^2\cos(\omega\tau_M) + \omega D_e\sin(\omega\tau_D) + K_e\cos(\omega\tau_K) \tag{3.2}$$

$$\frac{F_{dr,0}\sin\phi}{x_0} = \omega D + M_e\omega^2\sin(\omega\tau_M) + \omega D_e\cos(\omega\tau_D) - K_e\sin(\omega\tau_K) \tag{3.3}$$

By squaring and summing eq (3.2) and eq (3.3), the displacement amplitude x_0 will be found as:

$$\begin{aligned} x_0(\omega) &= \frac{F_{dr,0}}{\sqrt{\begin{array}{c}(K + K_e\cos(\omega\tau_K) - (M + M_e\cos(\omega\tau_M) - D_e\omega^{-1}\sin(\omega\tau_D))\omega^2)^2 \\ +(D + D_e\cos(\omega\tau_D) - K_e\omega^{-1}\sin(\omega\tau_K) + M_e\omega\sin(\omega\tau_M))^2\omega^2\end{array}}} \\ &= \frac{F_{dr,0}}{\sqrt{(K_{eff} - M_{eff}\omega^2)^2 + D_{eff}^2\omega^2}} \end{aligned} \tag{3.4}$$

where the second relation in eq (3.4) is determined by an effective equation of motion in standard form:

$$M_{eff}\ddot{x} + D_{eff}\dot{x} + K_{eff}x = F_{dr} \tag{3.5}$$

Therefore, the effective stiffness K_{eff}, effective damping D_{eff}, and effective mass M_{eff} can be found through (3.4) as :

$$\begin{aligned} K_{eff} &= K + K_e\cos(\omega\tau_K) \\ &\approx K + K_e \end{aligned} \tag{3.6}$$

$$\begin{aligned} D_{eff} &= D + D_e\cos(\omega\tau_D) - K_e\omega^{-1}\sin(\omega\tau_K) + M_e\omega\sin(\omega\tau_M) \\ &\approx \mathrm{D}+\mathrm{D}_e - K_e\tau_K + M_e\omega^2\tau_M \end{aligned} \tag{3.7}$$

$$\begin{aligned} M_{eff} &= M + M_e\cos(\omega\tau_M) - D_e\omega^{-1}\sin(\omega\tau_D) \\ &\approx M + M_e - D_e\tau_D \end{aligned} \tag{3.8}$$

The first relations in eq (3.6)-(3.8) show the exact representation of the effective stiffness, damping and mass, while the second relations show the first-order approximation, assuming that the feedback latency is much smaller than the time period of proof-mass oscillation $\tau \ll 2\pi/\omega$.

The phase difference between the response angle $\omega t - \phi$ and the drive angle ωt is found by the ratio of eq (3.3) to (3.2) as:

$$\phi = \tan^{-1}\left(\frac{\omega D_{eff}}{K_{eff} - \omega^2 M_{eff}}\right) \tag{3.9}$$

The performance parameters of the PODMEMS can be calculated from eq (3.5) as follows.

Exponential decay rate:

$$\gamma_{eff} = \frac{1}{2} D_{eff} \Big/ M_{eff} \tag{3.10}$$

Quality factor:

$$Q_{eff} = \frac{\omega_{d,eff}}{2\gamma_{eff}} = \frac{\omega_{d,eff} M_{eff}}{D_{eff}} = \frac{1}{2}\sqrt{\frac{\omega_{0,eff}^2 + \omega_{r,eff}^2}{\omega_{0,eff}^2 - \omega_{r,eff}^2}} \tag{3.11}$$

Amplitude at displacement resonance:

$$x_{\max} = \frac{F_{dr,0}}{D_{eff}\omega_{d,eff}} \tag{3.12}$$

Velocity resonance:

$$\omega_{0,eff} = \sqrt{\frac{K_{eff}}{M_{eff}}} \tag{3.13}$$

Frequency relations:

$$\omega_{r,eff}^2 = \omega_{0,eff}^2 - 2\gamma_{eff}^2 = \omega_{d,eff}^2 - \gamma_{eff}^2 = 2\omega_{d,eff}^2 - \omega_{0,eff}^2 \tag{3.14}$$

3.2. Steady-State Analysis of Nonlinear PODMEMS

In this section, the PODMEMS is extended from linear to nonlinear by considering third-order nonlinearity, which is generated by feeding back a force proportional to the cubic of proof mass displacement. The governing equation can describe such a system.

$$\begin{aligned} M\ddot{x} + D\dot{x} + Kx + \kappa x^3 &= F_{dr} - F_{fb}((x^3)^{\tau_\kappa}) \\ &= F_{dr} - F_{\kappa} \\ &= F_{dr} - \kappa_e (x^3)^{\tau_\kappa} \end{aligned} \tag{3.15}$$

where $F_{\kappa} = \kappa_e (x^3)^{\tau_\kappa}$ is the feedback force proportional to the cubic of sensed displacement $(x^3)^{\tau_\kappa} \equiv x^3(t - \tau_\kappa)$. The latency introduced by the sensing and feedback circuit is represented by τ_κ. The original nonlinearity coefficient of the MEMS device is represented by κ, which is usually a very small value. On the other hand, the quantity κ_e is the electrically generated proportionality constant that constructively or destructively contributes to the effective mechanical nonlinear stiffness of the system.

The steady-state solution to eq (3.15) can be found with Harmonic Balance Method(HBM). Firstly, when the driving force equals to $F_{dr,0}\cos(\omega t)$, eq (3.15) can be rewritten as:

$$\ddot{x} + \delta\dot{x} + \alpha x + \beta x^3 = A\cos(t) \tag{3.16}$$

where $\delta = D/M$, $\alpha = K/M$, $\beta = \kappa_e/M$, $A = F_{dr,0}/M$.

The approximate solution to the equation will take the form of:

$$x = a\cos(\omega t) + b\sin(\omega t) = Z\cos(\omega t - \phi) \tag{3.17}$$

where $Z=\sqrt{a^2+b^2}$ is the amplitude of displacement of proof mass, $\phi=\tan^{-1}(b/a)$ is phase difference between the mechanical response angle and applied electrical driving angle.

Substitute the approximate solution into eq (3.16) will have:

$$\begin{aligned}&(-\omega^2 a+\omega\delta b+\alpha a+\frac{3}{4}\beta a^3-A)\cos(\omega t)+(-\omega^2-\omega\delta a+\alpha b+\frac{3}{4}\beta b^3+\frac{3}{4}\beta b a^2)\sin(\omega t)\\&+(\frac{1}{4}\beta a^3-\frac{3}{4}\beta a b^2)\cos(3\omega t)+(-\frac{1}{4}\beta^3+\frac{3}{4}\beta b a^2)\sin(3\omega t)=0\end{aligned} \tag{3.18}$$

Neglecting the super harmonics term at $3\omega t$, the remaining two terms $\cos(\omega t)$ and $\sin(\omega t)$ must be zero, which leads to the following two equations:

$$\begin{cases}-\omega^2 a+\omega\delta b+\alpha a+\frac{3}{4}\beta a^3+\frac{3}{4}\beta a b^2-A=0\\ -\omega^2 b+\omega\delta a+\alpha b+\frac{3}{4}\beta b^3+\frac{3}{4}\beta b a^2=0\end{cases} \tag{3.19}$$

The amplitude-frequency response can be obtained by squaring both terms of eq (3.19) and adding them together:

$$\left[\left(\omega^2-\alpha-\frac{3}{4}\beta Z^2\right)^2+(\delta\omega)^2\right]Z^2=A^2 \tag{3.20}$$

For the system described with eq (3.16), when the nonlinear stiffness $\beta>0$, the system's stiffness characteristic is hardening. Otherwise, when $\beta<0$, the system's stiffness characteristic is softening. As shown in Fig.1, by using eq (3.20), the frequency responses of eq (3.16) with different β values are plotted.

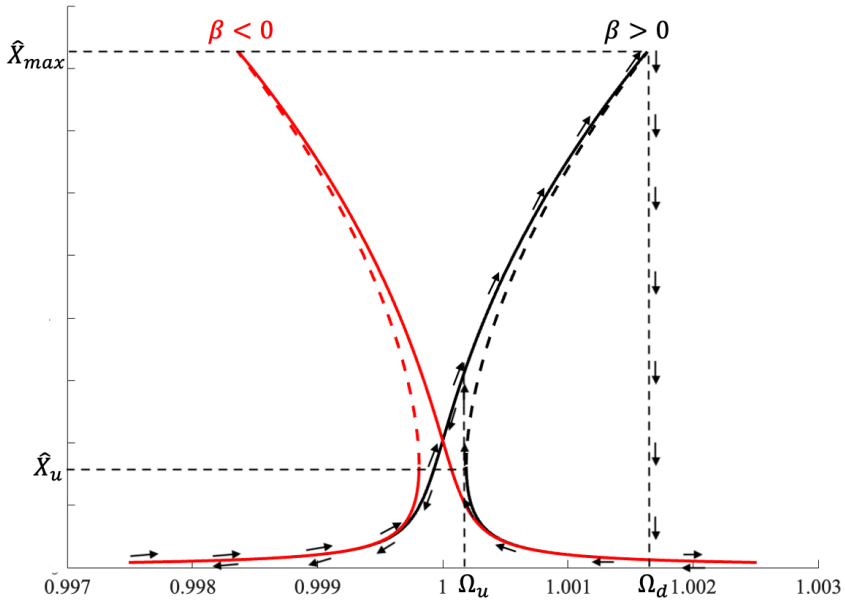

Figure 3.2: Frequency response of the nonlinear system. As shown in the figure, the black curve shows when the nonlinear stiffness β is a positive value, which is hardening. On the contrary, the red curve shows when the nonlinear stiffness β is negative, corresponding to the softening characteristic. For both the hardening and softening frequency responses, the solid lines represent the stable state, while the dashed lines represent the unstable state of the system. Taking the hardening system as an example, when the driving frequency is swept from the low frequency to high frequency, the displacement amplitude will follow the solid line until point D. After that, there will be the jump phenomenon, which causes the displacement amplitude to drop dramatically. On the other hand, if the frequency is swept from high frequency to low frequency, the displacement amplitude will follow the solid line until point U, where the jump-up phenomenon will occur, causing the amplitude to increase dramatically. This phenomenon also apply to the softening system.

The jump phenomenon for both the hardening and softening situations. The jump phenomenon is caused by the unstable status of the system, which is described in more detail in [105]. With a determined β value, the jump-up and jump-down frequency will be dependent on the direction of the sweeping excitation frequency. For a hardening system, the jump-down will occur when increasing the sweeping frequency from below the unstable region to into the

unstable region. On the other hand, the jump-up will occur when decreasing the sweeping frequency from a stable region into an unstable region. The jump-down frequencies are expressed in the following equation:

$$\Omega_d = \sqrt{\frac{3}{4}\alpha \hat{X}_{\max}^2 + (1-2\zeta^2)} \tag{3.21}$$

where $\zeta = D/2M\omega$, $\hat{X}_{\max}$ is the maximum amplitude, expressed as:

$$\hat{X}_{\max} \approx \frac{F_{dr,0}}{K}\sqrt{\frac{2}{3\alpha}\left(\sqrt{1+\frac{3\alpha}{4\zeta^2}}-1\right)} \tag{3.22}$$

Meanwhile, the jump-up frequency, which is dependent on whether the system is softening or hardening, can be expressed as follows:

Hardening system:

$$\Omega_u = 1+\frac{3}{4X_{up}} \tag{3.23}$$

Softening system:

$$\Omega_u = 1-\frac{3}{4X_{up}} \tag{3.24}$$

where X_{up} is the amplitude at jump-up frequency, which is expressed as:

$$X_{up} = \left(\frac{2}{3}\right)^{1/3}\frac{1}{|\alpha|^{1/3}} \tag{3.25}$$

3.3. Stability Analysis

The stability characteristic of eq (3.1) can be revealed by finding the region where the equation is stable in (M_e, D_e, K_e)-sapce, through using *eigenvalue analysis of the characteristic*

equation. To make the presentation simpler, assuming that $\tau_M = \tau_D = \tau_K = \tau$, therefore, the characteristic equation for eq (3.1) is expressed as:

$$Mz^2 + Dz + K + e^{-\tau z}\left(M_e z^2 + D_e z + K_e\right) = 0 \tag{3.26}$$

The borderline values between stability and instability of eq (3.1) is given by the values of M_e, D_e, and K_e, which give pure imaginary solutions $z = jy$ of eq (3.26). Thus, substituting $z = jy$ into the homogeneous equation (3.26) and solving for D_e and K_e, we have

$$\begin{cases} D_e(y) = \left(My^2 - K\right)\sin\left((\tau y)/y\right) - D\cos(\tau y) \\ K_e(y) = \left(My^2 - K\right)\cos(\tau y) - Dy\sin(\tau y) + M_e y^2 \end{cases} \tag{3.27}$$

Here, the parameter $y \geq 0$ introduces a spiral in the (D_e, K_e)-plane through equations (3.27). Additionally, when considering the fixed M_e value, this spiral, along with the line $K_e = -K$ where $z = 0$ solves eq (3.26), defines a partition within the (D_e, K_e)-plane. By allowing M_e to vary, we obtain a corresponding partition in (M_e, D_e, K_e)-space. The next step involves selecting the subset from this partition that includes $(M_e, D_e, K_e) = (0,0,0)$. For any triple (M_e, D_e, K_e) chosen from this selected subset, eq (3.1) demonstrates stability. This stability analysis yields zero error as it relies on finding exact solutions of the characteristic equation.

Figure 3.3a and **3.3c** depict families of stability domains, showcasing different M_e and τ values. These domains are plotted as a function of D_e/D versus K_e/K. In **Figure 3.3b** and **3.3d**, the magnified views of these domains specifically around the system state $(D_e/D, K_e/K) = (0,0)$ is presented. The stability domains represent regions within the domes, which are delimited by solid curves and the horizontal dashed line at $K_e/K = -1$. It is

important to note that system states located outside the domes, characterized by $D_e/D, K_e/K, M_e$, and τ, indicate instability.

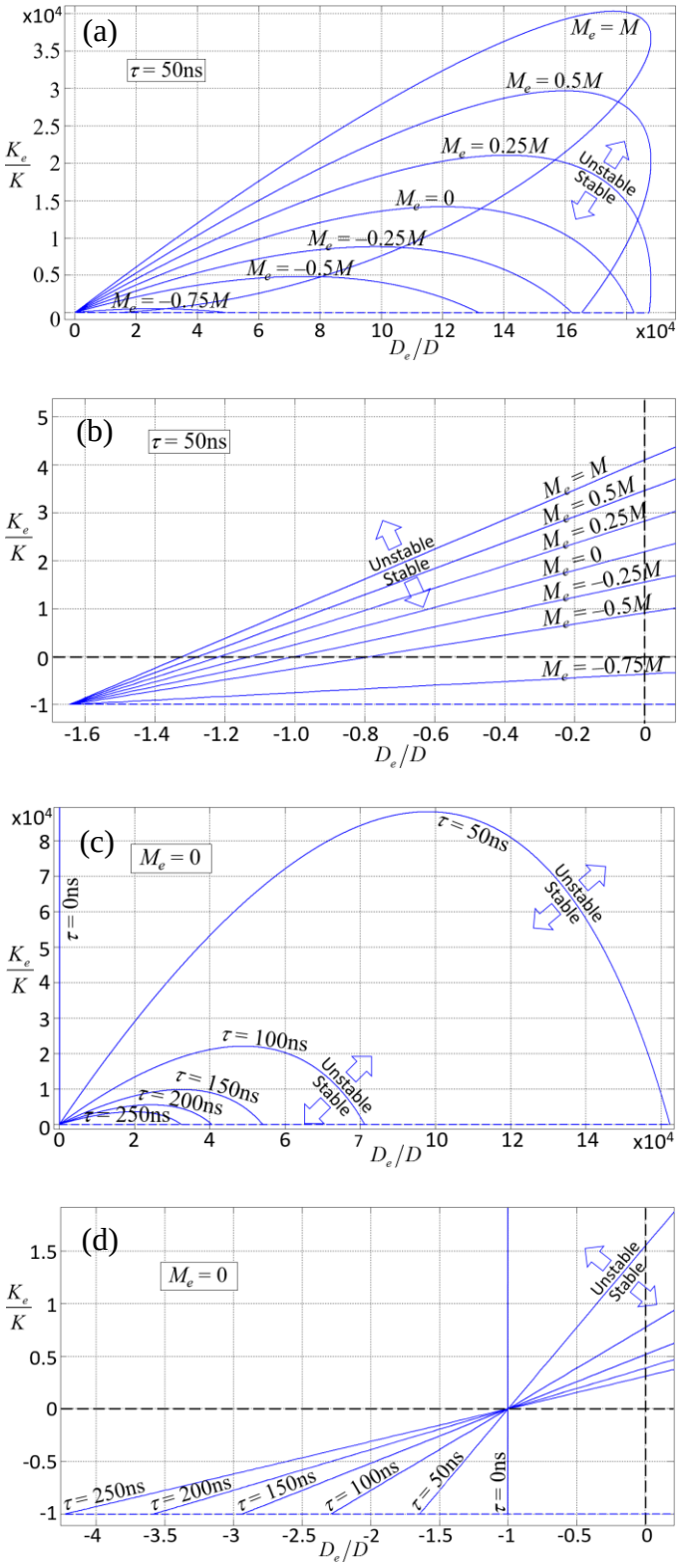

Figure 3.3: The stability domains of PODMEMS are illustrated for various M_e values. The horizontal-axis represents the ratio of electrical to mechanical damping, while the vertical-axis represents the ratio of electrical to mechanical stiffness. The dome-shaped areas enclosed between the curve and the horizontal line $K_e/K = -1$ indicate regions of stability. Within each dome, stability diminishes as the state approaches its boundary, reaching zero precisely on the boundary. Conversely, outside the domes, instability intensifies as the state moves farther away from the stability boundary. **Figure 3.3a** portrays the stability domains for different Me values, while **Figure 3.3b** provides a closer view around the point $(D_e/D, K_e/K) = (0,0)$. Additionally, **Figure 3.3c** exhibits stability domains for various τ values, with **Figure 3.3d** offering a magnified perspective near (0,0). It is worth noting that upon further magnification of **Figure 3.3d**, it becomes evident that all curves do not intersect at a single point near (-1, -2.9x10-3).

3.4. Conclusion

This chapter demonstrates the basic theory of PODMEMS, including both linear and nonlinear steady-state analysis. The effective stiffness, damping coefficient, and mass can be tuned by feeding back forces that are proportional to the sensed displacement, velocity, and acceleration. Meanwhile, the influence of latency introduced by sensing and feedback circuit are considered for the linear PODMEMS analysis. On the other hand, by feeding back a force that is proportional to the cubic of proof mass displacement, the third-order nonlinearity can be easily tuned, therefore realizing nonlinear PODMEMS.

Chapter 4

Artificial Linear Stiffness

This chapter introduced an on-time method of linearly tunning the effective stiffness of MEMS resonators. The proposed tunning mechanism is achieved by applying a feedback signal to the resonator to generate a feedback force proportional to the displacement. The feedback signal is obtained by adjusting the resonator's sensed displacement amplitude. Such a technique can be used for various applications, such as compensating the parameter variations introduced by process or temperature variation and achieving large displacement with extreme-low effective stiffness. Previous efforts by others on tuning the stiffness include post-processing with mechanical methods and electrical tunning by position based-feedback. However, we proposed a method of on-time tunning of stiffness with more dynamic controllability. The proposed analytical model has been verified by simulation in MATLAB/Simulink. The simulation result shows that by applying a feedback voltage with a voltage amplitude of only 1.1V, the effective stiffness can be decreased by 0.08N/m, resulting in a resonance frequency shift of 6Hz.

4.1 Analytical Model

4.1.1 MEMS resonator

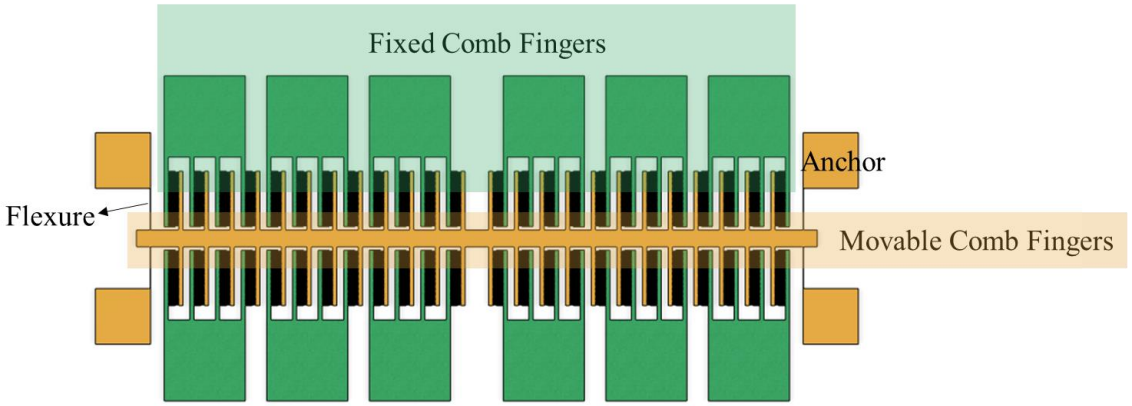

Figure 4.1: Layout of the MEMS resonator. The resonator is driven by electrostatic force, which is generated by the voltage difference between the fixed comb-fingers and movable comb-fingers. Except for the purpose of generating the electrostatic force, the fixed comb-finger capacitors are also used to sense the movement of the movable comb-fingers. The four flexures supported the movable comb-fingers and provided stiffness for the system.

The schematic of the comb-drive MEMS resonator used for the study is shown in **Figure 4.1**. Such a system can be modeled as a second-order mass-spring-damper system:

$$M\ddot{x}(t) + D\dot{x}(t) + Kx(t) = F_{dr}(t) \tag{4.1}$$

where M is the mass of the proof mass, D is the damping coefficient, K is the stiffness, $x(t)$ is the displacement of the proof mass, and $F_{dr}(t)$ is the electrostatic force generated by comb-finger capacitors.

The transfer function of the second-order system is expressed as follows:

$$G(s)=\frac{X(s)}{F_{dr}(s)}=\frac{1/M}{s^2+\frac{\omega_n}{Q}s+\omega_n^2} \tag{4.2}$$

Where Q is the quality factor of the system, ω_n is the undamped natural frequency.

The parameters used in our test case are: flexure width $w = 3\mu m$, thickness $h = 25\mu m$, and length $L = 300\mu m$; the two pairs of $N = 200$ finger comb drive arrays have initial finger overlap length $l_0 = 20\mu m$, finger width $w_f = 2\mu m$, and gap $g = 2\mu m$; Young's modulus $E = 160GPa$, density $\rho = 2300kg/m^3$, structure-to-substrate gap $g_{sub} = 2\mu m$, viscosity $\mu = 1.75\times10^{-5}$ sPa, and proof mass area $a_{pf} = 1.19\times10^{-6}\ m^2$ (including flexures and combs). This yields a compact mass of $M = \rho \times volume = 6.87\times10^{-8}$ kg, and stiffness of $K=\frac{4Ehw^3}{L^3}=16\,N/m$. The damping at standard atmospheric pressure is $D=\mu a_m/g_{sub}=1.04\times10^{-5}\,Ns/m$, with a quality factor of $Q \approx \omega_0 M/D = 101$ in air. Static capacitance is $C_0=\frac{\varepsilon_0 h l_0 N}{g}=0.44pF$, where the permittivity of the medium is $\varepsilon_0 = 8.854\times10^{-12}$ F/m. The driving force is $F_{dr}=\frac{1}{2}\frac{C_0}{l_0}V_{dr}^2$. All the parameters used in this article are listed in **Table 4.1**.

Table 4.1: Nomenclature of Artificial Linear Stiffness System

Parameter	Value	Unit	Description
a_m	1	atm	Standard atmospheric pressure
a_{pf}	1.19×10^{-6}	m^2	Area of proof mass

C_0	1.1×10^{-12}	F	Static capacitance
D	1.04×10^{-5}	Ns/m	Damping coefficient
ε_0	8.854×10^{-12}	F/m	Permittivity of the medium
E	1.6×10^{11}	Pa	Young's modulus
g	2×10^{-6}	m	Gap between comb fingers
g_{sub}	2×10^{-6}	m	Structure-to-substrate gap
G_f	5	1	Gain of amplifier
h	2.5×10^{-5}	m	Thickness of structure layer
K	16.039	N/m	Stiffness
L	3×10^{-4}	m	Length of flexure
l_0	2.5×10^{-5}	m	Initial comb-finger overlap length
M	6.87×10^{-8}	Kg	Mass
N	200	1	Comb finger numbers
Q	101	1	Quality factor
μ	1.75×10^{-5}	sPa	Viscosity of air
w	3×10^{-6}	m	Flexure length
w_f	2×10^{-6}	m	Finger width

To analyze the dynamic performance of the MEMS resonator, COMSOL is used for the simulation. Firstly, the eigenfrequency study is conducted, which reveals the first resonate mode frequency along the x-direction at 2475.9Hz and the second mode resonate frequency along the

y-direction at 12733Hz. Since the first and second modes' resonate frequencies are assigned far away, the unwanted motion along the y-direction can be avoided. Secondly, the stationary study is conducted by applying a constant voltage of 20V across one pair of fixed and movable comb-finger capacitors, which generated an electrostatic force of 8.8uN. With the simulated stationary displacement of 0.55um, the stiffness of the system can be calculated as $K = F_{stat} / x_{stat} = 16\,\mathrm{N/m}$. The COMSOL simulation shows a good alignment with the calculated parameter values.

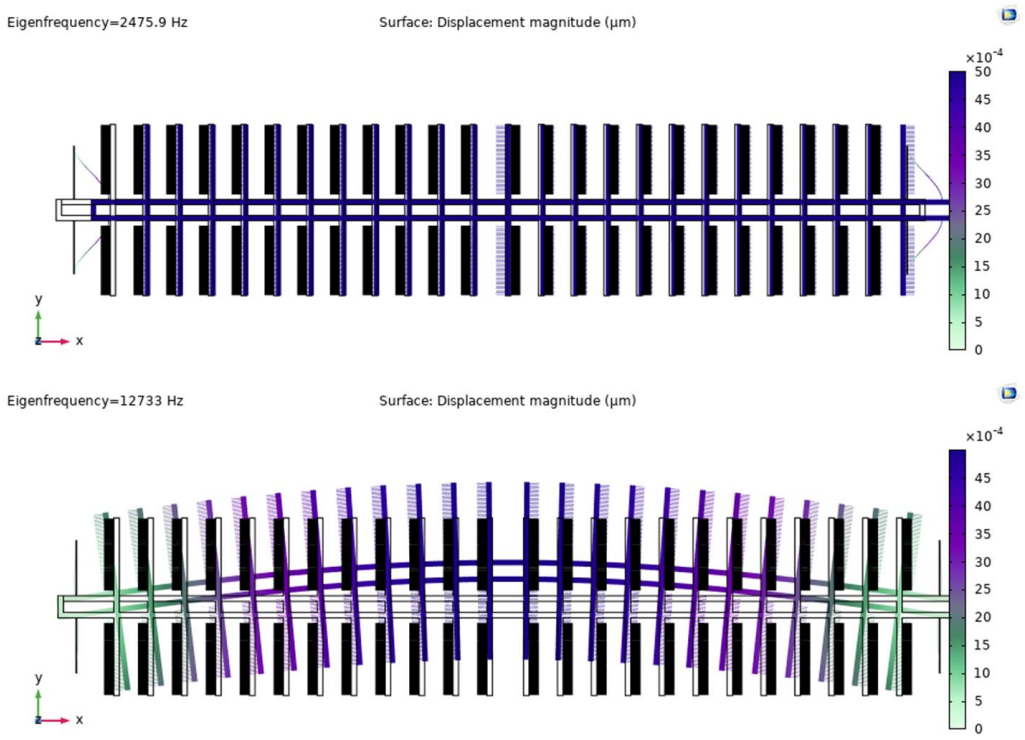

Figure 4.2: (a)First resonant mode of the MEMS resonator at 2475Hz. The direction of movement of the first resonant mode is along the x-direction. (b) The second resonant mode of the MEMS resonator is at 12733Hz. The direction of movement of the first resonant mode is along the y-direction.

4.1.2 Artificial Stiffness Tunning Principle

With the MEMS resonator designed as in **Figure 4.1**, the artificial stiffness tunning will be realized by adding the force feedback as in **Figure 3.1** expressed by eq (4.3):

$$M\ddot{x} + D\dot{x} + \left(K - K_e\right)x = F_{dr} \tag{4.3}$$

where K_e is the proportionality constants of the electrically generated feedback forces: $F_K = K_e x\left(t-\tau\right)$, and τ is the feedback latency.

Eq (4.3) is a form that ignores feedback latency τ for simplicity. By explicitly including latency, eq (4.3) is expressed as

$$M\ddot{x}\left(t\right) + D\dot{x}\left(t\right) + Kx\left(t\right) - K_e x\left(t-\tau\right) = F_{dr} \tag{4.4}$$

where $x\left(t\right)$ is the position at the time t, and $x\left(t-\tau\right)$ was the position about several nanoseconds ago.

Applying Laplace transform to eq (4.4), the transfer function of the stiffness tunable system is:

$$G\left(s\right) = \frac{1}{Ms^2 + Ds + K - K_e e^{-\tau s}} \tag{4.5}$$

When the latency τ is relatively small, the term $e^{-\tau s}$ can be approximated by Taylor 1st order expansion:

$$e^{-\tau s} = 1 - \tau s \tag{4.6}$$

Therefore, the transfer function eq (4.5) can be rewritten as:

$$G\left(s\right) = \frac{1}{Ms^2 + \left(D + K_e\tau\right)s + K - K_e} = \frac{1/M}{s^2 + \frac{\omega_{eff}}{Q_{eff}}s + \omega_{eff}^2} \tag{4.7}$$

where the $\omega_{eff} = \sqrt{\frac{K - K_e}{M}}$ is the effective undamped natural frequency, $Q_{eff} = \frac{\omega_{eff} M}{D + K_e\tau}$ is the effective quality factor. The transfer function eq (4.7) suggest that the small latency will result in a decrease in the quality factor.

However, when the latency is relatively large, the term $e^{-\tau s}$ needs to be approximated by Taylor 2nd order expansion:

$$e^{-\tau s} = 1 - \tau s + \frac{\tau^2}{4} s^2 \tag{4.8}$$

This will result in the transfer function of:

$$G(s) = \frac{1}{\left(M - \frac{K_e \tau^2}{4}\right) s^2 + \left(D + K_e \tau\right) s + K - K_e} = \frac{1 \Big/ \left(M - \frac{K_e \tau^2}{4}\right)}{s^2 + \frac{\omega_{eff}}{Q_{eff}} s + \omega_{eff}^2} \tag{4.9}$$

where the $\omega_{eff} = \sqrt{\frac{K - K_e}{M - \frac{K_e \tau^2}{4}}}$ is the effective undamped natural frequency, $Q_{eff} = \frac{\omega_{eff}\left(M - \frac{K_e \tau^2}{4}\right)}{D + K_e \tau}$ is the effective quality factor. From eq (4.9), it can be seen that the latency will introduce another influence on the effective mass of the system, which will cause the shift of the resonance frequency and decrease the quality factor.

The proposed artificial stiffness tunning technique is realized in the system shown in **Figure 4.3**

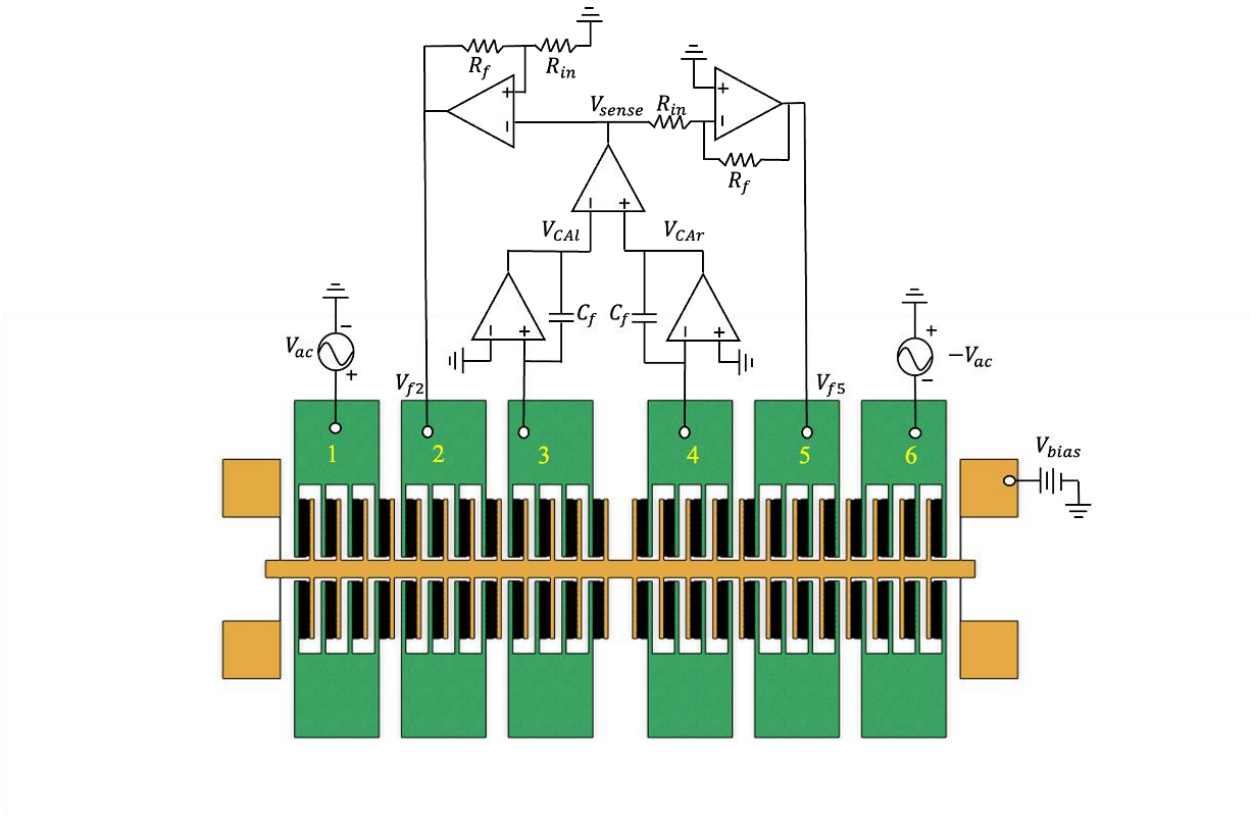

Figure 4.3: Block diagram of the stiffness tunable MEMS resonator. There are six pads connected to the fixed-comb-fingers arrays, chosen for the purpose of driving, sensing and feedback. Besides, the movable comb-fingers are all biased with a DC voltage. For the driving purpose, the differential AC voltages V_{ac} and $-V_{ac}$ are applied to pad 1 and 6, which will generate a total force linearly proportional to the amplitude of the AC voltage. For the sensing purpose, the two identical charge amplifiers are connected to pads 3 and 4, forming a differential charge sensing structure. The sensed voltage V_{sense} is linearly proportional to the displacement of the proof mass, which will then be split into a pair of differential signals applied to pad 2 and 5 for the purpose of generating feedback force.

To drive the MEMS resonator to vibrate and achieve the linear voltage-force relationship, a differential AC+DC driving voltage will be applied to pad 1 and 6:

Pad1:

$$V_{dr1} = V_{ac} - V_{bias} = A\sin(\omega t) - V_{bias} \tag{4.10}$$

Pad6:

$$V_{dr6} = -V_{ac} - V_{bias} = -A\sin(\omega t) - V_{bias} \tag{4.11}$$

where the Vac is the AC voltage, whose amplitude is A and frequency is ω, V_{bias} is the DC voltage applied to moveable comb fingers.

Since pad 1 and pad 6 has comb fingers pointed in the opposite direction, the total driving force will be the subtraction of the electrostatic force generated by pad 1 and pad6:

$$F_{dr} = \frac{1}{2}\frac{C_0}{l_0}V_l^2 - \frac{1}{2}\frac{C_0}{l_0}V_r^2 = 2\frac{C_0}{l_0}AV_{bias}\cos\left(\omega_n t\right)[\mathrm{N}] \tag{4.12}$$

When the frequency of the exciting voltage is equal to the effective resonate frequency ω_{eff}, the steady state amplitude of displacement is:

$$\left|x(t)\right| = \frac{\left|F_{dr}\right|Q}{\omega_{eff}^2 M} \tag{4.13}$$

When the driving force drives the resonator F_{dr}, the changing of fixed-movable comb-finger capacitor overlap areas will cause the accumulated charge changing on pad 3 and pad 4, which will be described as:

Pad3:

$$q_3 = \frac{\varepsilon_0\varepsilon_r h\left(l_0 + x(t)\right)N}{g}V_{bias} \tag{4.14}$$

Pad4:

$$q_4 = \frac{\varepsilon_0\varepsilon_r h\left(l_0 - x(t)\right)N}{g}V_{bias} \tag{4.15}$$

The charge will then be picked up and amplified by the charge amplifier. A differential charge amplifier structure is adopted to reduce parasitic capacitance effect. The sensing equation is expressed as follows:

$$V_{sense} = V_{CAl} - V_{CAr} = \frac{q_l}{C_f} - \frac{q_r}{C_f} = \frac{2\varepsilon_0 \varepsilon_r h x(t)}{g} * \frac{V_{bias}}{C_f} \tag{4.16}$$

Eq (4.16) suggested that the sensed voltage V_{sense} is directly proportional to the displacement $x(t)$. The sensed voltage will then be split into two differential signals, amplified with the same gain G_f. The feedback voltages applied to pad 2 and pad 5 are expressed as:

$$\begin{cases} V_{f2} = G_f V_{sense} - V_{bias} \\ V_{f5} = -G_f V_{sense} - V_{bias} \end{cases} \tag{4.17}$$

The electrostatic feedback force generated by the feedback voltage is then described as:

$$F_{fb} = \frac{1}{2}\frac{C_0}{l_0} V_{fl}^2 - \frac{1}{2}\frac{C_0}{l_0} V_{fr}^2 = 2\frac{C_0}{l_0} G_f V_{bias} V_{sense} = 4\frac{C_0^2}{l_0^2}\frac{G_f V_{bias}^2}{C_f} x(t) \tag{4.18}$$

Substituting eq (4.18) into eq (4.4), the governing equation of the stiffness tunable system is:

$$M\ddot{x}(t) + D\dot{x}(t) + Kx(t) = F_{dr} + F_{fb} = 2\frac{C_0}{l_0} A V_{bias} \cos(\omega_n t) + 4\frac{C_0^2}{l_0^2}\frac{G_f V_{bias}^2}{C_f} x(t) \tag{4.19}$$

Therefore, the electrically generated stiffness is $K_e = 4\frac{C_0^2}{l_0^2}\frac{G_f V_{bias}^2}{C_f}$.

4.2 Simulation

To verify the proposed system, the simulation is performed in Matlab/Simulink(R2022a). As shown in Fig.4, the MEMS resonator is represented by a second-order system that integrates the acceleration signal. The Driving Voltage-Force and Feedback Voltage-Force blocks represent

the voltage-to-force functions of the resonator ports. On the other side, the Differential Charge Amplifier block represents the displacement-to-charge relationship and the following charge amplifier stage.

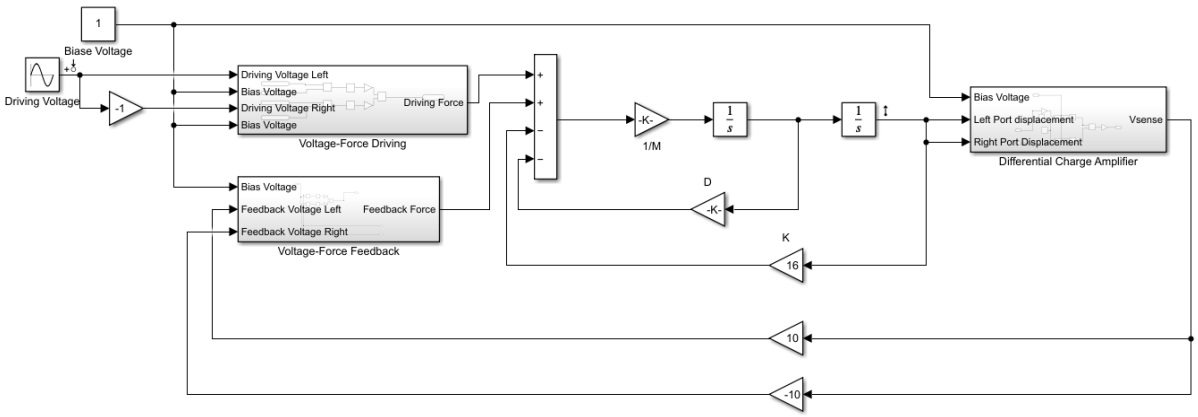

Figure 4.1: Simulation setup in MATLAB/Simulink. The mechanical spring-mass-damper system of the MEMS resonator is represented by the second-order system with two integrators. The voltage-force driving and voltage-force feedback blocks represent the voltage-to-force relationship at the ports. The differential charge amplifier represents the displacement to voltage conversion. Lastly, the amplifier block amplifies the sensed voltage signal and is processed to generate differential feedback voltages.

Figure 4.5 shows the simulation result of frequency response when electronic stiffness K_e =0 N/m and -0.31N/m. The system was applied with a total of 10V DC voltage at a simulation time of 0.05s.

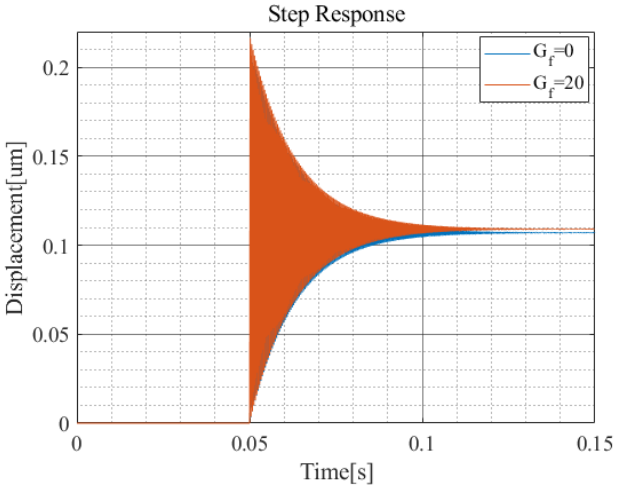

Figure 4.5: Step response of the system when with and without the electrical stiffness tuning.

Figure 4.6 shows the resonance frequency change simulation result when electronic stiffness K_e=0.08N/m, 0N/m, and -0.08N/m. The value of electronic stiffness value is setup by setting the amplifier gain G_f value equal to -5, 0, and 5. Meanwhile, in this simulation, the feedback circuit latency τ is not included. Simulation results show that the resonator's resonance frequency is tuned by 6Hz, 0Hz, and -6Hz.

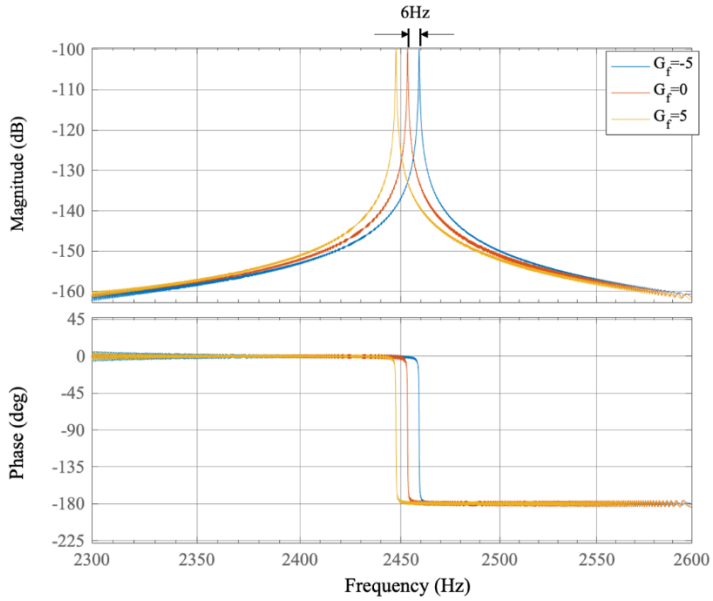

Figure 4.6: Frequency response of the system with different electrical stiffness K_e value.

To show the influence of the feedback circuit latency on the quality factor of the system, a transport delay block is added with latency values of 0us, 1us, and 10us. As discussed in eq (4.7), when the latency is small, the latency term can be described by using Taylor 1st order expansion, which will cause influence on the damping coefficient of the system. As shown in **Figure 4.7**, the *Q* is reduced by a, and b for latency of 1us and 10us.

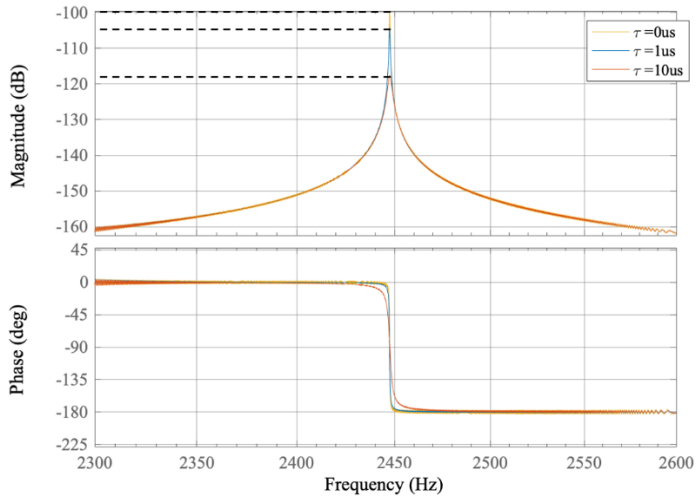

Figure 4.7: Frequency response of the system with same electrical stiffness K_e value, but different feedback circuit latency. The latency values are set to be smaller than 10us, which can be treated as relatively small latency.

However, as shown in eq (4.9), when the latency is large enough, the latency term needs to be described by Taylor's 2nd-order expansion, which will cause influence on both the damping coefficient and effective mass. As shown in **Figure 4.8**, when the latency tau is increased from 0us to 500us, the quality factor is decreased by a. Meanwhile, the resonance frequency is also shifted from c to d, due to a change of effective mass.

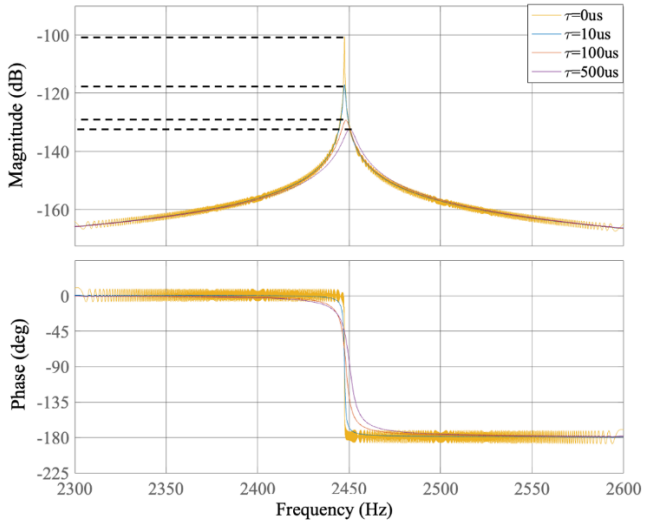

Figure 4.8: Frequency response of the system with the same electrical stiffness K_e value, but different feedback circuit latency. The latency values are set to be larger than 10us, which can be treated as relatively large latency.

4.3 Conclusion

In this chapter we proposed a method to solve the problem of resonance frequency shift caused by process variation. Due to process variation, even identically designed MEMS devices will perform differently, such as the geometry variation causing the stiffness variation of the

flexures. Therefore, causing the resonance frequency shift. However, though consistently feeding back a force proportional to the displacement of the proof mass, the effective stiffness of the device will be tuned.

Chapter 5

Artificial Nonlinear Stiffness

Nonlinearity in MEMS resonators is usually unwanted because it degrades performance based on linearized sensing. However, this chapter examines the generation and utilization of artificial nonlinear stiffness for a micro-electromechanical system (MEMS) resonator to reduce the influence of the thermal drift problem. Utilizing the resonator's nonlinear behavior, the amplitude of motion can remain large while the structural resonance frequency drifts, and the drive frequency remains constant. Our previous efforts showed the methods of tuning the apparent mass, damping, and stiffness linearly by applying electrostatic feedback force. Here, we implement this method with nonlinear stiffness, which is generated by applying an electrostatic feedback force proportional to the cubed displacement of the proof mass. As a test case, we demonstrate how this concept may benefit devices that suffer from thermal drift, such as MEMS vibratory gyros. The test case is simulated with Simulink, which is verified by comparing it with analytical results. The results suggest when the temperature is decreased by 10K from the room temperature that artificial nonlinear stiffness can help reduce the amplitude attenuation of oscillation to 3dB while resonance frequency drifts 10Hz about a constant drive frequency of 2449Hz, where the amplitude attenuation is 36dB for the system without nonlinear feedback.

5.1 The design of the artificial nonlinear stiffness resonator system

The nonlinear stiffness model is realized in the system shown in **Figure 5.1**.

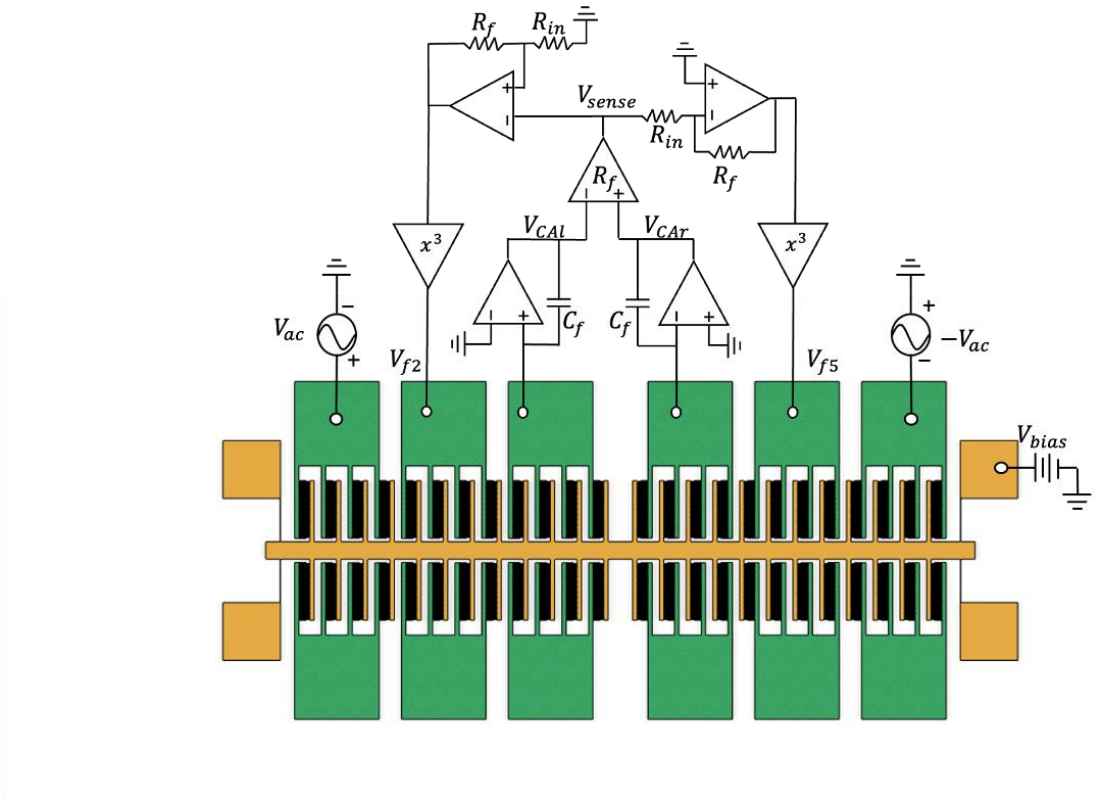

Figure 5.1: Block diagram of the stiffness tunable MEMS resonator. There are 6 pads connected to the fixed-comb-fingers arrays, chosen for driving, sensing, and feedback. Besides, the movable comb-fingers are all biased with a DC voltage. For the driving purpose, the differential AC voltages V_{ac} and $-V_{ac}$ are applied to pads 1 and 6, which will generate a total electrostatic force linearly proportional to the amplitude of the AC voltage. For the sensing purpose, the two identical charge amplifiers are connected to pads 3 and 4, forming a differential charge sensing structure. The sensed voltage V_{sense} is linearly proportional to the displacement of the proof mass, which will then be split into a pair of differential signals and cubed to generate the feedback voltage V_{f2} and V_{f5}.

The parameters used in our test case are: flexure width w = 3μm, thickness h = 25μm, and length L = 300μm; the two pairs of N = 200 finger comb drive arrays have initial finger overlap length l_0 = 20μm, finger width w_f = 2μm, and gap g = 2μm; Young's modulus E = 160GPa, density ρ = 2300kg/m^3, structure-to-substrate gap g_{sub} = 2μm,

viscosity $\mu = 1.75\times10^{-5}$sPa , and proof mass area $a_{pf} = 1.19\times10^{-6}$ m^2 (including flexures and combs). This yields a compact mass of M = $\rho \times volume$ = 6.87×10^{-8} kg, and stiffness of $K = \frac{4Ehw^3}{L^3} = 16\,\mathrm{N/m}$. The damping at standard atmospheric pressure is $D = \mu a_m / g_{sub} = 1.04\times10^{-5}\,\mathrm{Ns/m}$, with a quality factor of $Q \approx \omega_0 M/D$ = 101 in air. Static capacitance is $C_0 = \frac{\varepsilon_0 h l_0 N}{g} = 0.44\mathrm{pF}$, where the permittivity of the medium is $\varepsilon_0 = 8.854\times10^{-12}$ F/m. The driving force is $F_{dr} = \frac{1}{2}\frac{C_0}{l_0}V_{dr}^2$.

To drive the MEMS resonator to vibrate and achieve the linear voltage-force relationship, differential AC+DC driving voltage will be applied to pads 1 and 6:

Pad1:

$$V_{dr1} = V_{ac} - V_{bias} = A\sin(\omega t) - V_{bias} \tag{5.1}$$

Pad6:

$$V_{dr6} = -V_{ac} - V_{bias} = -A\sin(\omega t) - V_{bias} \tag{5.2}$$

where the Vac is the AC voltage, whose amplitude is A and frequency is ω, and V_{bias} is the DC voltage applied to moveable comb-fingers.

Since pad 1 and pad 6 have comb-fingers pointed in the opposite direction, the total driving force will be the subtraction of the electrostatic force generated by pad 1 and pad6:

$$F_{dr} = \frac{C_0 V_l^2}{2l_0} - \frac{C_0 V_r^2}{2l_0} = 2\frac{C_0}{l_0}AV_{bias}\cos(\omega_n t)[\mathrm{N}] \tag{5.3}$$

When the frequency of the exciting voltage is equal to the effective resonate frequency ω_{eff}, the steady state amplitude of displacement is:

$$|x(t)| = \frac{|F_{dr}|Q}{\omega_{eff}^2 M} \tag{5.4}$$

When the driving force drives the resonator F_{dr}, the changing of fixed-movable comb-finger capacitor overlap areas will cause the accumulated charge changing on pad 3 and pad 4, which is described as:

Pad3:

$$q_3 = \frac{\varepsilon_0 \varepsilon_r h(l_0 + x(t))N}{g} V_{bias} \tag{5.5}$$

Pad4:

$$q_4 = \frac{\varepsilon_0 \varepsilon_r h(l_0 - x(t))N}{g} V_{bias} \tag{5.6}$$

The charge will then be picked up and amplified by the charge amplifier. A differential charge amplifier structure is adopted to reduce the parasitic capacitance effect. The sensing equation is expressed as follows:

$$V_{sense} = V_{CAl} - V_{CAr} = \frac{q_l}{C_f} - \frac{q_r}{C_f} = \frac{2\varepsilon_0 \varepsilon_r h x(t)}{g} \times \frac{V_{bias}}{C_f} \tag{5.7}$$

Eq (5.7) suggested that the sensed voltage V_{sense} is directly proportional to the displacement $x(t)$. The sensed voltage will then be split into two differential signals amplified with the same gain G_f. The feedback voltages applied to pad 2 and pad 5 are expressed as:

Pad2:

$$V_{f2} = G_f V_{sense}^3 - V_{bias} \tag{5.8}$$

Pad5:

$$V_{f5} = -G_f V_{sense}^3 - V_{bias} \tag{5.9}$$

The electrostatic feedback force generated by the feedback voltage is then described as:

$$F_{fb} = \frac{1}{2}\frac{C_0}{l_0}V_{f2}^2 - \frac{1}{2}\frac{C_0}{l_0}V_{f5}^2 = 2\frac{C_0}{l_0}G_f V_{bias} V_{sense}^3 = 16G_f \frac{C_0^4}{l_0^4}\frac{V_{bias}^2}{C_f^3}x^3(t) \tag{5.10}$$

Substituting eq (5.10) into eq (3.15), the governing equation of the stiffness tunable system is:

$$M\ddot{x}(t) + D\dot{x}(t) + Kx(t) = F_{dr} + F_{fb} = 2\frac{C_0}{l_0}AV_{bias}\cos(\omega_n t) + 16G_f \frac{C_0^4}{l_0^4}\frac{V_{bias}^4}{C_f^3}x^3(t) \tag{5.11}$$

Therefore, the electrically generated nonlinear stiffness is $\kappa_e = 16G_f \frac{C_0^4}{l_0^4}\frac{V_{bias}^4}{C_f^3}$.

5.2 Simulation

In this section, the nonlinear resonator system is simulated with Simulink. **Figure 5.2** shows the simulation setup in Simulink.

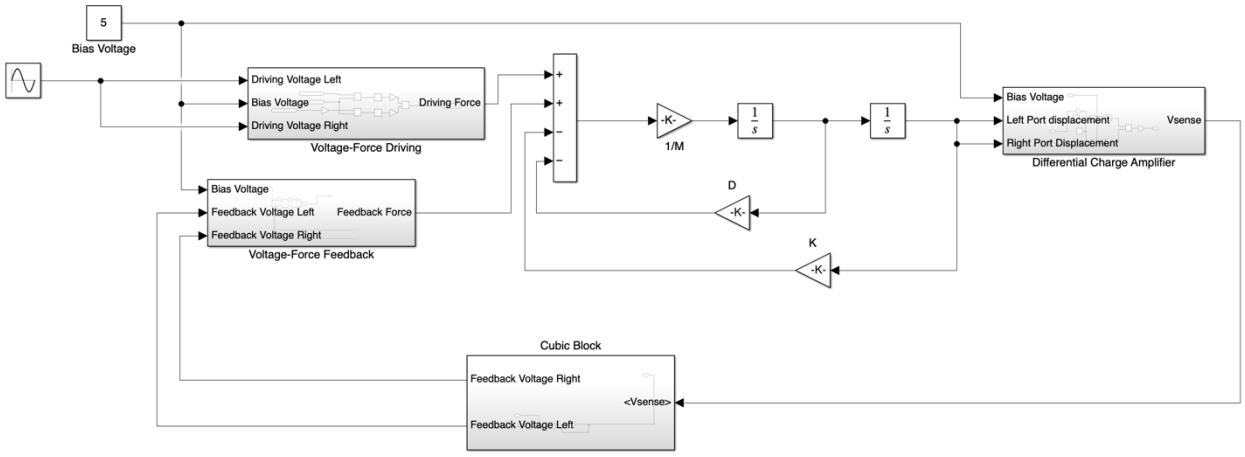

Figure 5.2: Simulation setup in Simulink. The mechanical spring-mass-damper system of the MEMS resonator is represented by the second-order system with two integrators. The voltage-force driving and voltage-force feedback blocks represent the voltage-to-force relationship at the ports. The differential charge amplifier represents the

displacement to voltage conversion. Lastly, the cubic block cube sensed the voltage signal and processed it to generate differential feedback voltages.

5.2.1 Transient behavior

By applying a constant driving frequency of 2453Hz and a magnitude of 1V of AC voltage, the transient simulation result can reveal the start-up oscillation process, which took 15s to stabilize. At t=15s, the driving voltage is set to 0, which will cause the amplitude of displacement to decay with time. By fitting the envelope of the decay curve to the displacement amplitude, the simulated damping coefficient will be 0.3979, which is comparable to the analytical result of $\zeta = D/2M = -0.396$.

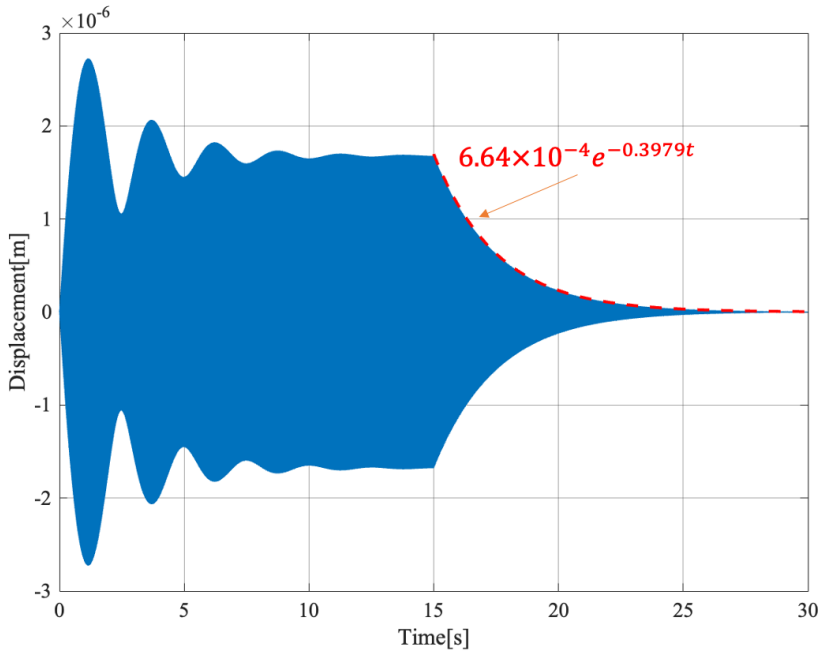

Figure 5.3: Transient simulation result. At t=0s, the system is driven with an AC voltage with an amplitude of 1V and frequency of 2453Hz. After 15s, the system reaches a steady state, which gives the steady state amplitude of 1.67um. At t=15s, the power is turned off, which causes the displacement amplitude to decay. By fitting the decay curve to the response envelope, the decay rate is determined to be 0.3979.

A driving voltage with increasing frequency is applied to show the nonlinear system's jump-down phenomena. At t=0s, the excitation frequency is set to be 2440Hz, which is simulated for 10s to let the system reach a steady state. At t=10s, the excitation frequency will be increased with a step size of 1Hz. The final state of each step is used as the initial state for the next step. Repeating such a procedure will cause the jump-down phenomenon. As shown in **Figure 5.4**, when the driving voltage is 0.2V, and the nonlinear feedback gain is 5, the jump-down phenomenon happens at a frequency of 2.466kHz.

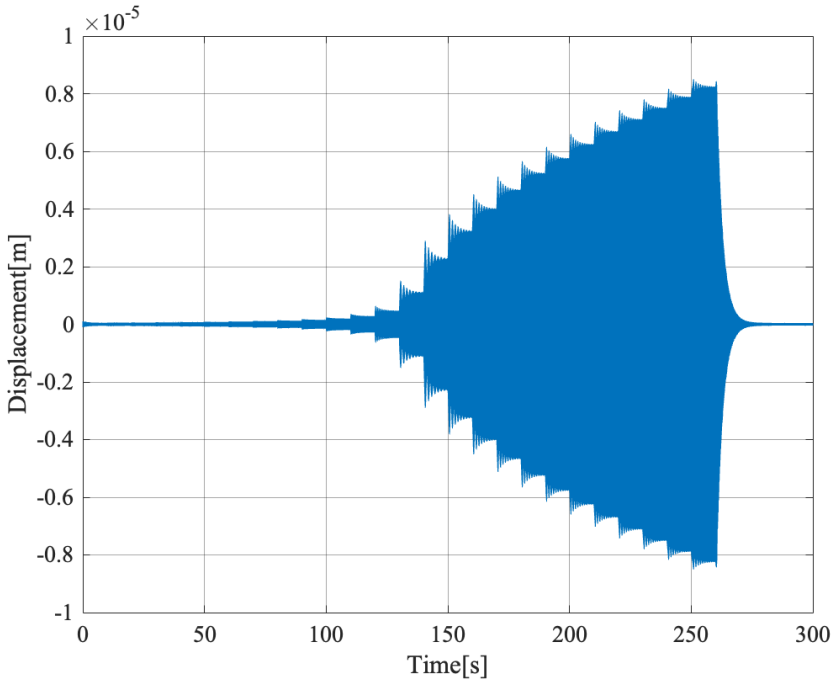

Figure 5.4: Result of TA when sweeping the driving voltage's frequency from 2440Hz to 2470Hz. The nonlinear system is swept from 2440Hz to 2470Hz with a step size of 1Hz. To make sure the response reaches steady state, each step was simulated for 10s. Meanwhile, to make the sweeping continuous, the end state of each step is used for the initial state of the next step. The jump-down phenomenon occurs at t=260s, corresponding to the driving frequency of 2.466kHz.

5.2.2 The frequency characteristic

Figure 5.5 shows the amplitude and phase response of the artificial nonlinear stiffness. Through tuning the gain Gf of the nonlinear feedback path, the artificial nonlinear stiffness value is changed from 2.11×10^{10} N/m^3 to 3.74×10^{10} N/m^3, corresponding to the feedback voltage value increased from 3.1V to 5.5V. Furthermore, to show the influence of the amplitude of the driving force on the jump-down frequency, for a constant nonlinear stiffness value of $\beta = 2.11\times10^{10}$, the amplitude of the driving voltage is increased from 0.02V to 0.027V.

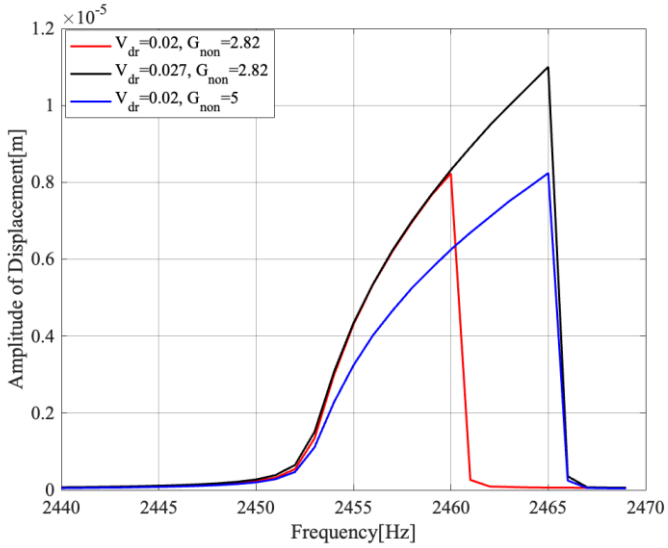

Figure 5.5: Frequency responses of the nonlinear PODMEMS. Comparing the red and black curve, the effective nonlinear stiffness is the same, while the amplitude of the driving frequency is increased from 0.02V to 0.027V, and the jump-down frequency is increased from 2.459kHz to 2.464kHz. On the other hand, comparing red and blue curves, the amplitude of driving frequency is constant, while the feedback voltage is increased, also causing the jump down frequency 2.459kHz to 2.464kHz.

5.2.3 Thermal drift

Using our verification between expected analytical modeling behavior and our numerical modeling testbed, we now investigate how temperature changes affect our PODMEMS test case subject to artificial vacuuming and stiffening. Thermal expansion of length, width, and thickness of flexure, as well as the effect of temperature on Young's modulus, is modeled as

$$K(T) = \frac{E(T)h(T)}{4}\left(\frac{w(T)}{L(T)/2}\right)^3 \tag{5.12}$$

where

$L(T) = L_0(1+\alpha\Delta T)$, $w(T) = w_0(1+\alpha\Delta T)$, $h(T) = h_0(1+\alpha\Delta T)$, and

$$E(T) = 145\times10^9 \exp\left(2.61\times\frac{10^{-3}eV}{k_B T}\right)[Pa]$$

and where the coefficient of thermal expansion of silicon is $\alpha = 2.6\times10^{-6}\,\mathrm{K}^{-1}$, the reference geometry at 300K is L_0, w_0, h_0, electron volts is $eV = 1.6\times10^{-19}\,\mathrm{J}$, and Boltzmann constant is $k_B = 1.38\times10^{-23}\,\mathrm{J/K}$.

According to eq (5.12), when the temperature is increased from 300K to 310K, the resonance frequency of the MEMS resonator used for the test is decrease by 5Hz. Therefore, when a constant driving frequency of 2449Hz is applied to the linear model and detuned to the frequency of 2460Hz for the nonlinear model, the thermal drift will cause the linear model's amplitude to drop by 98.5% (36dB) and causes the nonlinear model's amplitude to drop by 18.9% (1.8dB).

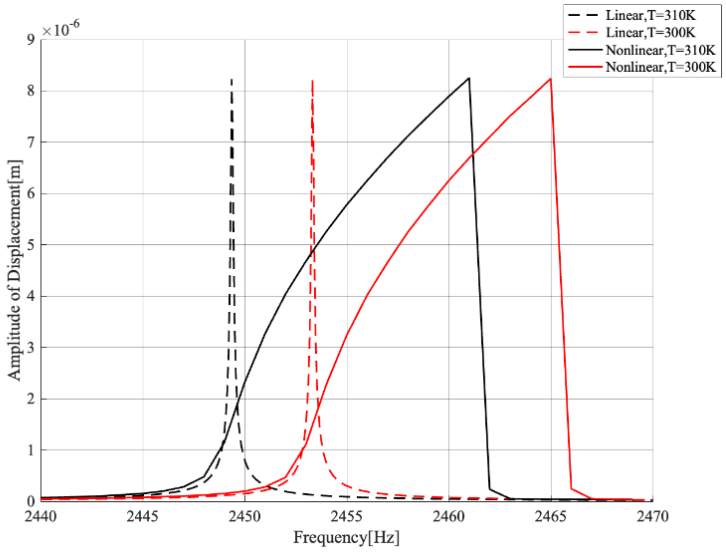

Figure 5.6: Frequency response of linear and nonlinear Simulink models of PODMEMS undergoing thermal drift. A constant driving frequency of 2.449kHz is applied to the linear model and detuned to the frequency of 2.460kHz for the nonlinear model, where a decrease in temperature of 10K results in a resonance frequency increase of about 5Hz. Such drift causes the linear model's amplitude to drop by 98.5% (36dB) and causes the nonlinear model's amplitude to drop by 18.9% (1.8dB).

5.3 Conclusion

This chapter proposed a method to address a MEMS resonator's output amplitude stability issue due to thermal drift. For a MEMS resonator with high Q, a small temperature change can cause the resonator to lose resonance by falling below cutoff frequency amplitudes. However, the amplitude can remain above the cutoff by controllably bending the response curve through artificial damping.

Chapter 6

Artificial Vacuum and Nonlinear Stiffness

Matching the drive frequency to the resonance frequency of narrow bandwidth, high-Q microstructure subject to thermal drift can be difficult. We, therefore, study the effect of applying artificial nonlinear stiffness to maintain high Q while widening the bandwidth. Doing so enables the amplitude of motion to remain large while the structural resonance frequency drifts and the drive frequency remains constant. Previously we showed how a MEMS device's apparent mass, damping, and stiffness could be linearly increased or decreased using electrostatic force feedback. Here, we use electrostatic feedback force to generate apparent nonlinear stiffness mimicking a Duffing oscillator's nonlinear stiffness that is strongly cubic in displacement at low amplitude. To achieve high Q in the absence of a vacuum, we apply negative damping feedback such that the total apparent damping is near zero. We simulate a MEMS oscillator's feedback circuit and an equivalent circuit model subject to noise, parasitic capacitance, leaking current, and thermal drift. We validate the simulation using analytical methods. Our results suggest that artificial nonlinear stiffness can help maintain a large oscillation amplitude while resonance frequency drifts about a constant drive frequency. The rest of the chapter is organized as follows. In **Section 6.1**, we introduce and verify our nonlinear stiffness feedback model. Section 6.2 demonstrates how such nonlinear feedback maintains large amplitudes during resonance frequency shifts due to temperature changes. Last, we summarize our findings in **Section 6.3**. The nomenclature used in this study is provided in **Table 1**.

Table 6.1: Nomenclature of artificial nonlinear stiffness and vacuum system

Parameter	Value	Unit	Description
a_m	1	atm	Standard atmospheric pressure
C_1	0.5	F	Capacitor of equivalent circuit
C_p	1×10^{-9}	F	Parasitic capacitor
D	1.55×10^{-7}	Ns/m	Damping
D_e	1.548×10^{-7}	Fs/m	Electrical damping
E	1.6×10^{11}	Pa	Young's modulus
ε_0	8.854×10^{-9}	F/m	Permittivity of free space
g	2×10^{-6}	m	Gap between comb fingers
g_{sub}	2×10^{-6}	m	Substrate-to-substrate gap
G_{amp}	1×10^{3}	1	Gain of pre-amplifier
G_D	1×10^{3}	1	Gain of damping amplifier
$G_{F/C}$	1	F/C	Unit converter
G_{Fm^2/CV^2}	1	Fm^2/CV^2	Unit converter
$G_{FN/m}$	1	FN/m	Unit converter
$G_{H/Kg}$	1	H/Kg	Unit converter
G_{int}	1×10^{3}	1/s	Gain of integrator
G_κ	8.85×10^{5}	$1/V^2$	Gain of cubic amplifier

$G_{mN/FV}$	1	mN/FV	Unit converter
G_{sq}	1.3	1/V	Gain of square root amplifier
G_{sqrt}	1	$V^{1/2}$	Gain of square amplifier
G_{TIA}	1×10^{5}	V/A	Gain of TIA
$G_{\Omega m/Ns}$	1	Ωm/Ns	Unit converter
h	20×10^{-6}	m	Thickness of folded flexure
K	2	N/m	Stiffness
κ	0	F/m^3	Mechanical nonlinear stiffness
κ_e	1×10^{9}	F/m^3	Electrical nonlinear stiffness
L	294.7×10^{-6}	m	Length of folded flexure
L_1	8×10^{-10}	H	Inductor of equivalent circuit
L_f	20×10^{-6}	m	Length of comb finger
M	8×10^{-10}	Kg	Mass
N	100	1	Comb finger numbers
ρ	2300	Kg/m^3	Density
R_1	1.55×10^{-7}	Ω	Resistor of equivalent circuit
R_{p1}	1×10^{-9}	Ω	Parasitic resistance

R_{p2}	1×10^{-3}	Ω	Parasitic resistance
τ_1	3.2×10^{-9}	s	Latency of equivalent circuit
τ_2	2.2×10^{-9}	s	Latency of TIA circuit
τ_3	1.2×10^{-9}	s	Latency of integrator circuit
τ_4	8×10^{-10}	s	Latency of cubic circuit
τ_5	8×10^{-11}	s	Latency of parasitic elements
τ_6	3×10^{-9}	s	Latency of square root circuit
τ_7	3×10^{-9}	s	Latency of square circuit
μ	1.75×10^{-5}	sPa	viscosity
V_{noise}	1×10^{-9}	V	Noise source
w	2×10^{-6}	m	Width of folded flexure
w_f	2×10^{-6}	m	Width of comb finger

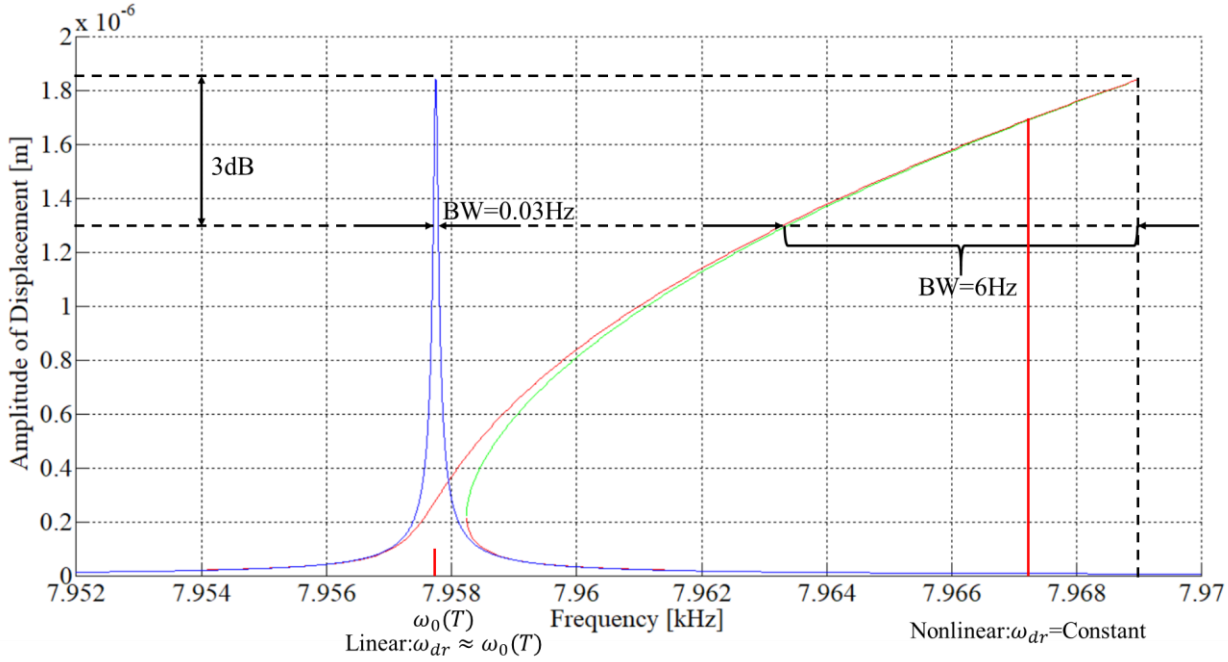

Figure 6.1: The bandwidth, driving frequency, and quality factor of a linear (blue) vs nonlinear (red) MEMS oscillator.

6.1. Electronic feedback components for artificial nonlinear stiffness

In this section, we present a set of analog circuit components that, when integrated, can generate the type of electrostatic force feedback needed to achieve near-zero damping and large nonlinear stiffness. By feeding back an amplified electrostatic force onto the proof mass proportional to the displacement's cubic, nonlinear Duffing characteristics can be produced at low amplitudes. For nonlinear stiffness, let's define it as the derivative of the elastic restoring force with respect to displacement:

$$K_{nonlinear} = \frac{d}{dx} F_K = \frac{d}{dx}\left(Kx + \kappa x^3\right) = K + 3\kappa x^2 . \tag{6.1}$$

The equation of motion of the MEMS structure shown in **Figure 3.1** without feedback is

$$M\ddot{x} + D\dot{x} + \left(K + 3\kappa x^2\right)x = F_{dr} . \tag{6.2}$$

By including feedback for damping D_e and nonlinear stiffness κ_e we have

$$M\ddot{x}+\left(D-D_e\right)\dot{x}+\left(K+3\kappa x^2+\kappa_e x^2\right)x=F_{dr}\,, \tag{6.3}$$

which is a form that ignores feedback latency τ for simplicity. By explicitly including latency, eq (6.3) is expressed as

$$M\ddot{x}\left(t\right)+D\dot{x}\left(t\right)-D_e\dot{x}\left(t-\tau\right)+Kx\left(t\right)+3\kappa\left[x\left(t\right)\right]^3+\kappa_e\left[x\left(t-\tau\right)\right]^3=F_{dr}\,, \tag{6.4}$$

where $x\left(t\right)$ is the position at the time t, and $x\left(t-\tau\right)$ was the position about several nanoseconds ago.

Using the ready-made circuit models in HSPICE that include latency, and components for noise and parasitics, we model and simulate our nonlinear feedback circuit together with an equivalent circuit representation of the MEMS device. Our analytical circuit model expression of the MEMS device with feedback circuit has the form：

$$L\frac{di}{dt}+Ri+\frac{1}{C}\int i dt=\frac{N\varepsilon_0 h}{g}\left(\sqrt{V_{dr}-G_{\tau D}R_{TIA}G_{amp}i-G_{\tau\kappa}\left[G_{\text{int}}\int R_{TIA}G_{amp}i\,dt\right]^3}\right)^2 \tag{6.5}$$

where $L=M$, $R=D$ and $C=1/K$; that is, the inductor, resistor, and capacitor represent the mass, damping, and stiffness. The velocity $\dot{x}$ and drive force F_{dr} are represented by current i and drive voltage V_{dr}. The quantities G_{amp}, R_{TIA}, $G_{\tau D}$, and $G_{\tau\kappa}$ are the amplification of pre-amplifier, transimpedance amplifier (TIA), damping amplifier, and nonlinear stiffness amplifier. From eq (6.5), right-hand terms for force, damping, and nonlinear stiffness are

$$\begin{cases} F_{dr} = \dfrac{N\varepsilon_0 h}{g} V_{dr} \\ F_D = \dfrac{N\varepsilon_0 h}{g} G_{\tau D} R_{TIA} G_{amp} i \\ D_e = \dfrac{N\varepsilon_0 h}{g} G_{\tau D} R_{TIA} G_{amp} \\ F_\kappa = -\dfrac{N\varepsilon_0 h}{g} G_{\tau\kappa} \left[G_{\text{int}} \int R_{TIA} G_{amp} i\, dt \right]^3 \\ x = \int i\, dt \\ \kappa_e = \dfrac{N\varepsilon_0 h}{g} G_{\tau\kappa} G_{\text{int}} \left(R_{TIA} G_{amp} \right)^3 . \end{cases} \tag{6.6}$$

From eq (6.6) it is seen that the magnitude of the artificial nonlinear stiffness is independently controlled by $G_{\tau\kappa}$ and G_{int}, and that of the damping is independently controlled by $G_{\tau D}$. A block diagram of the feedback circuit is shown in **Figure 6.2**.

The parameters used in our PODMEMS test case are: folded flexure width w = 2μm, thickness h = 20μm, and length L = 294.7μm; the two pairs of N = 100 finger comb drive arrays have finger length L_f = 20μm, finger width w_f = 2μm, and gap g = 2μm; Young's modulus E = 160GPa, density ρ = 2300kg/m^3, structure-to-substrate gap g_{sub} = 2μm, viscosity $\mu = 1.75\times10^{-5}$ sPa, and proof mass area $a_m = 1.74\times10^4$ μm^2 (including flexures and combs). This yields a compact mass and stiffness of M = $\rho \times$ *volume* = 8×10^{-10} kg, and K = $Ehw^3/4/(L/2)^3$ = 2N/m. The damping at standard atmospheric pressure is $D = \mu a_m / g_{sub}$ = 1.55×10^{-7} Ns/m, with a quality factor of $Q \approx \omega_0 M/D$ = 258 in air. The driving force is $F_{dr} = \left(N\varepsilon_0 h/g\right) V_{dr}^2$, where the number of fingers $N = 100$ and the permittivity of the medium is $\varepsilon_0 = 8.854\times10^{-12}$ F/m.

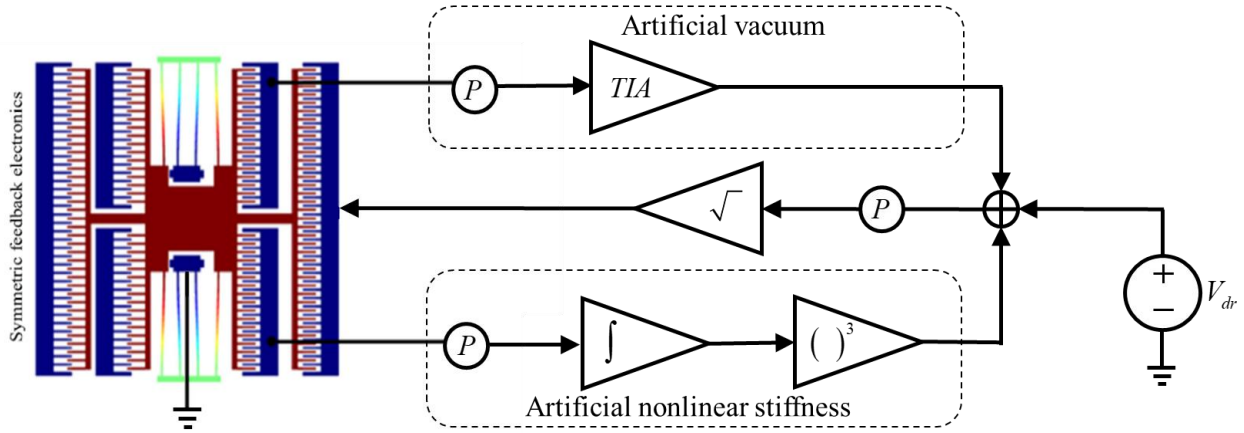

Figure 6.2: System block diagram of the artificial damping and nonlinear stiffness feedback system. The output signal from velocity is integrated and cubed. The square root component outputs a signal that is the square root of voltage since the applied force is proportional to the square of the voltage. For simplicity, the structural design shown here has a smaller number of comb fingers than our test case. The circuits that make up the component blocks of this system are shown in **Figures 6.3-6.10**.

MEMS block. The equivalent circuit models the mechanical system with electronic elements and the corresponding relationship between mechanical domain and electrical domain parameters are listed as in eq (6.7):

$$L_1 = M G_{\mathrm{H/kg}},\ R = D G_{\Omega\mathrm{m/Ns}},\ C_1 = G_{\mathrm{FN/m}} / K. \tag{6.7}$$

Our analytical model for the MEMS equivalent circuit block is

$$L_1 \frac{d}{dt} i_{out} + R_1 i_{out} + \frac{1}{C_1} \int i_{out} dt = \frac{N \varepsilon_0 h}{g} \left(\sqrt{V_{in}} \right)^2 \tag{6.8}$$

where our transduction model between the electrical and mechanical domains is eq (6.9), and the block's HSPICE circuit, numerical simulation, and verification are shown in **Figure 6.3**.

$$F_{in} = \left(\frac{N \varepsilon_0 h}{g} G_{\mathrm{mN/FV}} \right) V_{in} \text{ and } \dot{x}_{out} = \left(\frac{g}{N \varepsilon_0 h} G_{F/C} \right) i_{out}. \tag{6.9}$$

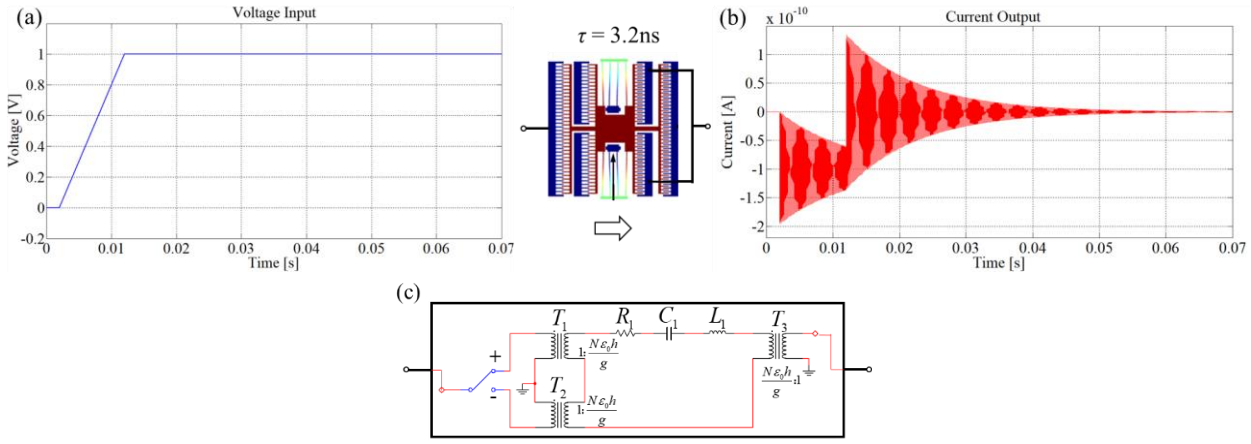

Figure 6.3: MEMS equivalent circuit. The purpose of the MEMS equivalent circuit is to simulate the integrated structure and feedback electronics in the same numerical modeling and simulation domain. A test input signal is shown in (a), and its simulated output is shown in (b). The component contributes a latency of 3.2ns between its input and output signal. The circuit model of the equivalent circuit is shown in (c). The circuit works by simulating the mechanical system's mass, damping, and stiffness with the inductor, resistor, and capacitor. The pull-left and pull-right forces are generated by the transformers that represent the comb drives that can only pull.

TIA block. Our analytical transduction model of the transimpedance amplifier is eq (6.10) , and the block's circuit, numerical simulation, and verification are shown in **Figure 6.4**.

$$\dot{x}_{in} = \left(\frac{g}{N\varepsilon_0 h} \frac{G_{\mathrm{F/C}}}{G_{amp} G_D} \right) i_{in} \text{ and } V_{out} = G_{TIA} i_{in}. \tag{6.10}$$

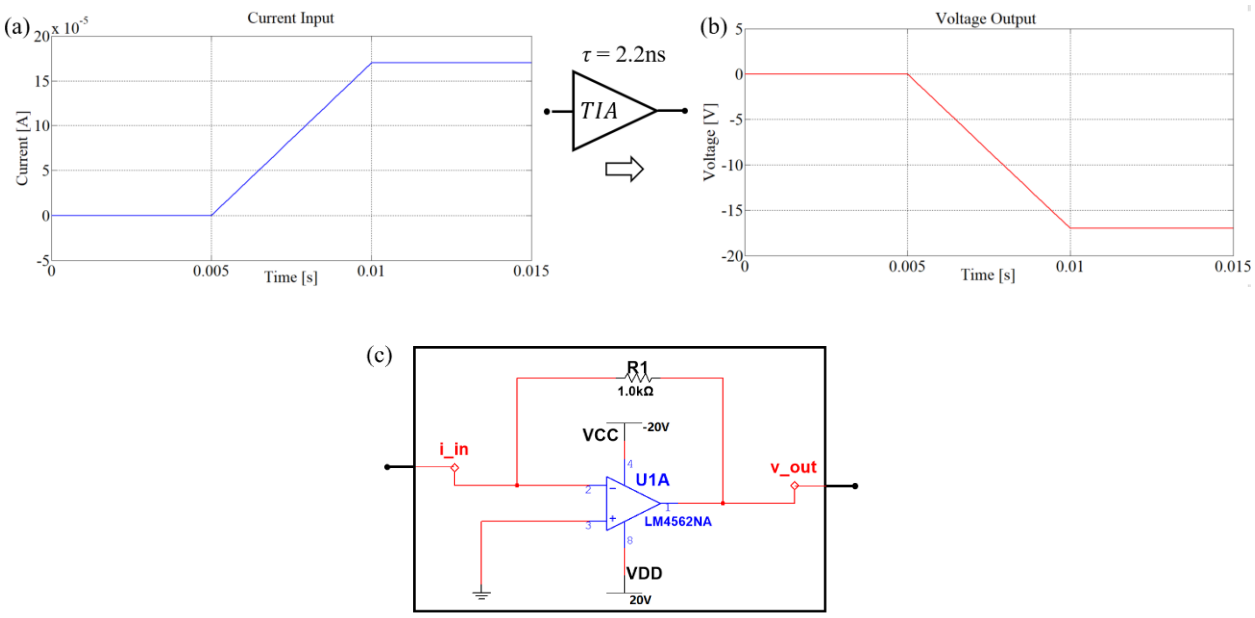

Figure 6.4: Transimpedance amplifier (TIA) component. The purpose of the TIA component is to convert the comb drive current (proof mass velocity) to a voltage. A test input signal is shown as in (a), and its simulated output is shown as in (b). The component contributes a latency of 3.2ns between its input and output signal. The circuit model of the equivalent circuit is shown in (c). The circuit works by using a resistor as the feedback loop of the operational amplifier. Consequently, the current that goes through the resistor will cause a voltage drop upon the resistor, which then will be shown as a voltage in the output of opamp that is proportional to current. Due to the limitation of the bandwidth and supply power of the opamp, the gain will not be infinite for an ideal opamp. A multistage TIA may be adopted to distribute the gain of each TIA.

Integrator block. Our analytical transduction model of the integrator is eq (6.11) and the block's circuit, numerical simulation, and verification are shown in **Figure 6.5**.

$$\dot{x}_{in} = \left(\frac{g}{N\varepsilon_0 h G_{amp}} G_{F/C} \right) i_{in}, \; x_{out} = \left(\frac{g}{N\varepsilon_0 h G_{amp} G_{\text{int}}} G_{\text{F/C}} \right) i_{out}, \text{ and } i_{out} = G_{\text{int}} \int i_{in}\, dt. \tag{6.11}$$

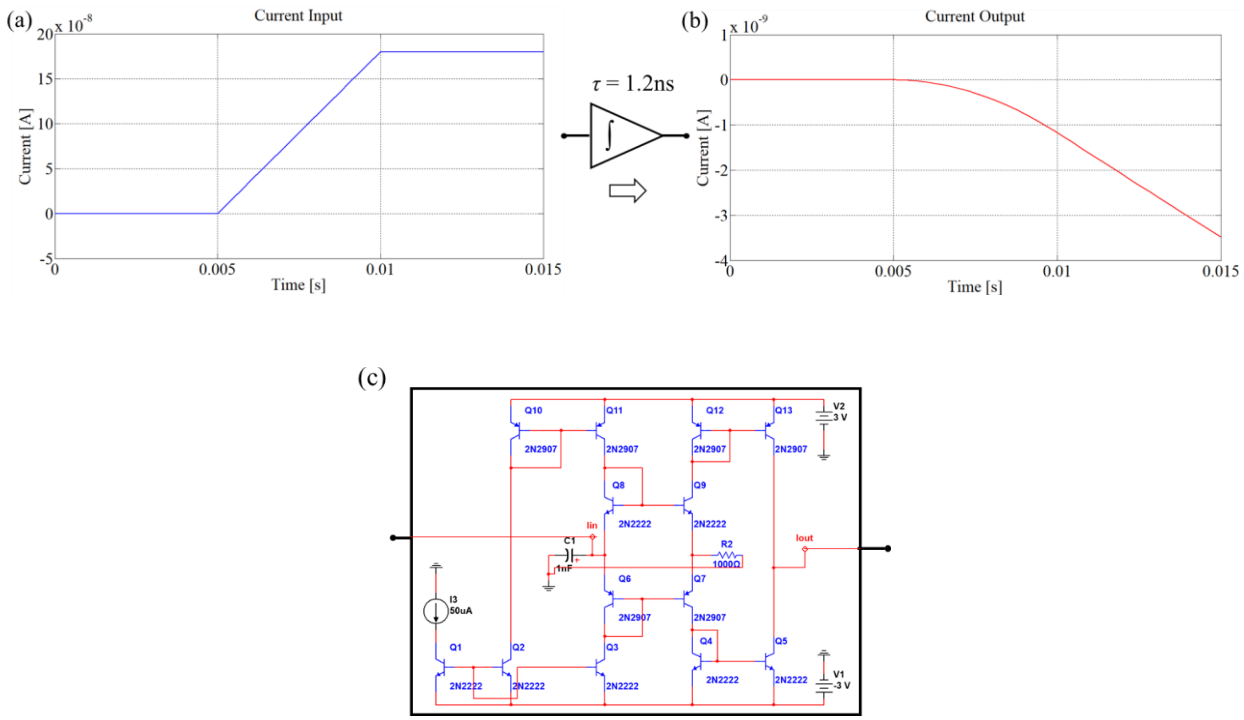

Figure 6.5: Integrator component. The purpose of the integrator component is to convert the velocity of the proof mass (comb drive current) to a displacement. A test input signal is shown as in (a), and its simulated output is shown as in (b). The component contributes a latency of 1.2ns between its input and output signal. The circuit model of the equivalent circuit is shown in (c). The circuit works by using the current conveyor II (CCII) structure, which is an open-loop current-mode amplifier with low and fixed current gain. A typical CCII is a three terminal device, with the terminals designated X, Y, Z. If a voltage is applied to Y, an equal potential will appear on the input terminal X. The current that goes through X will then be conveyed to output terminal Z, such that Z has the characteristic of the current source, of value I, with high output impedance. Therefore, CCII has similar behavior with an op-amp, except that the CCII structure has a higher voltage gain over a larger signal bandwidth than the corresponding op-amp. By connecting a capacitor from X to the ground and a resistor from Y to ground, the output current will be an integrated input current signal.

Cubic block. Our analytical transduction model of the cubic block eq (6.12) and the block's circuit, numerical simulation, and verification are shown in **Figure 6.6**.

$$x_{in} = \left(\frac{g}{N\varepsilon_0 h G_{amp} G_{\text{int}} G_{TIA}} G_{\text{F/C}} \right) V_{in} \quad , \quad x_{out} = \sqrt[3]{\left(\frac{g}{N\varepsilon_0 h G_{amp} G_{\text{int}} G_{TIA} G_{\kappa}} G_{\text{Fm}^2/\text{CV}^2} \right) V_{out}} \quad , \quad \text{and}$$

$$V_{out} = G_{\kappa} \, (V_{in})^3 . \tag{6.12}$$

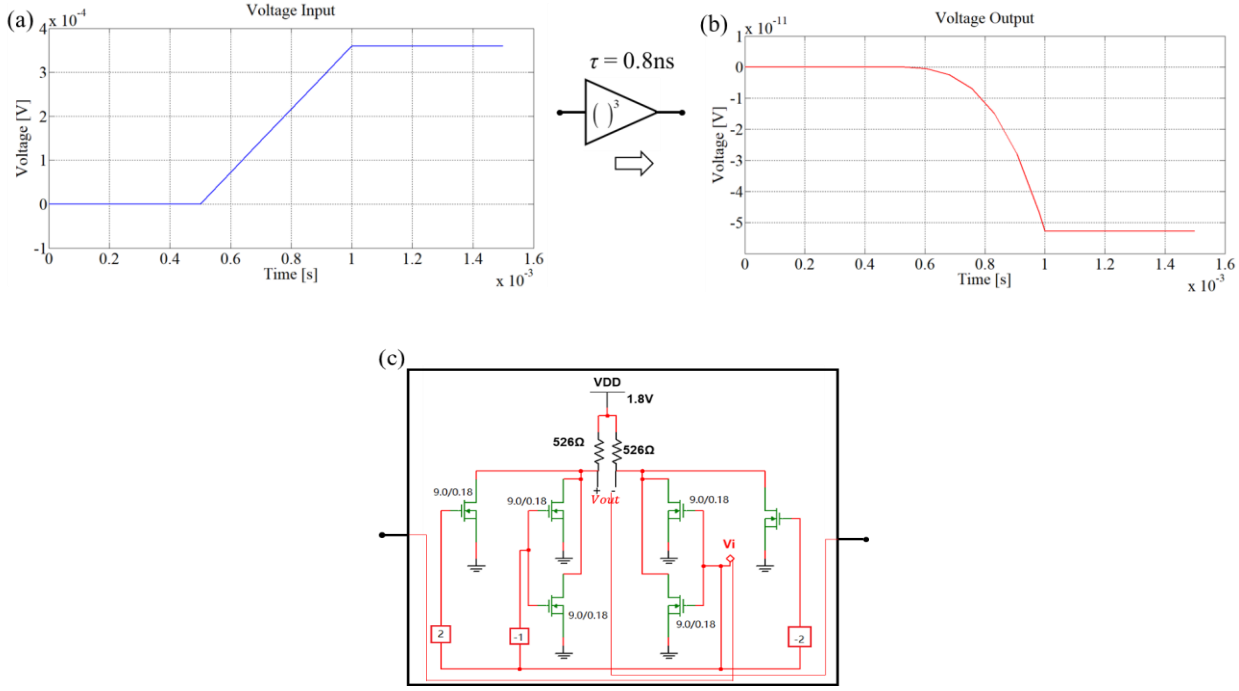

Figure 6.6: Cubic component. The purpose of the cubic component is to cube the displacement. A test input signal is shown as in (a), and its simulated output is shown as in (b). The component contributes a latency of 0.8ns between its input and output signal. The circuit model of the equivalent circuit is shown in (c). The circuit works by using the characteristic of CMOS under weak inversion. When CMOS is working under weak inversion status, a Taylor series can express the gate voltage-drain current's relationship. By using differential pair transistors, the even-ordered powers of the Taylor series can be canceled, while higher-order odd powers of the Taylor series are negligible. Therefore, the desired cubic term can be isolated by using an analog adder configuration of transistors with specific input voltage combinations to cancel the first-order terms. For the reason that CMOS needs to work under weak inversion status, the input level is limited to no larger than 300mV for the circuit shown in (c).

Parasitic block. Our analytical transduction model of the cubic block eq (6.13) and the block's circuit, numerical simulation, and verification are shown in **Figure 6.7**.

$$V_{out} = \left(1 + R_{2p} / R_{1p} + R_{2p} C_p s\right) V_{in} + V_{noise} \tag{6.13}$$

where R_{1p} and R_{2p} are the leakage resistances, C_p is the parasitic capacitance, and V_{noise} is noise.

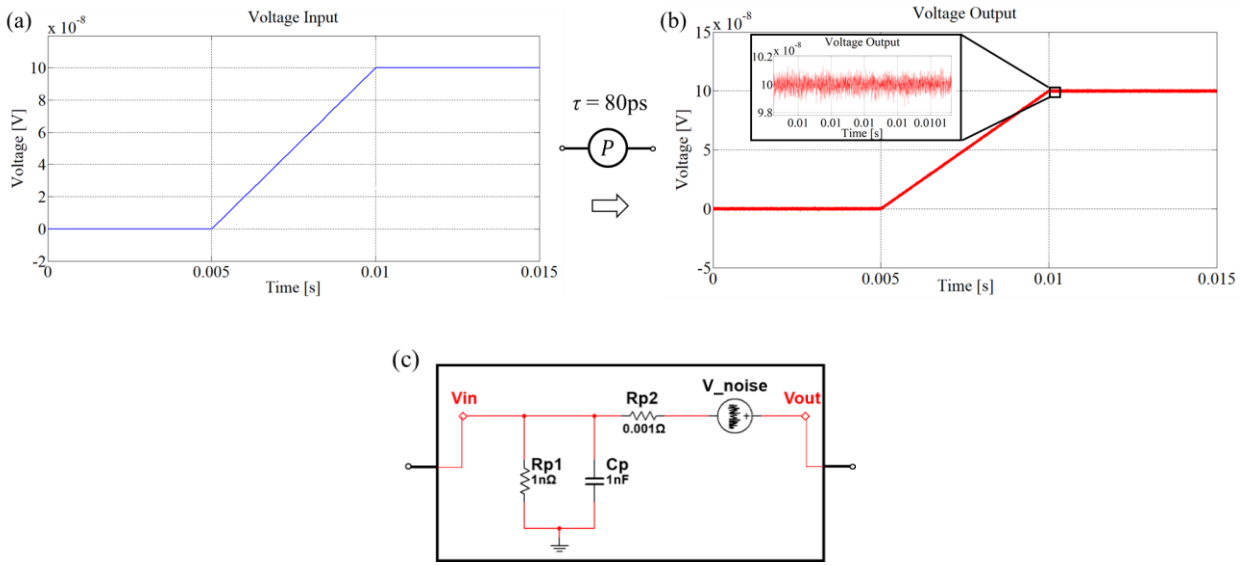

Figure 6.7: Parasitic component. The purpose of the parasitic component is to simulate the nonideal leakage current, parasitic capacitance, and noise. A test input signal is shown as in (a), and its simulated output is shown as in (b). The component contributes a latency of 80ps between its input and output signal. The circuit model of the equivalent circuit is shown in (c). The circuit works by using a parallel resistor, capacitor, and series resistor to represent the parasitic resistance and capacitance, and by using a noise voltage source to simulate the noise in the circuit.

Square root block. Our analytical transduction model of the square root block eq (6.14) and the block's circuit, numerical simulation, and verification are shown in **Figure 6.8**.

$$V_{out} = G_{sqrt} \sqrt{V_{in}} \ . \tag{6.14}$$

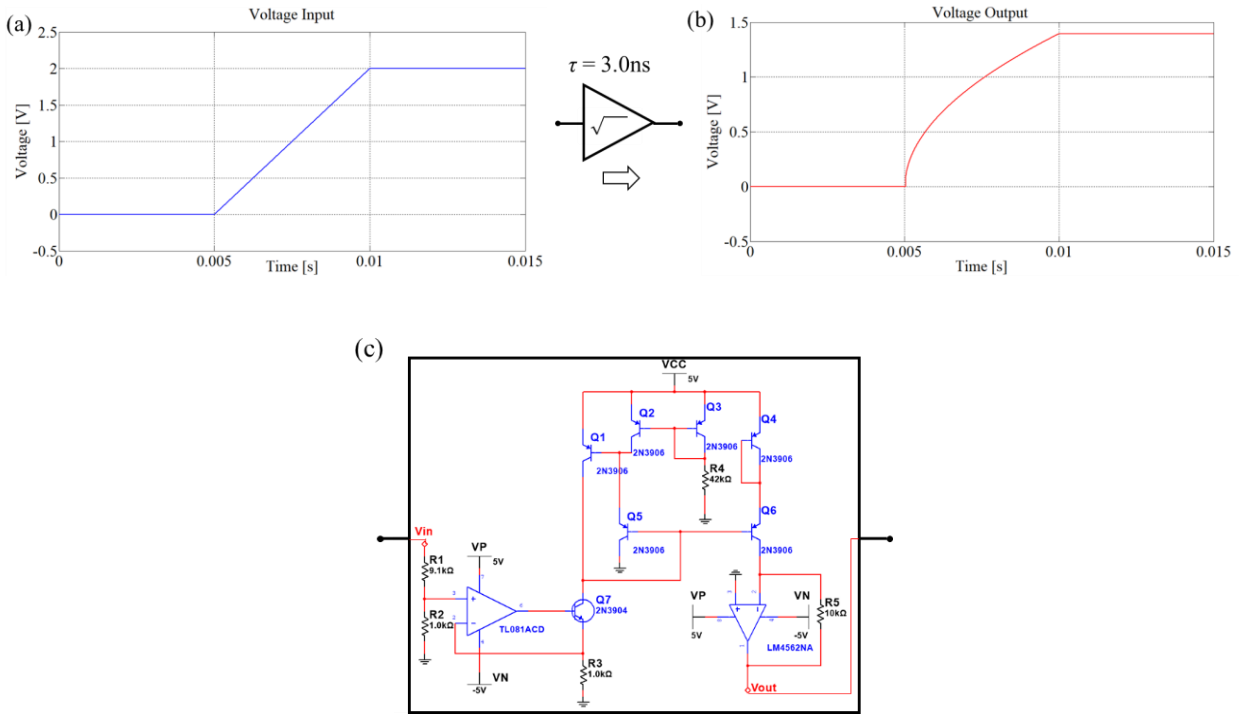

Figure 6.8: Square root component. The purpose of the square root component is to square root the feedback voltage because the comb drive subsequently squares the voltage, which then results a force that is desirable proportional to voltage. A test input signal is shown as in (a), and its simulated output is shown as in (b). The component contributes a latency of 3.0ns between its input and output signal. The circuit model of the equivalent circuit is shown in (c). The circuit works by using the translinear principle of BJT which works under weak inversion. When a BJT is working under weak inversion status, the base-emitter voltage and collector current are exponentially related. By building a loop with four BJTs inside, at the common collector point, using Kirchhoff's law, the collector-emitter current of these BJTs can be expressed as: $I_1 \times I_2 = I_{bias} \times I_3$, where I_{bias} is provided by a current source. Connecting two BJTs with emitter to collector, the collector-emitter current will be the same at these 2 BJTs. Therefore, the output current will have a square root relationship with the input. The square root relationship will be between voltage and voltage by adding voltage-current converter at the input and TIA at the output.

Square block. Our analytical transduction model of the square block is eq (6.15), and the block's circuit, numerical simulation, and verification are shown in **Figure 6.9**.

$$V_{out} = G_{sq}\left(V_{in}\right)^2. \tag{6.15}$$

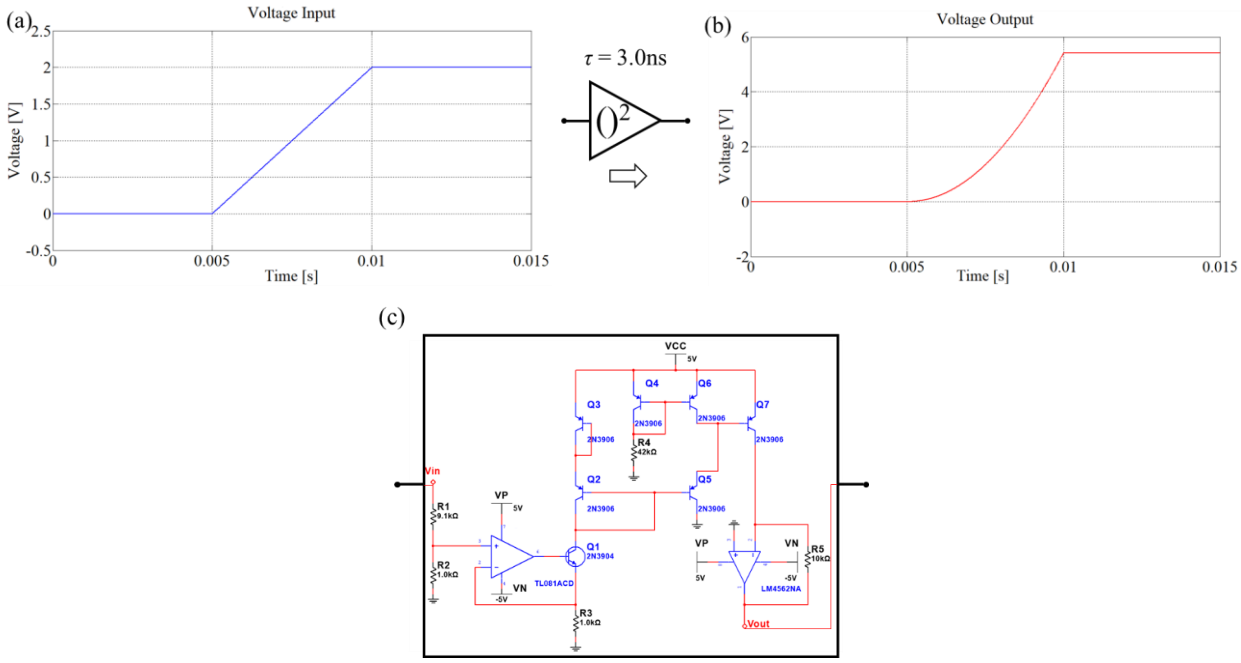

Figure 6.9: Square component. The purpose of the square component is to simulate the square relationship between the input voltage and output force of the comb drive. A test input signal is shown as in (a), and its simulated output is shown as in (b). The component contributes a latency of 3.0ns between its input and output signal. The circuit model of the equivalent circuit is shown in (c). The circuit works by using the translinear principle of BJT which works under weak inversion. By building a loop with four BJTs inside, at the common collector point, using Kirchhoff's law, the collector-emitter current of these BJTs can be expressed as: $I_1 \times I_{bias} = I_2 \times I_3$, where I_{bias} is provided by a current source. Connecting two BJTs with emitter to collector, the collector-emitter current will be the same at these 2 BJTs. Therefore, the output current will have a square relationship with the input. The square relationship between voltage and voltage will be between voltage and voltage by adding a voltage-current converter at the input and TIA at the output.

6.2. System integration verification

Using HSPICE, the circuits shown in **Figures 6.3-6.9** are integrated into a complete system, simulated, and verified with our analytical models. We used static, transient decay rate, resonance, and bandwidth simulation modes to verify the transduced displacement, comb drive force, and artificially-generated damping, stiffness, mass, and nonlinear stiffness. The parameter values used in our verification and test case are given in **Table 6.1**.

Displacement. In **Figure 6.10** we show the result of applying a DC input step voltage, which compares well to the analytical expression $x = F_{dr} / K$ with a relative error of 0.135%.

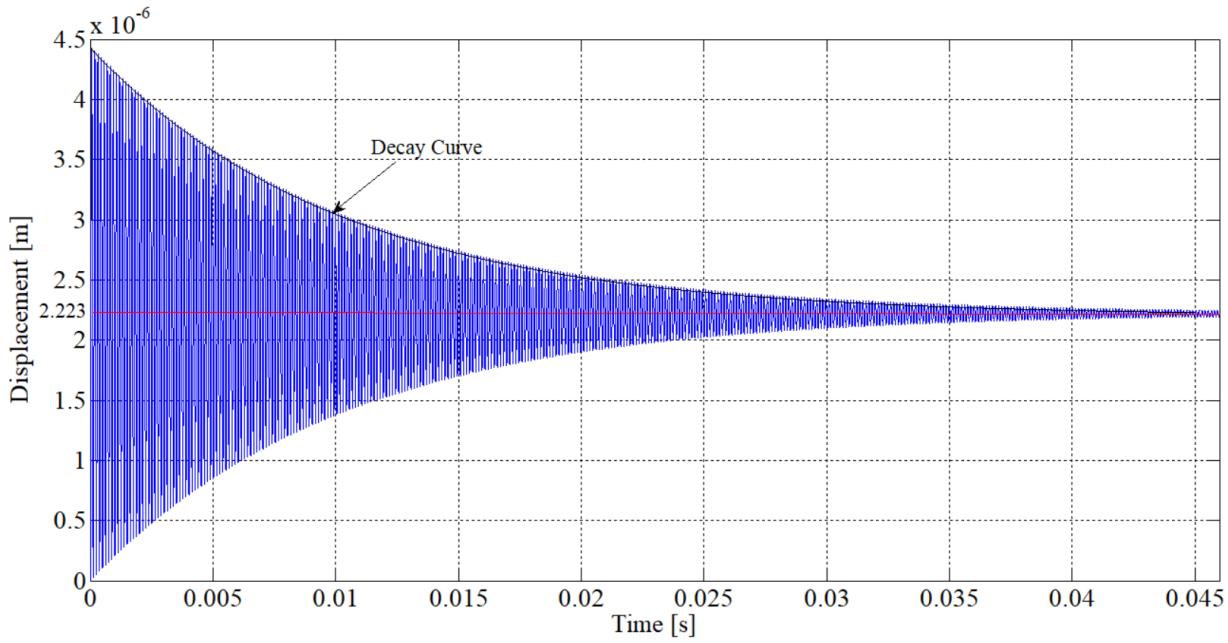

Figure 6.10: Result of TA when a static input force of 4.44uN (Drive voltage of 22.4V) is applied to the MEMS with zero displacement and velocity initial conditions. The simulation results in a static displacement of 2.223um, compared with the calculated ideal static displacement of 2.22um, the relative error is 0.135%.

Damping. By measuring the exponential decay rate of the HSPICE simulation shown in **Figure 6.10**, we find that damping also compares favorably with $\gamma = D / 2M$, with a relative error of 0.07%.

Bandwidth. Instead of using linearized HSPICE's frequency to capture nonlinearity, we obtained a nonlinear frequency response by slowly stepping through increasing drive frequencies and capturing the response amplitude after the steady-state was reached. The natural resonance frequency is predicted by $\omega_d = \sqrt{\omega_0^2 - 2\gamma^2}$, where ω_0 is the undamped displacement frequency, or damped velocity resonance frequency, which is $\sqrt{K/M}$. The bandwidth of a linear analytical model is $BW = \omega_d / Q = 2\omega_d \zeta$, where ζ is the fraction of critical damping, $\zeta = D/2\sqrt{KM}$. Our analytical expression [8] for the linear frequency response subject to feedback latency is given as

$$x_0(\omega) = \frac{F_{dr,0}}{\sqrt{\begin{pmatrix} K + K_e \cos(\omega\tau_K) \\ -\left(\begin{matrix} M + M_e \cos(\omega\tau_M) \\ - D_e \omega^{-1} \sin(\omega\tau_D) \end{matrix}\right)\omega^2 \end{pmatrix}^2 + \left(\begin{matrix} D + D_e \cos(\omega\tau_D) \\ - K_e \omega^{-1} \sin(\omega\tau_K) + M_e \omega \sin(\omega\tau_M) \end{matrix}\right)^2 \omega^2}} = \frac{F_{dr,0}}{\sqrt{\left(K_{eff} - M_{eff}\omega^2\right)^2 + D_{eff}^2 \omega^2}}. \quad (6.16)$$

We plot eq (6.16) in **Figure 6.11** as the red curve. Due to the length of time for each data point of our HSPICE circuit simulation to reach steady-state, we have only focused on the points near the peak of the curve and near the bandwidth about the 3dB down location. Our numerical results are shown in **Figure 6.11** as the blue piecewise curves. We find that the resonance frequency is off by 0.2 Hz the bandwidth is off by 0.05 Hz. Verification yields a relative error of 0.6% for resonance amplitude and a relative error of 7.1% for bandwidth. We suspect that the larger error in bandwidth is due to the damping nonidealities in HSPICE circuit models and our leakage current.

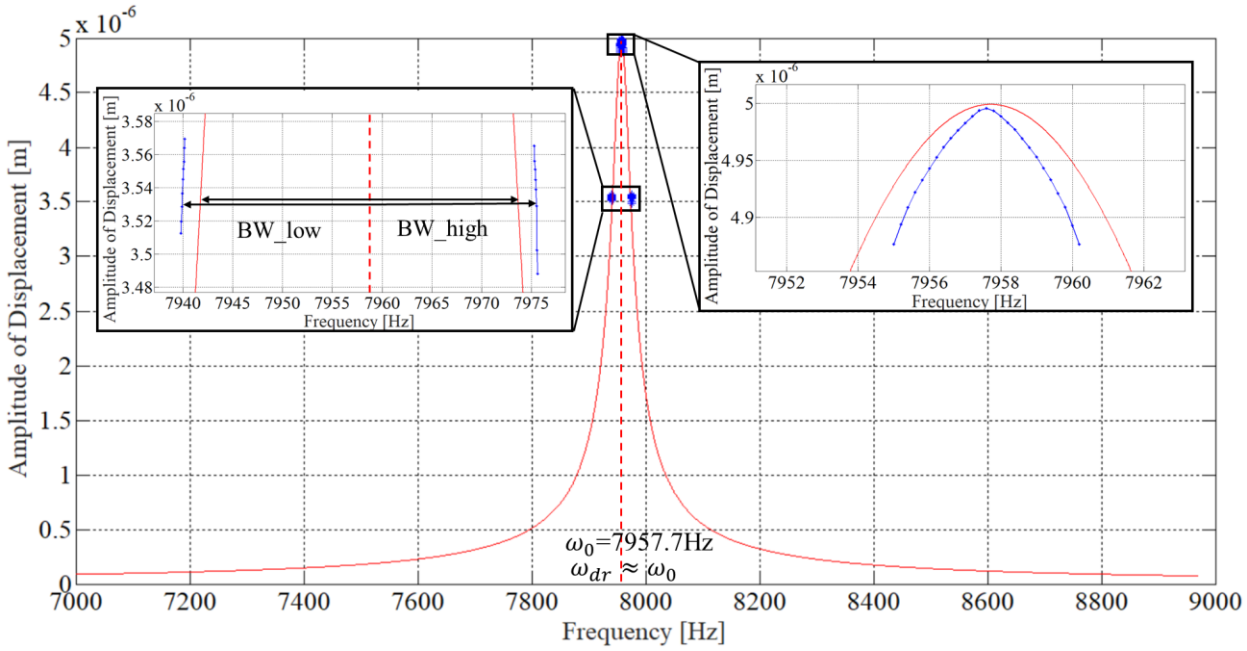

Figure 6.11: Verification of TA characteristics by comparing TA's resonance frequency and bandwidth with AC analysis. The resonance is 7.9577kHz, bandwidth is 31Hz.

6.3. Nonlinear stiffness Results

Using our verification between expected analytical modeling behavior and our numerical modeling testbed, we now investigate how temperature changes affect our PODMEMS test case which is subject to artificial vacuuming and artificial stiffening. Thermal expansion of length, width, and thickness of flexure, as well as the effect of temperature on Young's modulus, is modeled as

$$K(T) = \frac{E(T)h(T)}{4}\left(\frac{w(T)}{L(T)/2}\right)^3 \tag{6.17}$$

where

$L(T) = L_0(1+\alpha\Delta T)$, $w(T) = w_0(1+\alpha\Delta T)$, $h(T) = h_0(1+\alpha\Delta T)$, and

$$E(T) = 145\times10^9 \exp\left(2.61\times\frac{10^{-3}eV}{k_B T}\right)[Pa]$$

and where the coefficient of thermal expansion of silicon is $\alpha = 2.6\times10^{-6}\,\mathrm{K}^{-1}$, the reference geometry at 300K is L_0, w_0, h_0, electron volts is $eV = 1.6\times10^{-19}\,\mathrm{J}$, and Boltzmann constant is $k_B = 1.38\times10^{-23}\,\mathrm{J/K}$.

To verify the benefit of adding nonlinear stiffness on the high-*Q* device, an artificially tuned *Q* is increased to > 10^5, which only requires a small drive force of 4.43e-11 N to reach a steady-state amplitude of 5mm. In the test case, the damping feedback force is driven by $F_{D_e} = D_e\dot{x} = \left(N\varepsilon_0 h/g\right)V_D^2$=3.87e-8N , which requires a voltage amplitude of 2.1V, the nonlinear term is driven by $F_\kappa = \kappa_e x_\tau^{\,3} = \left(N\varepsilon_0 h/g\right)V_\kappa^2$=1.25e-7N , which requires a voltage amplitude of 3.8V. For a comparison with mechanical forces, the force amplitude of stiffness is $Kx_{\max} = 1\text{e-}5N$, damping is $D\dot{x}_{\max} = 3.875\text{e-}8\mathrm{N}$, and mass $M\ddot{x}_{\max} = 1\text{e-}5N$. By changing the mechanical stiffness *K* according to temperature variation (6.17), which is represented by the capacitor in HSPICE, the relationship between the temperature variation and resonance frequency change in both linear and nonlinear models is shown in **Figure 6.12**.

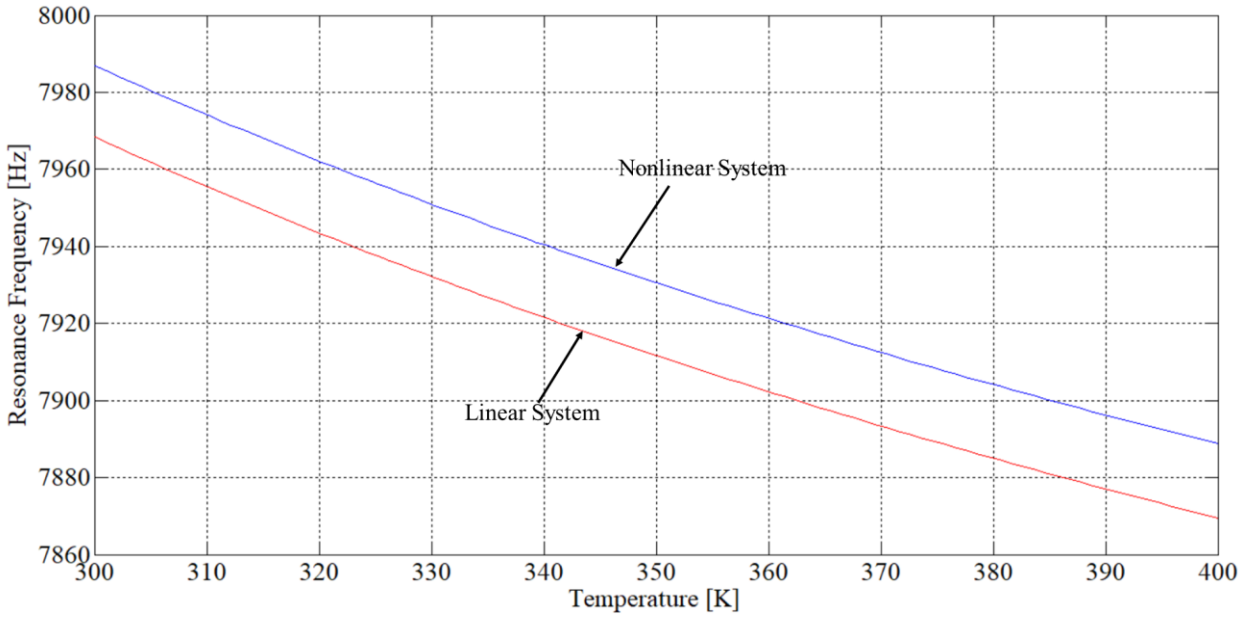

Figure 6.12: Resonance frequency shift due to temperature change. The red curve is the linear model and the blue curve is the nonlinear model.

As seen in **Figure 6.12**, increasing the temperature by 10K decreases the resonance frequency by about 10Hz for both linear and nonlinear models. However, as shown in **Figure 6.13**, the amplitude of the linear model experiences a large decrease of 99.2%, while the nonlinear system only experiences a decrease of 30%, which is still within 3dB of nominal. The plot in Figure 15 is a stepped sweep of drive frequency using HSPICE's transient analysis, where each data point was acquired after steady state was reached. Simulations also demonstrated the jump-up and jump-down phenomenon (not shown here), which is a characteristic of Duffing oscillators. The transient simulations were subject to nonidealities such as noise, parasitic capacitance, and leakage current at three locations on the circuit (recall **Figure 6.7**). The maximum level of noise was 43.4mV.

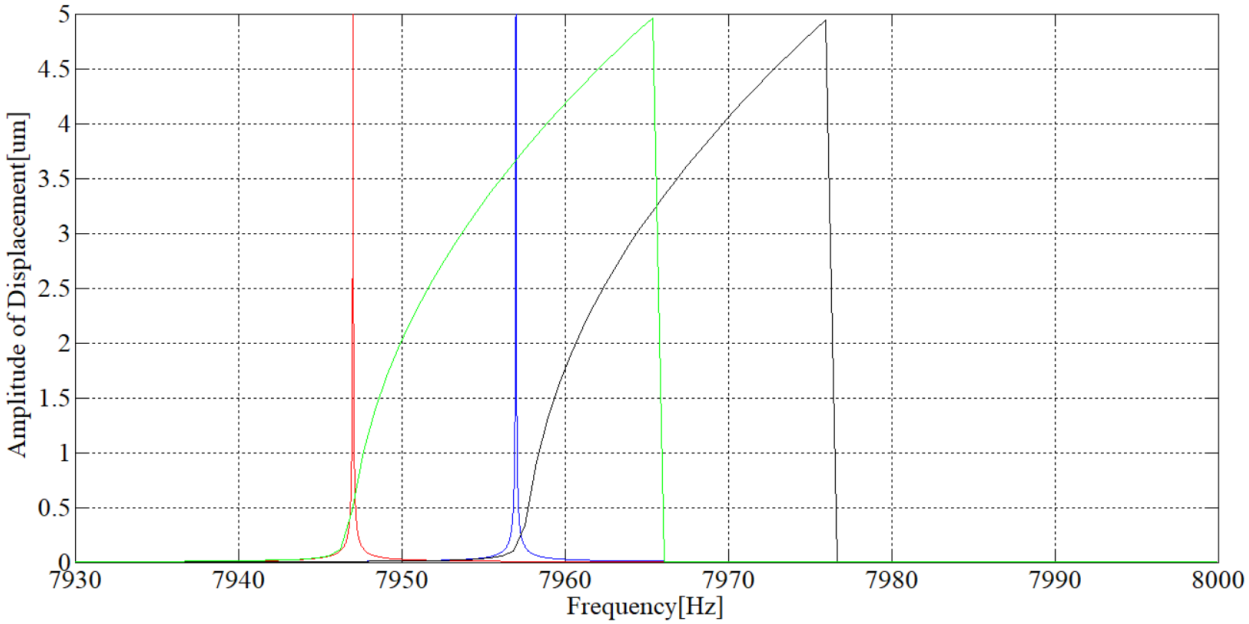

Figure 6.13: Frequency response of linear and nonlinear HSPICE circuit models of PODMEMS undergoing thermal drift. For the constant driving frequency of 7957Hz for the linear model, and detuned to the frequency of 7966Hz for the nonlinear model, an increase in temperature of 10K results in a resonance frequency change of about 10Hz. Such drift causes the linear model's amplitude to drop by 99.8% (56dB) and causes the nonlinear model's amplitude to drop by 30% (3dB).

6.4. Conclusion

In this chapter, we proposed a method to address the stability issue confronted by high-*Q* MEMS resonators that are subject to thermal drift. High-*Q* resonators typically have a very narrow bandwidth, so it can be difficult to match the drive frequency to a driving structural resonance frequency. A small temperature change can cause the oscillator to lose resonance by falling below cutoff frequency amplitudes. However, the amplitude can remain above cutoff by controllably bending the response curve through artificial damping. Moreover, using artificial vacuuming can significantly decrease and maintain the cost of achieving high-Q behavior as the device ages.

Chapter 7

Application to Thermal Drift

We propose a method to reduce the signal attenuation problem that is often associated with drift in vibratory microelectromechanical system (MEMS) gyroscopes. Drift in the electromechanical properties of MEMS can be caused by changes in temperature, pressure, or packaging stress, which can impact the values of the frequencies and the size of resonance amplitudes. Large resonance amplitude in MEMS is used to increase the strength of signals above the level of noise. When resonance amplitude is increased by increasing the quality factor (Q) from thousands to millions, the bandwidth of the resonance frequency reduces by the same factor, and the cost of the device increases by about the same factor. Such narrow vertical bandwidths increase the challenge in matching the frequency of the excitation to the drifting resonance frequencies of the drive mode and that of the sense mode. Due to the extremely narrow bandwidths, mismatch between the three frequencies results in significant signal attenuation within the gyroscopic sensor. This chapter addresses the problem of matching these three frequencies while uncharacteristically reducing the cost. To achieve high Q, we use an artificial electrostatic feedback force that is proportional to the negative velocity of the proof mass to produce a negative damping effect that restores energy lost per vibratory cycle due to natural damping. To achieve a consistently strong sensing signal during drift, we use a second artificial electrostatic feedback force that is proportional to displacement cubed, which bends the narrow vertical peak to cover a larger range of frequencies that are within 3dB of the preferred amplitude. This effectively achieves both high-Q and large bandwidth. Therefore, the problem of matching the three frequencies of the sense mode, drive mode, and the drive modes' excitation

signal is reduced to simply locking the drive modes' excitation frequency to the sense mode's resonance frequency. That is, the drive and sense modes are continuously excited by the same sinusoidal voltage signal, which is itself locked to the drifting resonance frequency of the sense mode. Efforts by others to reduce drift sensitivity include using temperature-dependent drive frequency to match the drift of structural resonance frequency; creating structural designs that are less sensitive to temperature variations; encapsulating the MEMS in a thermal reservoir to maintain a constant temperature, etc. However, by integrating our feedback method into inexpensive MEMS gyroscopes, our study suggests that the level of performance may be improved to that of expensive MEMS gyroscopes. Our simulation results show that the drive mode's excitation frequency can be locked to the sense mode structural resonance frequency with 0.006% error. For instance, by applying a temperature change of 80^{o}C, which is the temperature range of consumer electronics, the signal from our nonlinear feedback system attenuates by 0.4dB instead of an attenuation of 94.8dB without our nonlinear feedback. By applying the feedback velocity voltage, which is proportional to the velocity of the proof mass and has a maximum value of 0.43V, the effective quality factor of the drive mode is increased by a hundred times, from 12k (in air at STP) to 1.2M (in an artificial vacuum). All feedback voltages remained less than 2V.

7.1. Background

MEMS gyroscopes measure changes in orientation. They are presently used in smart phones, virtual reality controllers, automobile navigation, robotics, etc. [106]–[109]. A most critical challenge in improving the accuracy and sensitivity of MEMS gyroscopes is the drift in resonance frequency due to changes in temperature, pressure, or stress [5]-[6]. Drift produces frequency mismatches between the applied excitation frequency of the drive mode, the structural

resonance of the drive mode, and the structural resonance of the sense mode. And large quality factors with a narrow bandwidth are required for the vibratory gyros to amplify the small Coriolis forces that they are trying to sense, which increases the cost of the gyros since the higher the quality factor, the higher the cost (see **Figure 7.1**). Therefore, a small mismatch in frequency can cause the output signal to be greatly reduced to the level of noise.

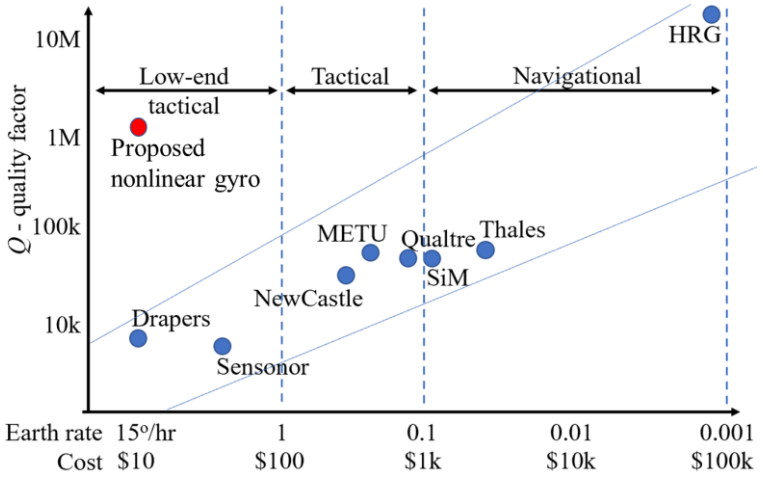

Figure 7.1: Quality factor versus cost for MEMS gyroscopes. As *Q* increases exponentially, so do performance and cost [112]. Simulations show that our nonlinear MEMS vibratory gyroscope can adjust its effective *Q* without modifying its design. That is, by tuning the velocity feedback voltage, the effective *Q* can be tuned from a low to high value without affecting cost.

A review of efforts to address frequency drift in MEMS gyroscopes is discussed in [3] and [7]. Example efforts include the design of temperature-insensitive mechanical structures [114], [115], thermal reservoir packaging [116], and electrostatic tunning [117]–[124]. In [114], Kaji et al. uses the donut-like rigid mass suspended on a single central anchor to improve the system's symmetry. The split of drive mode and sense mode frequency is reduced by a factor of 100 because the drive and sense mode share the same temperature-dependent mechanical elements. In [115], the MEMS gyroscope adopted the symmetric structure to decrease the

temperature sensitivity. The resonance frequency split between drive and sense mode caused by temperature range is reduced by 40 times. Researchers have also investigated oven control methods: on-chip and off-chip architecture. In [116], Lemmerhirt et al. used the on-chip method by integrating all structures in a sealed first-level package, where MEMS die is installed on an isolation platform with surrounding heaters. The heater controls the cavity temperature of the sealed package. A more effective method, called the electrostatic tuning method, was studied for its advantages of not requiring a new structure design, being low cost, and being adaptable to various types of MEMS devices. The electrostatic tunning method utilizes a structure-specific electrostatic negative stiffness effect to change the structure's stiffness by adjusting the feedback voltage, thereby altering the resonant frequency to compensate for frequency drift [117]. Complex algorithms are used for parameter fitting [118], [119], identification [120], [121], and prediction [122] to realize real-time frequency tunning. Although these methods can eliminate the frequency split, they require large data acquisition. The phase domain approach is also adopted to reduce frequency mismatch on drive mode [123]. When frequency mismatch between the drive signal and drive mode structural displacement signal is 0, the phase difference between drive signal and drive mode structural displacement signal is 90^0, which can be measured through a phase-locked loop (PLL). Thereby, the frequency match-mode of drive mode can be recognized. In [124], Cheng et al. excited the sense mode to obtain the corresponding DC tuning voltage, which can be used to tune the apparent stiffness of sense mode for mode matching. Compared to mode mismatching conditions, their results show that the bias stability and angular random walk (ARW) are improved by 3.25 and 4.49 times respectively. However, such control did not take into account the frequency mismatch in drive mode caused by drive mode structural resonance frequency drift.

In addition to drifts in temperature, pressure, or packaging stress, process variations also make it difficult to match the vibratory MEMS gyroscope's drive, sense, and excitation frequencies. Some mode-matching efforts by others to improve performance include mechanical geometric post-processing, creating unusual structural designs that are difficult to fabricate, and in-run mode matching. Mechanical post-processing methods include removing material with laser [125] or chemical etching [54] and adding material with mass deposition [44] to match the resonance frequency between different working modes. Post-processing addresses the problem of process variations, it must be done before packaging, it slows production throughput, and does not enable real-time control. Developing unique structural designs can achieve inherent mode matching. Through optimizing spoke location and ring width, the frequency split of a disk-resonating gyroscope is reduced by a factor of 100 in [126]. In [127], Ginger et al. placed the critical element in the center to increase symmetry, which decreased the frequency split by ten times. Although such unusual designs can reduce the modes mismatch, these techniques are passive approaches to minimize frequency split and may face the make-or-break characteristic. Most in-run mode matching methods utilize electrostatic tuning through specially designed electrodes to minimize frequency split in real-time [128]–[130]. In [131], Sung et al. employed the phase relation between signals in the two modes to realize mode matching, which increased the sensitivity of the MEMS gyroscope by 40 times. By injecting a perturbation signal to the quadrature cancellation loop, Yesil et al. improved the bias instabilities and ARW by factors of 1.5 and 6 in [132]. However, such an in-run mode-matching method is unsuitable for extremely high Q MEMS gyroscopes with Q larger than 1M because matching the frequency of the two modes with an extremely small bandwidth requires high-precision circuitry [111].

On the other hand, the hemispherical resonator gyroscope (HRG) has an ultra-high-quality factor, which can be larger than 10M. Matching the frequency of the two modes with such high Q is more difficult. The methods to decrease the frequency split between the two modes include enhancing the mechanical fabrication process [133], using a thermal reservoir package [134], and electronic calibration [135]. In [133], Sharma et al. use the Hauser make H35 jig grinding machining to increase the precision of fabrication, which decreased the frequency split between the two modes by 15 times with the obtained Q of 7M. In [134], Zhao et al. improved the bias error level of the uncompensated HRG by 40 times by using a thermal reservoir package with a Q of 7M. In [135], Zhao et al. use force to rebalance control to improve the HRG's bias stability by three times.

The WGM optical gyroscope can achieve even higher quality factor due to the very low loss and low scattering of the host materials in the visible and near-infrared wavelengths [136]. Because the frequency shift of clockwise mode WGM resonator and counter-clockwise mode WGM resonator is proportional to the angular rate of the system, such a phenomenon is used for building an optical gyroscope. In [136], Liang et al. proposed and experimentally verified the prototype of a WGM gyroscope, whose quality factor is 1 billion. However, due to the specific form of WGM resonator (spherical, bottleneck, etc.), it is difficult to integrate the WGM resonator into the other components of the micro-optic gyroscope. More suitable for integration into a single optical circuit WGM resonators (toroidal, disk-shaped, etc.) are usually characterized by a low Q factor [137]. In [138], Amrane et al. used the disk-shaped WGM resonator for a fully integrated optical gyroscope, whose quality factor is only 370k. Besides, creating sub-millimeter resonant optical gyroscopes is impractical due to the quantum effects [139].

7.2. Vibratory MEMS gyroscope test case

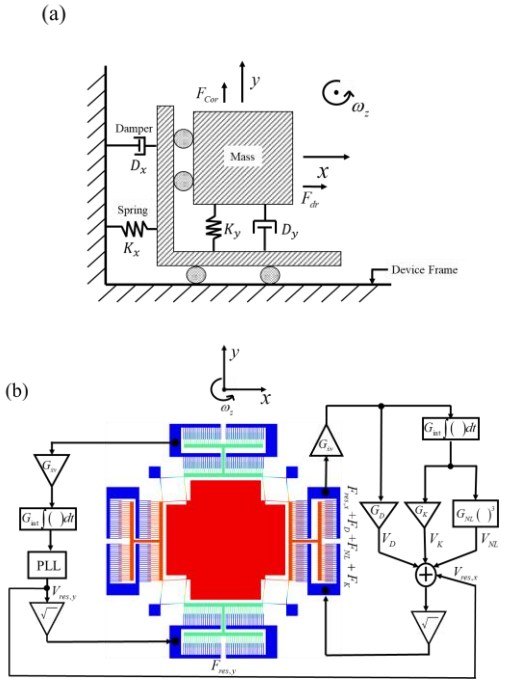

Figure 7.2: Lumped spring-mass-damper model of MEMS gyroscope. For the driving mode, a proof mass is driven to resonate in the *x*-direction with a sinusoidal driving force F_{dr}, which also matches the resonance frequency of the sense mode along the y-axis. The mass is supported in the *x*-direction with spring stiffness K_x and y-direction with spring K_y. The damping in *x* and *y*-directions are D_x and D_y. When the device is rotated about the *z*-axis with angular rate ω_z, then a Coriolis force F_{Cor} generated and exerted on the mass along the *y*-direction. **Figure 7.2(b)** shows the designed MEMS gyroscope with a connected feedback circuit, where the *x*-direction is the drive mode, and the *y*-direction is the sense mode. The blue color comb fingers are stators, while the red color represents moveable structures, which is supported by the flexures. The velocity of the proof mass is converted to voltage and then used for damping feedback. Meanwhile, the sensed velocity will be integrated into displacement, which is then used for linear stiffness feedback. By cubing the voltage signal that is proportional to the displacement, the feedback voltage will be proportional to the cubic of displacement, which is used to generate nonlinear behavior.

As shown in **Figure 7.2**, the MEMS vibratory gyroscope consists of two orthogonal mechanical vibrations: primary mode and secondary mode, which are used to drive the proof mass and sense angular rate. The driving force generated by the input voltage exerted on the spring-mass-damper system causes a vibration on the *x*-axis. The velocity of the proof mass in the *x*-direction is multiplied by the angular rate along the *z*-axis with the mass of proof mass to generate a force, which is then exerted on the spring-mass-damper system on the *y*-axis. Therefore, the z-axis angular rate information can be revealed by sensing the change of displacement on the *y*-axis. The ideal equations representation of the two vibrations is described in eq (7.1) and eq (7.2).

$$M\ddot{x} + D_x\dot{x} + K_x x = F_{dr} = F_o \sin \omega_{dr} t \tag{7.1}$$

$$M\ddot{y} + D_y\dot{y} + K_y y = F_{cor} = -2M\omega_z\dot{x} \tag{7.2}$$

where, $M = 1.45\times10^{-8}\,\text{kg}$ is the proof mass, $D_x = 1.55\times10^{-7}\,\text{Ns/m}$, $D_y = 1.548\times10^{-7}\,\text{Ns/m}$ are the damping of *x* and *y* directions, $K_x = 237.85\,\text{N/m}$, $K_y = 256.62\,\text{N/m}$ are the stiffnesses of *x* and *y* directions, F_{dr} is the magnitude of the driving force, ω_{dr} is the frequency of driving force, ω_z is the angular rate of the *z*-axis, t is time. Solving for drive mode equation eq (7.1), we get the amplitude and phase of displacement as follows:

$$x = \frac{F_{dr}/M}{\sqrt{(\omega_x^2 - \omega_{dr}^2)^2 + \frac{\omega_x^2\omega_{dr}^2}{Q_x^2}}} \sin(\omega_{dr} t + \phi_x) \tag{7.3}$$

$$\phi_x = -\arctan\frac{\omega_x\omega_{dr}}{(\omega_x^2 - \omega_{dr}^2)Q_x} \tag{7.4}$$

where $\omega_x = \sqrt{K_x / M} = 128.08\text{k}\,\text{rad}/\text{s}$ is the structural resonance frequency of drive mode, $Q_x = M\omega_x / D_x$ is the quality factor of drive mode. The bandwidth of drive mode is represented as:

$$BW = \omega_x / Q_x \tag{7.5}$$

To increase structural displacement amplitude, get a better signal to noise ratio (SNR), be more sensitive to Coriolis force, high Q of both drive mode and sense mode is desired in MEMS gyroscope. Nevertheless, matching drive frequency to structural resonance frequency or matching the frequency of drive mode to sense mode with high Q can be difficult due to frequency drift caused by temperature variations.

7.3. Nonlinear feedback and frequency match control system

7.3.1. Electrostatic Force Feedback Circuit

The electrostatic force feedback circuit is used to generate nonlinear stiffness and low damping behavior of drive mode by feeding back the states of the proof mass, and to excite the sense mode by tracking the drifting resonance frequency with PLL. The nonlinear stiffness feedback enables the drive mode to behave like a Duffing oscillator, while the damping feedback can produce high Q by only using the feedback circuit. The excitation of sense mode at resonance frequency with PLL enables the tracking of drifting resonance frequency of sense mode. In the following of this section, the system-level block diagram of the entire electrostatic force feedback system is given. Then generating of nonlinear stiffness behavior and low damping behavior are described in **7.3.2** and **7.3.3,** respectively. The excitation of sense mode is demonstrated in **7.3.4**. Lastly, the determination of the angular rate is described in **7.3.5**.

A system-level block diagram of the entire electrostatic force feedback system is shown in **Figure 7.3**. Gains are labeled *G*, the signal delay time (latency) is *t*, the voltage signals are *V*, and the electrostatic feedback forces are labeled *F*. The voltage signal $V_{dr,x}$ that excites the drive mode is locked to the sense mode's drifting resonance frequency ω_y by the PLL, with the amplification of the PLL's output by $G_{dr,x}$. The output voltage of the drive mode is proportional to the velocity with velocity to voltage gain $G_{\dot{x}v}$. The output voltage $V_{out,x}$ is then amplified by $G_{damping}$ and appears as the feedback voltage V_D for damping control. Meanwhile, the output voltage $V_{out,x}$ is also integrated with gain G_{int}, which results in a voltage V_{int} that is proportional to the displacement. The voltage V_{int} is then amplified by $G_{stiffness}$ and appears as the feedback voltage $V_{stiffness}$ for linear stiffness control. At the same time, the voltage V_{int} is cubed with gain G_{cubed} and appears as the feedback voltage V_{cubed}, which is proportional to the cubic of displacement. The voltages V_D, V_K, V_{NL} and $V_{res,x}$ are then added together and square rooted, which are then converted to force through the square function representing the comb drive. The capacitance of the comb drive is labeled as G_{comb}. In the sense mode, the voltage signal $V_{res,y}$ that excites the sense mode is also locked to the sense mode's drifting resonance frequency, which is square-rooted and converted to force $F_{res,y}$. When the chip rotates at ω_z, then a Coriolis force F_{Cor} that is proportional to the velocity of the drive mode is added to the sense mode.

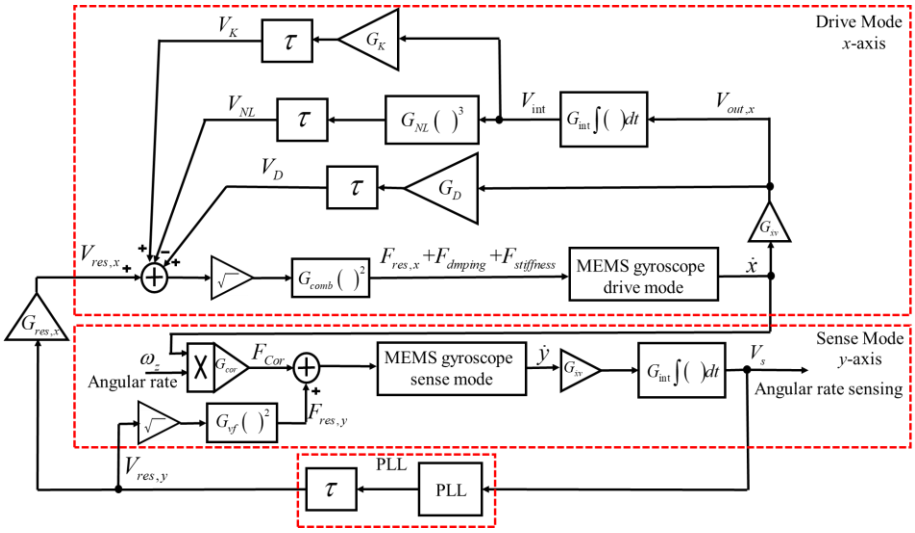

Figure 7.3: System block diagram of MEMS gyroscope with control system for accurate angular rate sensing. The sense mode is excited by two forces: the Coriolis force F_{Cor} that is proportional to the velocity of the drive mode when the chip rotates ω_z, and the force $F_{res,y}$ that is generated by the voltage $V_{res,y}$, whose frequency is locked to the drifting resonance frequency of the sense mode. Meanwhile, the drive mode is driven by four forces: excitation force $F_{res,x}$, which is generated by the voltage $V_{res,x}$, whose frequency is also locked to sense mode resonance frequency; Feedback forces F_D, F_K, and F_{NL}, which are proportional to the velocity, displacement, and cubic of displacement of the proof mass, respectively. The square block and gain G_{comb} are used to represent the voltage-to-force relationship of the comb drive. The square root block cancels out the square relationship generated by the comb drive.

7.3.2 Generating nonlinear stiffness behavior in the drive mode

(a)

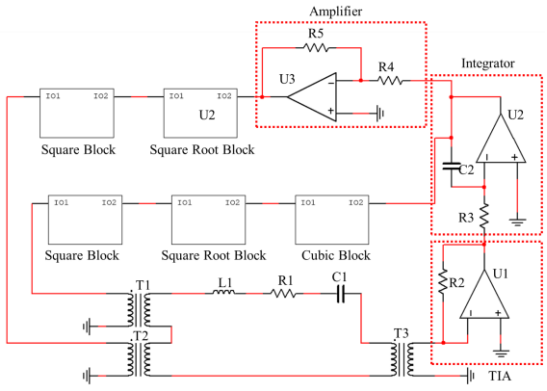
Amplifier
R5
R4
U3
Integrator
U2
C2
R3
R2
U1
Square Block
Square Root Block
Square Block
Square Root Block
Cubic Block
T1
L1
R1
C1
T2
T3
TIA

(b)

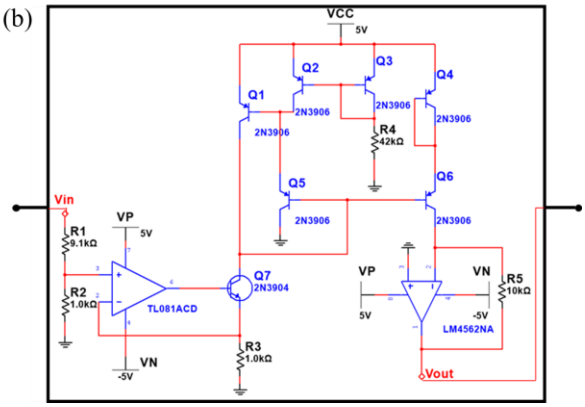
VCC
5V
Q1
Q2
Q3
Q4
Q5
Q6
Q7
2N3906
2N3904
R4
42kΩ
Vin
VP
5V
R1
9.1kΩ
R2
1.0kΩ
TL081ACD
VN
-5V
R3
1.0kΩ
LM4562NA
R5
10kΩ
Vout

(c)

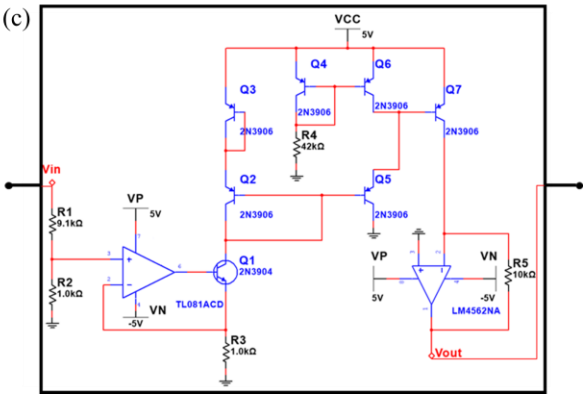
VCC
5V
Q1
Q2
Q3
Q4
Q5
Q6
Q7
2N3906
2N3904
R4
42kΩ
Vin
VP
5V
R1
9.1kΩ
R2
1.0kΩ
TL081ACD
VN
-5V
R3
1.0kΩ
LM4562NA
R5
10kΩ
Vout

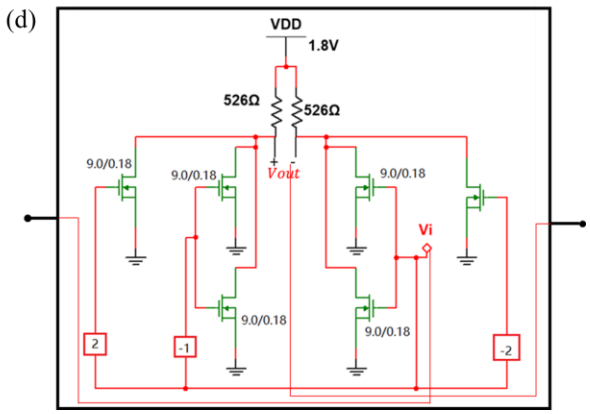

Figure 7.4: Nonlinear stiffness feedback circuit. The drive mode is represented by the RLC equivalent circuit in **Figure 7.4(a)**, where R1 represents the damping D_x, L1 represents the mass M, and 1/C1 represent the stiffness K_x. The velocity of the proof mass, which is represented by the current go through the R1, is converted to voltage by the TIA, which is then integrated to voltage. The integrated voltage is proportional to the displacement, which is amplified and appears as the feedback voltage for linear stiffness feedback. Meanwhile, the integrated voltage is also cubed for nonlinear stiffness feedback. Both the linear and nonlinear stiffness feedback voltages are square rooted and then go through the square block, which represents the comb drive. **Figure 7.4(b)** shows the detail of the square root circuit, which works by using the translinear principle of BJT which works under weak inversion. **Figure 7.4(c)** shows the detail of the square circuit, which also works by using the translinear principle of BJT, which works under weak inversion. **Figure 7.4(d)** shows the detail of the cubic block. The cubic block circuit works by using the characteristic of CMOS under weak inversion.

Without feedback, the small amplitude deflection of the drive mode behaves linearly. To produce nonlinear stiffness behavior, we feed back an amplified electrostatic force onto the proof mass that is proportional to the cube of displacement. This enables the drive mode to behave as a Duffing oscillator at small displacement amplitudes. The stiffness force of the drive mode is

$$F_{stiffness} = \left(K_x + K_e\right)x + \left(\kappa + \kappa_e\right)x^3, \tag{7.6}$$

where $K_e x$ and $k_e x^3$ are electrostatic feedback forces. Such feedback enables the drive mode to increase or decrease both its linear and nonlinear stiffness characteristics. With respect to **Figure 7.3**, the voltage signals pertaining to stiffness force in the drive mode, we have

$$V_{stiffness} = G_{\dot{x}v} G_{\text{int}} G_K x + G_{\dot{x}v}^3 G_{\text{int}}^3 G_{NL} x^3 . \tag{7.7}$$

7.3.2. Generating low damping behavior in the drive mode

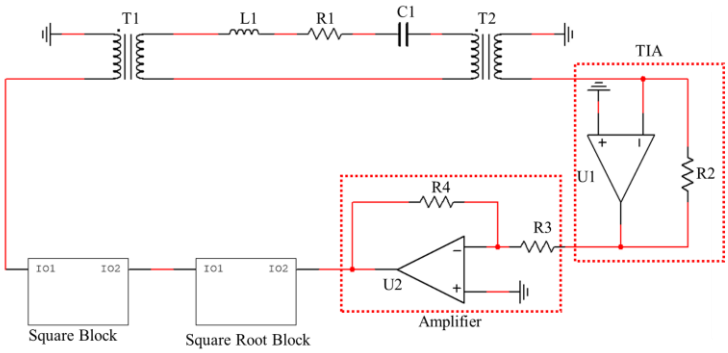

Figure 7.5: Damping feedback circuit. The velocity of drive mode proof mass is converted to voltage by TIA, and then is amplified by the amplifier. The feedback voltage is square-rooted and then goes through the square block, which represents the force generated on the comb drive. Therefore, the generated electrostatic force will be proportional to the velocity. The square root block and square block are as shown in **Figure 7.4(b)** and **(c)**.

High-Q MEMS gyroscopes can be achieved by feeding back an amplified electrostatic force onto the proof mass that is proportional to the negative velocity, such that a negative damping effect that restores energy lost per vibratory cycle due to natural damping is realized. The damping force of the drive mode is

$$F_{damping} = \left(D_x - D_e \right) \dot{x} , \tag{7.8}$$

where $D_e \dot{x}$ is electrostatic feedback force. The damping of the drive mode can therefore be decreased with the feedback. With respect to **Figure 7.3**, the voltage signals pertaining to damping force in the drive mode, we have

$$V_{damping} = G_{\dot{x}V} G_D \dot{x} . \tag{7.9}$$

7.3.3. Excitation of the drifting sense mode

To track the drifting structural resonance frequency of the sense mode, the sense mode must be continuously excited into resonance. The resonance tracking is accomplished through a PLL. For accurate frequency matching, an excitation voltage generated by the PLL is applied to both modes, i.e., the linear sense mode and nonlinear drive modes.

The PLL closed-loop control generates a signal whose output phase is related to the phase of an input signal. As shown in Figure 4, the PLL components include a phase detector (PD), a loop filter (LPF), and a voltage-controlled oscillator (VCO). The PD compares the phase relationship of the input signal $V_s(t)$ and output signal $V_{dr,x}(t)$, LPF is used to filter out the higher frequency in the output of PD through a low pass filter, which can generate a stable phase difference signal $V_c(t)$， and the VCO frequency is controlled by the voltage input.

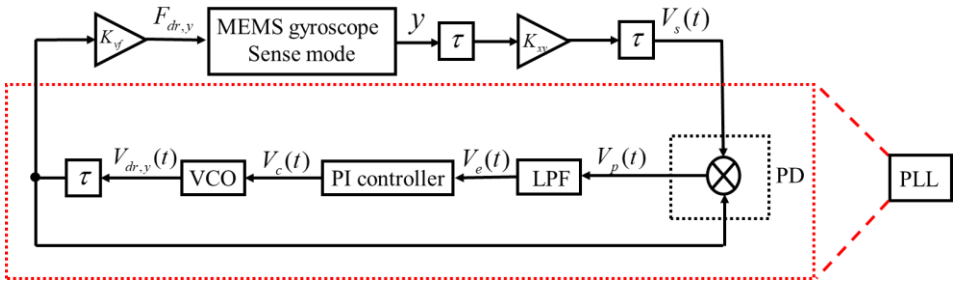

Figure 7.6: PLL module of **Figure 7.3**. The PLL consists of 4 parts: PD, which is a phase detector, is used to detect the phase difference between the two input signals $V_s(t)$ and $V_{res,y}(t)$; LPF, which is a low pass filter, is used to filter out the higher frequency terms in the output signal $V_p(t)$ of PD and generate a signal $V_e(t)$ that is proportional to the phase difference detected by PD; PI controller is used to adjusting the PLL's responding speed

and frequency locking accuracy; VCO, which is voltage controlled oscillator, is used to generate output signal whose frequency is controlled by the phase difference between $V_s(t)$ and $V_{dr,y}(t)$.

When the excitation frequency $\omega_{dr,y}$ is exactly equal to the sense mode structural resonant frequency ω_y, the phase of sense mode displacement is equal to -90°. Such a relationship between excitation frequency and displacement phase can be used to determine whether the excitation frequency follows structural resonant frequency by using PLL. The phase difference between the drive signal and structural displacement can be detected through quadrature demodulation. If the input signal of PLL is $V_s(t) = \cos(\omega_d t + \theta_d)$, the output signal of PLL is $V_{dr,y}(t) = \sin \omega_d t$, where θ_d is the phase of sensed displacement signal, which is also the phase deviation to the structural resonance frequency. Multiply $V_s(t)$ and $V_{dr,y}(t)$ can get the demodulated signal $V_p(t)$, which is shown as in eq (7.10).

$$V_p(t) = V_s(t)V_{dr,y}(t) = \cos(\omega_d t + \theta_d)\sin \omega_d t = \frac{1}{2}(\sin(2\omega_d t + \theta_d) - \sin \theta_d t). \tag{7.10}$$

Demodulated signal eq (7.10) includes a higher frequency AC term and a DC term containing phase information. By using a low pass filter, the higher frequency AC term can be filtered out, leaving only the DC term. When $\theta_d \ll 1$, $\sin \theta_d$ can be approximated as $\sin \theta_d \approx \theta_d$, therefore, phase signal can be expressed as:

$$V_e = -\frac{1}{2}\sin \theta_d \approx -\frac{1}{2}\theta_d. \tag{7.11}$$

In order to increase the response speed and decrease the steady-state error of the PLL, a proportional-integrator (PI) controller is used. The output voltage of the PI controller can be described as:

$$V_c(t) = G_p V_e(t) + G_i \int V_e(t)dt \tag{7.12}$$

where G_p and G_i are the coefficients of proportional and integral terms, respectively.

The output signal $V_c(t)$ can then be used as the control signal for VCO, whose output frequency is controlled by the input voltage. The output frequency ω_d' of VCO is determined by its central frequency ω_o, the difference between the drive signal's frequency ω_d and central frequency ω_o, and the multiplication of control voltage V_c and gain of VCO G_o. ω_d' is described as

$$\omega_d' = \omega_o + \omega_d - \omega_o + G_o V_c = \omega_d + G_o V_c. \tag{7.13}$$

To realize the PLL, firstly, a first-order LPF is chosen, whose transfer function is described as follows:

$$L(s) = \frac{\omega_c}{s + \omega_c}, \tag{7.14}$$

where ω_c is the cutoff frequency, s is the Laplace operator.

The transfer function of VCO is described as:

$$V(s) = \frac{G_o}{s}, \tag{7.15}$$

where G_o is the gain of VCO.

Therefore, the closed-loop transfer function of the PLL is derived as:

$$H(s) = \frac{\theta_o(s)}{\theta_i(s)} = \frac{\omega_c G_o}{s^2 + \omega_c s + \omega_c G_o} \tag{7.16}$$

where $\theta_o(s)$ and $\theta_i(s)$ are the output and input phase of PLL, respectively.

The characteristic equation of the transfer function eq (7.16) is

$$s^2 + \omega_c s + \omega_c G_o = 0 \tag{7.17}$$

The two roots of the characteristic equation are solved as

$$s_{1,2} = \frac{-\omega_c \pm \sqrt{\omega_c^2 - 4\omega_c G_o}}{2}. \tag{7.18}$$

Since ω_c is the cutoff frequency of LPF and $\omega_c > 0$, the two roots in eq (7.18) will always have a negative real part, which means all the poles of the closed-loop system are located in the left part of the s-plane. Therefore, the closed-loop system is asymptotically stable.

Assuming the input phase θ_i has a step change at time $t = 0$, which is represented as

$$\theta_i(t) = u(t)\Delta\varphi, \tag{7.19}$$

where $u(t)$ is the unit step function, $\Delta\varphi$ is the change of input phase. The Laplace transform of the phase input change eq (7.19) is

$$\theta_i(s) = \frac{\Delta\varphi}{s}. \tag{7.20}$$

By substituting the step input eq (7.20) to the system transfer function eq (7.16), the phase error is

$$\theta_e(s) = \left(1 - H(s)\right)\theta_i(s) = \frac{(\omega_c + s)\Delta\varphi}{(\omega_c + s)s + \omega_c G_o}. \tag{7.21}$$

According to the final value theorem of the Laplace transform, when time *t* tends to infinity,

$$\theta_e(\infty) = \lim_{s \to 0} s\theta_e(s) = 0. \tag{7.22}$$

Therefore, the phase error tends to zero when time tends to infinity. The settling time of the PLL under step response is

$$t_s = \frac{7}{\omega_c}. \tag{7.23}$$

7.3.4. Determining the angular rate

To determine the input angular rate from the output voltage of the sense mode, the nonlinear drive mode, and the sense mode equations and are solved as follows. First, the steady-state maximum displacement amplitude X_{dr} of nonlinear drive mode at a given driving frequency ω_{dr} is solved with the harmonic balance method. The harmonic balance method assumes the displacement trajectory of the drive mode motion equation (7.8) as

$$x = a\cos\left(\omega_{dr}t\right) + b\sin(\omega_{dr}t) = X_{dr}\cos(\omega_{dr}t - \phi) \tag{7.24}$$

where $X_{dr} = a^2 + b^2$, $\tan\phi = \frac{b}{a}$.

Substituting the displacement trajectory equation (7.24) into drive mode motion equation (7.8) leads to

$$\begin{aligned}
&\left(-\omega_{res,x}^2 a + \omega_{res,x}\frac{\left(D_x - D_e\right)}{M}b + \frac{\left(K_x + K_e\right)}{M}a + \frac{3\kappa_e}{4M}a^3 + \frac{3\kappa_e}{4M}ab^2 - \frac{F_{res,x}}{M}\right)\cos\left(\omega_{res,x}t\right) \\
&+\left(-\omega_{res,x}^2 b - \omega_{res,x}\frac{\left(D_x - D_e\right)}{M}a + \frac{3\kappa_e}{4M}b^3 + \frac{\left(K_x + K_e\right)}{M}b + \frac{3\kappa_e}{4M}a^2 b\right)\sin\left(\omega_{res,x}t\right) \\
&+\left(\frac{\kappa_e}{4M}a^3 - \frac{3\kappa_e}{4M}ab^2\right)\cos\left(3\omega_{res,x}t\right) + \left(\frac{3\kappa_e}{4M}a^2 b - \frac{\kappa_e}{4M}b^3\right)\sin\left(3\omega_{res,x}t\right) = 0.
\end{aligned} \tag{7.25}$$

If we neglect superharmonic terms containing $3\omega_{dr}$, the coefficients of $\cos\left(\omega_{dr}t\right)$ and $\sin\left(\omega_{dr}t\right)$ are required to be zero

$$\begin{cases}
-\omega_{res,x}^2 a + \omega_{res,x}\dfrac{\left(D_x - D_e\right)}{M}b + \dfrac{\left(K_x + K_e\right)}{M}a + \dfrac{3\kappa_e}{4M}a^3 + \dfrac{3\kappa_e}{4M}ab^2 - \dfrac{F_{res,x}}{M} = 0 \\
-\omega_{res,x}^2 b - \omega_{res,x}\dfrac{\left(D_x - D_e\right)}{M}a + \dfrac{3\kappa_e}{4M}b^3 + \dfrac{\left(K_x + K_e\right)}{M}b + \dfrac{3\kappa_e}{4M}a^2 b = 0.
\end{cases} \tag{7.26}$$

The parameters a and b in the coefficients equation eq (7.26) can be eliminated by squaring the coefficient equations in eq (7.26) and adding them. The relationship between X_{dr} and ω_{dr} then can be described as

$$\left[\left(\omega_{res,x}^2-\frac{\left(K_x+K_e\right)}{M}-\frac{3\kappa_e}{4M}X_{dr}^2\right)^2+\left(\frac{\left(D_x-D_e\right)}{M}\omega_{res,x}\right)^2\right]X_{dr}^2=\left(\frac{F_{res,x}}{M}\right)^2. \tag{7.27}$$

To determine the Coriolis force, the velocity amplitude of the drive mode is needed, which can be derived by differentiating displacement trajectory eq (7.24):

$$\dot{x}=\frac{dx}{dt}=\frac{d\left[X_{dr}\cos(\omega_{res,x}t-\phi)\right]}{dt}=\omega_{res,x}X_{dr}\cos(\omega_{res,x}t-\phi). \tag{7.28}$$

Therefore, the velocity amplitude of the drive mode is

$$\dot{X}_{dr}=\omega_{res,x}X_{dr}. \tag{7.29}$$

The Coriolis force exerted on sense mode can therefore be expressed as

$$F_{Cor}=2M\omega_z\dot{X}_{dr}=2M\omega_z\omega_{dr,x}X_{dr}. \tag{7.30}$$

Then, by combing Coriolis force together with excitation force, the static displacement of sense mode Y_{static} is

$$Y_{sense}=\frac{F_{Cor}+F_{res,y}}{D_y\sqrt{\left(\omega_y^2-\omega_r^2\right)/2}}, \tag{7.31}$$

where $\omega_r^2=\omega_y^2-2\gamma^2$ is the damped displacement resonance frequency, $\gamma=\sqrt{D_y/2M}$ is the exponential decay rate.

Substituting Coriolis force eq (7.30) into eq (7.31), the relationship between the sense mode displacement amplitude and input angular rate ω_z is described as

$$Y_{sense} = \frac{2M\omega_z \omega_{res,x} X_{dr} + F_{res,y}}{D_y \sqrt{\left(\omega_y^2 - \omega_r^2\right)/2}}. \tag{7.32}$$

To determine angular rate through the output voltage of sense mode with sense mode displacement amplitude eq (7.32), quantities M, $\omega_{res,x}$, ω_y, D_y, K_x, K_e, D_x, D_e, κ_e, $F_{res,x}$, X_{dr}, and $F_{res,y}$ needed to be determined. Here, electro-micro metrology (EMM) [140] can be used to accurately measure the mechanical quantities M, $\omega_{res,x}$, ω_y, D_y, K_x, K_e, D_x, D_e, κ_e, $F_{res,x}$, X_{dr}, and $F_{res,y}$. Then, through using the PLL to lock drive mode driving frequency $\omega_{res,x}$ with sense mode structural resonance frequency ω_y, $\omega_{res,x}$ will be equal to ω_y, which can be read out from the output of PLL.

7.4. Simulation

To verify the feasibility of the nonlinear feedback and mode matching system, we apply our method in SIMULINK and HSPICE for comparison. **Figure 7.7** shows the model constructed in SIMULINK.

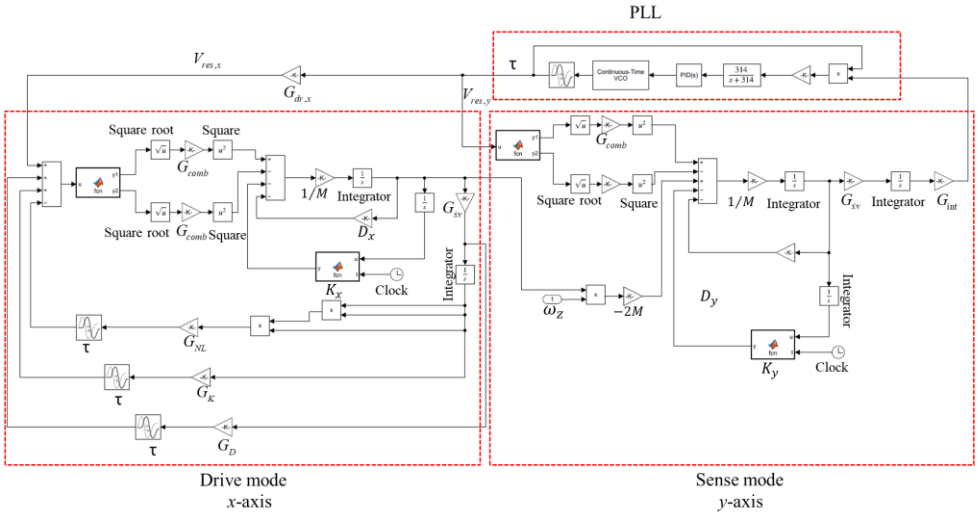

Figure 7.7: SIMULINK realization of the system described in **Figure 7.2**. The drive and sense mode in **Figure 7.2** is implemented with a second-order system by integrating the acceleration to velocity and displacement in this figure. The stiffnesses K_x and K_y are defined in the MATLAB function block, which defines different stiffness values at different times to simulate the effect of temperature change on the change of stiffness value. The square blocks are used to represent the voltage-to-force relationship of the comb drive, while square root blocks are used to square toot the input voltage. Since the square root blocks only take positive values, the MATLAB function block is used to separate the positive and negative values of the voltage signal. The PLL module in **Figure 7.4** is modeled with four blocks in this figure: a multiplier block, is used as PD; a transfer function block, used to define LPF; a PID controller block, specified proportional and integral parameters; a continuous-time VCO block, has the central frequency and input sensitivity defined. The Transport delay block is connected to the PLLs and nonlinear feedback circuit to model the introduced latency τ .

Firstly, the effect of temperature change on the system's stiffness is modeled with thermal expansion of length, width, and thickness of flexure, as well as the effect of temperature on Young's modulus, which is described as:

$$K(T) = 8E(T)h(T)\left(\frac{w(T)}{L(T)}\right)^3 \tag{7.33}$$

where $L(T) = L_0(1+\alpha\Delta T)$, $w(t) = w_0(1+\alpha\Delta T)$, $h(T) = h_0(1+\alpha\Delta T)$ and $E(T) = 145\times10^9 \exp\left(2.61\times\frac{10^{-3}eV}{k_B T}\right)[Pa]$ where the coefficient of thermal expansion of silicon is $\alpha = 2.6\times10^{-6}K^{-1}$, the reference geometry of drive mode flexure at -20ºC is $L_{0,x} = 100\text{um}$, $w_{0,x} = 1.95\text{um}$, $h_{0,x} = 25\text{um}$ .To model the process variations, the reference geometry sizes of sense mode flexure at -20ºC are slightly different with drive mode, which has parameters as $L_{0,y} = 100\text{um}$, $w_{0,y} = 2\text{um}$, $h_{0,y} = 25\text{um}$, electron volts is $eV = 1.6\times10^{-19}\text{J}$, and Boltzmann

constant is $k_B = 1.38\times10^{-23}$ J/K. In the SIMULINK model, a MATLAB function block specifies the stiffness, where the stiffness is a function of temperature as defined in eq (7.33). Meanwhile, through using clock time as another input, the temperature is defined as a step function of time, which can be described as:

$$T = \begin{cases} T_0 & t < t_0 \\ T_0 + \Delta T & t \geq t_0. \end{cases} \tag{7.34}$$

At a temperature of -20°C, the system parameters are set as follows: $\omega_x = 129.28\text{krad/s}$, $M = 1.45\times10^{-8}$ kg, $D_x = 1.55\times10^{-7}\ \text{Ns/m}$, $D_e = 1.5345\times10^{-7}\ \text{Ns/m}$, $D_y = 1.548\times10^{-7}\ \text{Ns/m}$, $K_x = 242.34\,\text{N/m}$, $K_e = 17\,\text{N/m}$, $K_y = 261.46\,\text{N/m}$, $G_{comb} = 1.8\times10^{-7}\ \text{N/V}$, $G_{\dot{x}v} = 10\,\text{Vs/m}$, $G_o = 300\text{Hz/V}$, $G_p = 5$, $G_i = 0.4/\text{s}$, $\omega_c = 340\,\text{rad/s}$.

At a temperature of 60°C, $K_x = 235.53\,\text{N/m}$, $K_y = 254.11\,\text{N/m}$.

To examine the closed-loop characteristic of the PLL, a test is run in the sense mode frequency matching loop. At $t = 0s$, the output frequency of VCO is 10Hz higher than the resonance frequency of structural displacement. At $t = 2s$, temperature is stepped from -20°C to 60°C, which causes the stiffness change from 261.46N/m to 254.11N/m. Therefore, the resonance frequency of the sense mode is changed from 21.372kHz to 21.069kHz at $t = 2\text{s}$. After the simulation run, because of the frequency difference between VCO output frequency and sense mode resonance frequency, PLL will first detect the phase difference through PD and generate a corresponding control V_c voltage for VCO. V_c will decrease dramatically to match VCO output frequency with sense mode resonance frequency. When the simulation reaches $t = 2\text{s}$, because of the resonance frequency change of sense mode, the PLL will adjust the VCO

output frequency to match the sense mode resonance frequency. **Figure 7.8** shows how the PLL's VCO output frequency is locked to sense mode resonance frequency.

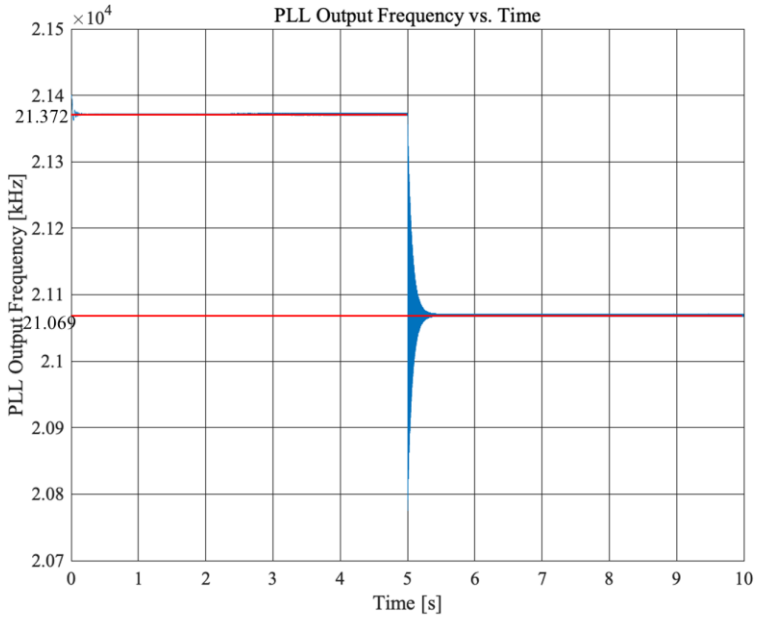

Figure 7.8: Result of VCO output frequency vs. time. The central frequency of VCO is set to be 21.18kHz, which is 10Hz higher than the sense mode's structural resonance frequency, which is 21.372kHz at -20°C. At time t = 2s, the temperature is changed to 60°C, which causes sense mode's structural resonance frequency to be 21.069kHz. The simulation result shows the error of the VCO output frequency to the sense mode structural resonance frequency is $4.72\times10^{-5}\%$.

According to **Figure 7.8**, the response time of the PLL is shorter than 0.2s, and the steady-state frequency mismatch between the PLL output frequency and sense mode structural resonance frequency is $4.72\times10^{-5}\%$.

To examine the characteristic of the nonlinear drive mode, a chirp signal with an amplitude of 0.32V is used to excite the nonlinear drive mode at different temperatures. The chirp signal linearly increases output frequency from 20.24kHz to 20.44kHz within a time range

of 0s to 1000s. When the nonlinear stiffness coefficient $\kappa_e = 1.08\times10^{10}\ \mathrm{N/m^3}$, the corresponding nonlinear stiffness feedback voltage can be obtained from

$$V_{cubed} = \kappa_e X_{dr}^3 / G_{comb} \tag{7.35}$$

where $X_{dr} = 4.4\mathrm{um}$, $G_{comb} = 1.8\times10^{-7}\ \mathrm{N/V}$. The calculated result of nonlinear feedback voltage is 1.28V. The transient response of nonlinear drive mode is shown in **Figure 7.9**, where the red curves show system response at -20°C, and blue curves show system response at 60°C.

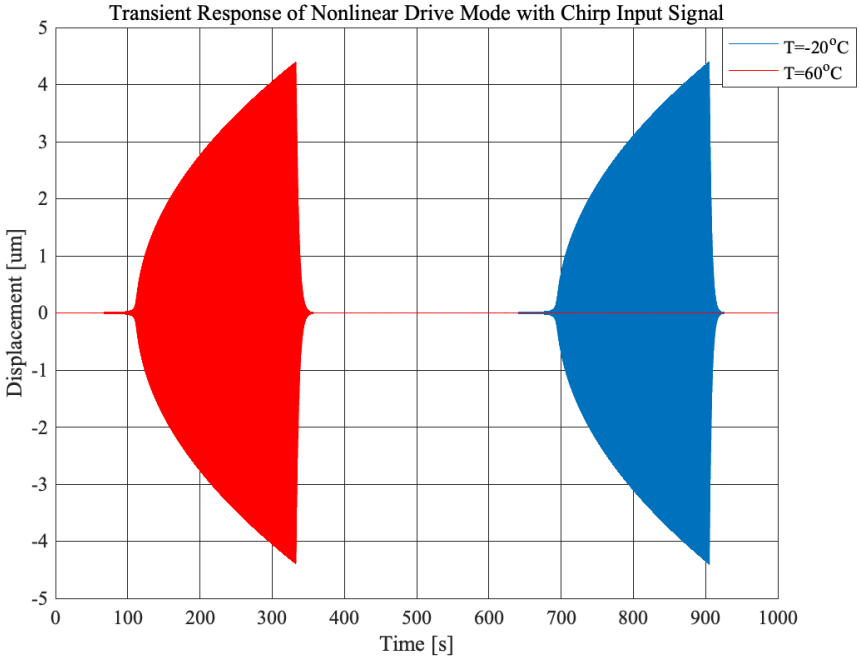

Figure 7.9: Displacement trajectory of nonlinear drive mode vs. time when the nonlinear drive mode is applied with a 0.31V chirp signal, whose frequency linearly increases from 20.24kHz to 20.44kHz within a time range of 1000s. In the figure, the red curve is the temperature at -20°C, and the blue curve is the temperature at 60°C. The linear stiffness K_x of the drive mode was changed from 242.34N/m to 235.53N/m when the temperature changed from -20°C to 60°C. The simulation result shows that the maximum displacement amplitude is 4.4um for both temperatures.

The effect of feedback controls is demonstrated in **Figure 7.10(a)-(d)** by adding the feedback control one by one. Firstly, the frequency responses of drive mode and sense mode without any feedback control is shown as in **Figure 7.10(a)**. When the temperature is increased by 80^{o}C, the amplitude of drive mode is attenuated by -54.8dB. By adding damping feedback control, the quality factor of the drive mode is increased from 12k to 1.2M, with a bandwidth of 0.01Hz. The frequency responses are shown in **Figure 7.10(b)**. When the temperature is increased by 80^{o}C, the amplitude of drive mode is attenuated by -94.8dB. To maintain the amplitude of drive mode a large value for sense mode input, linear stiffness feedback control is added, which is shown in **Figure 7.10(c)**. The resonance frequency of drive mode is increased from 20.575kHz to 21.285kHz. In **figure 7.10(d)**, PLL feedback control is added to lock the excitation frequency of drive mode and sense mode to the drifting resonance frequency of sense mode. Lastly, the nonlinear stiffness feedback control is added, as shown in **Figure 7.10(e)**. Due to the nonlinear frequency response and PLL control, the drive mode is only attenuated by 4.5% (-0.4dB) when the temperature is increased by 80^{o}C.

(a)

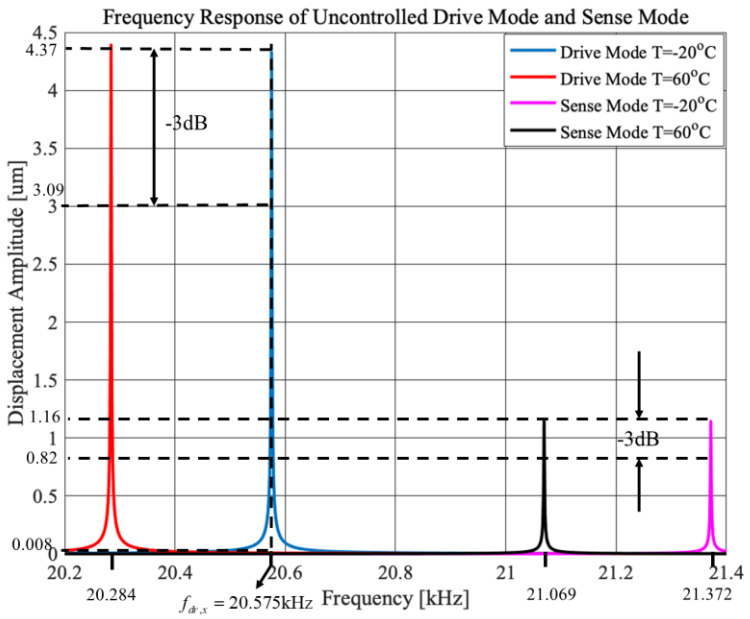
Frequency Response of Uncontrolled Drive Mode and Sense Mode
Drive Mode T=-20°C
Drive Mode T=60°C
Sense Mode T=-20°C
Sense Mode T=60°C
Displacement Amplitude [um]
4.5
4.37
4
3.5
3.09
3
2.5
2
1.5
1.16
1
0.82
0.5
0.008
0
-3dB
-3dB
20.2
20.4
20.6
20.8
21
21.2
21.4
20.284
21.069
21.372
$f_{dr,x}$ = 20.575kHz
Frequency [kHz]

(b)

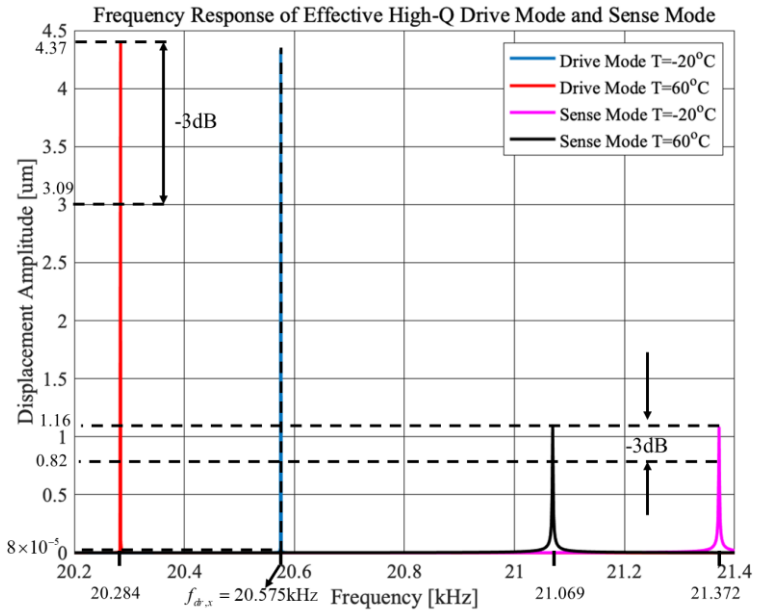
Frequency Response of Effective High-Q Drive Mode and Sense Mode
Drive Mode T=-20°C
Drive Mode T=60°C
Sense Mode T=-20°C
Sense Mode T=60°C
Displacement Amplitude [um]
4.5
4.37
4
3.5
3.09
3
2.5
2
1.5
1.16
1
0.82
0.5
8×10⁻⁵
0
-3dB
-3dB
20.2
20.4
20.6
20.8
21
21.2
21.4
20.284
21.069
21.372
$f_{dr,x}$ = 20.575kHz
Frequency [kHz]

(c)

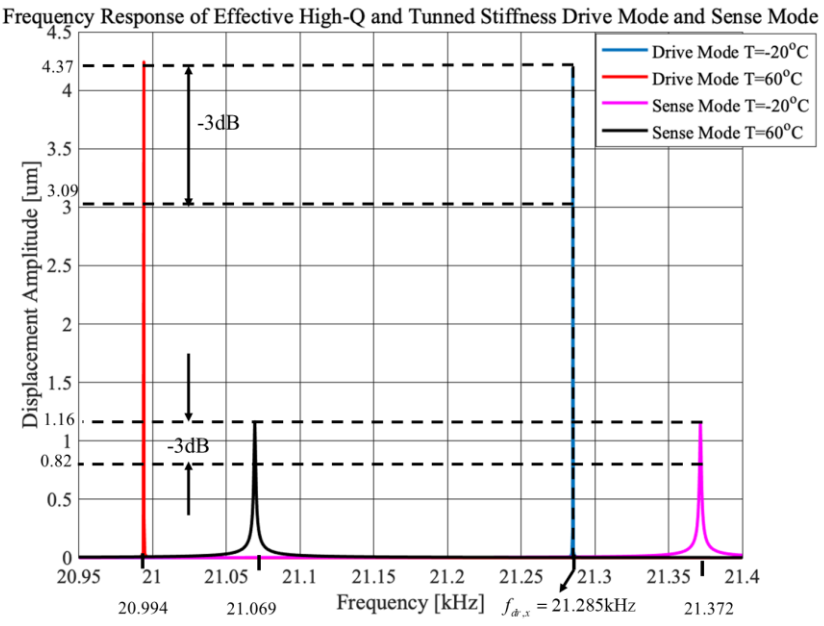
Frequency Response of Effective High-Q and Tunned Stiffness Drive Mode and Sense Mode
Drive Mode T=-20°C
Drive Mode T=60°C
Sense Mode T=-20°C
Sense Mode T=60°C
Displacement Amplitude [um]
4.5
4.37
4
3.5
3.09
3
2.5
2
1.5
1.16
1
0.82
0.5
0
-3dB
-3dB
20.95
21
21.05
21.1
21.15
21.2
21.25
21.3
21.35
21.4
20.994
21.069
Frequency [kHz]
$f_{dr,x}$ = 21.285kHz
21.372

(d)

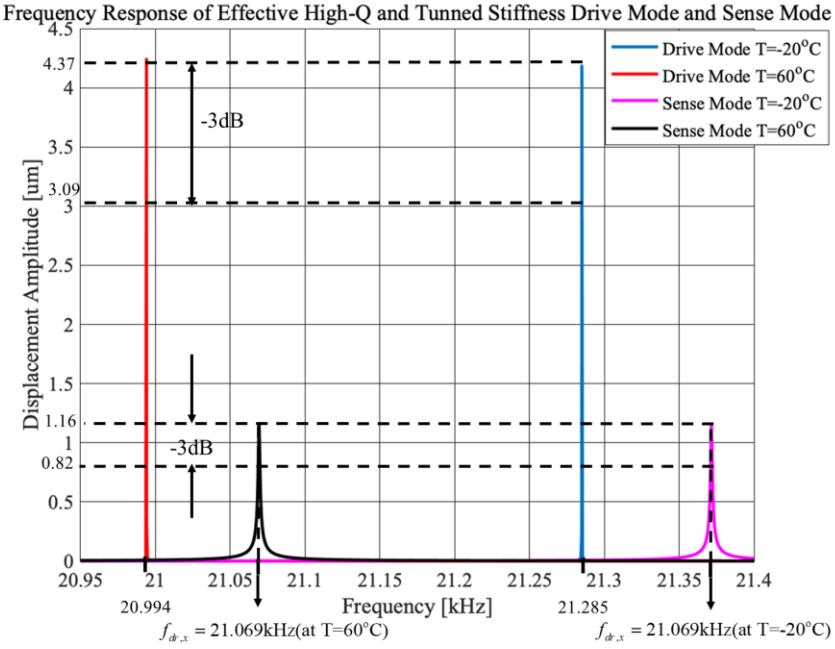
Frequency Response of Effective High-Q and Tunned Stiffness Drive Mode and Sense Mode
Drive Mode T=-20°C
Drive Mode T=60°C
Sense Mode T=-20°C
Sense Mode T=60°C
Displacement Amplitude [um]
4.5
4.37
4
3.5
3.09
3
2.5
2
1.5
1.16
1
0.82
0.5
0
-3dB
-3dB
20.95
21
21.05
21.1
21.15
21.2
21.25
21.3
21.35
21.4
20.994
Frequency [kHz]
21.285
$f_{dr,x}$ = 21.069kHz(at T=60°C)
$f_{dr,x}$ = 21.069kHz(at T=-20°C)

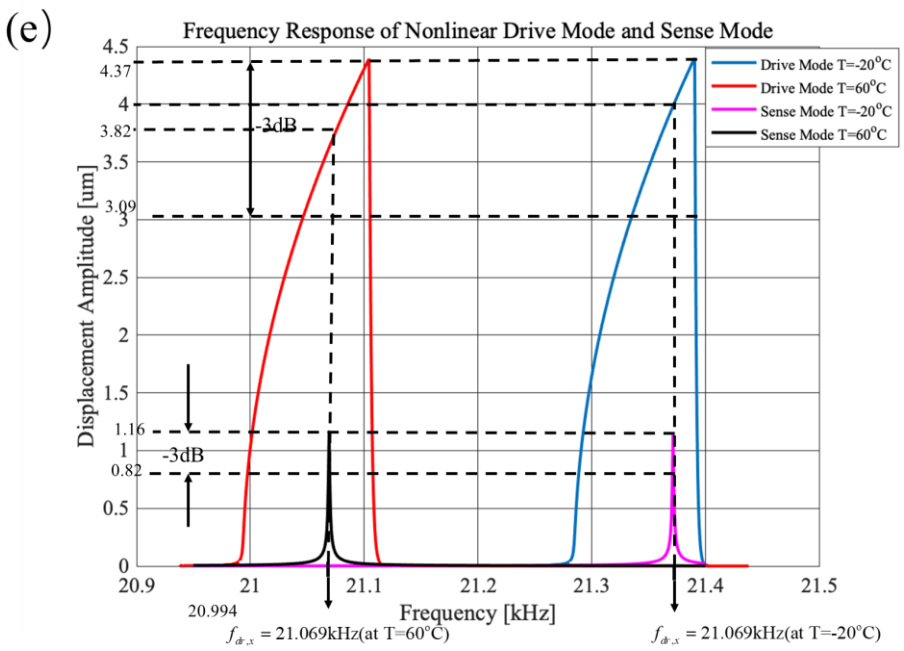

Figure 7.10: Frequency responses of the drive mode and sense mode. In **(a)**, there is no feedback control applied. The bandwidth and quality factor are 1.8Hz and 12k for the drive mode and 1.7Hz and 12.5k for the sense mode. The drive mode is excited at $f_{dr,x} = 20.575\text{kHz}$, when temperature is changed from -20ºC to 60ºC, resonance frequency of drive mode is drifted from 20.575kHz to 20.284kHz, while the resonance frequency of sense mode is drifted from 21.372kHz to 21.069kHz. The amplitude of drive mode is attenuated by 99.8%(-54.8dB). In **(b)**, the damping feedback control is applied, which increases the quality factor of sense mode by 100 times. The amplitude attenuation of drive mode when the temperature is increased by 80ºC is 99.99%(-94.8dB). In **(c)**, linear stiffness feedback control is applied, which tunes the resonance frequency of drive mode from 20.575kHz to 21.285kHz at -20ºC. In **(d)**, the PLL feedback control is applied, which locks the excitation frequency of both drive mode and sense mode to the drifting resonance of the sense mode. Therefore, at T=-20ºC, the drive mode is excited at 21.372kHz, and at T=60 ºC, the drive mode is excited at 21.069kHz. In **(e)**, the nonlinear stiffness feedback control is applied, which enables the drive mode to mimic Duffing oscillator. Due to the nonlinear stiffness feedback control and PLL feedback control, the amplitude attenuation of drive mode is only 4.5%(-0.4dB), which is 22 times smaller than the system in **(b)**.

To show the system's ability to maintain sense mode output voltage amplitude at different angular rate input when the temperature is changed, the input angular rate ranging from $0^{\circ}/\mathrm{s}$ to $100^{\circ}/\mathrm{s}$ is applied to the input of the proposed system. An assumption is made that when the gyroscope starts being excited, the nonlinear drive mode will be swept with excitation voltage frequency ranging from 21.25kHz to 21.45kHz. Under such conditions, the frequency response of the nonlinear drive mode will follow the blue or red curves shown in **Figure 7.10(b)**, where the stability of the nonlinear drive mode will be maintained. The sense mode output voltage amplitude is measured for every corresponding value of the input angular rate. Such measurements are repeated for temperatures of -20ºC and 60ºC. To clearly show that the proposed system can maintain output voltage when the temperature is changed, the absolute percentage change of the output voltage at 60ºC to the output voltage at -20ºC is used. Here, the percentage amplitude attenuation is defined as

$$A = \frac{V_{T1} - V_{T2}}{V_{T1}} \times 100\%, \tag{7.36}$$

where A is the percentage amplitude attenuation between two different temperatures, V_{T1} is the output voltage of sense mode at $T_1 = -20^{\circ}\mathrm{C}$, V_{T2} is the output voltage of sense mode at $T_2 = 60^{\circ}\mathrm{C}$. **Figure 7.11(a)** shows the percentage amplitude attenuation values with different input angular rates of the system corresponding to **Figure 7.10(e)**. The mean value of percentage amplitude attenuation is 4.3% (-0.88dB). As a comparison, such simulation is also run in the system corresponding to **Figure 7.10(b)**, where the excitation frequency of the drive mode is a constant value equal to 20.575kHz. The simulated result is plotted in **Figure 7.11(b)**. The mean value of percentage amplitude attenuation is 87.2% (-41.11dB).

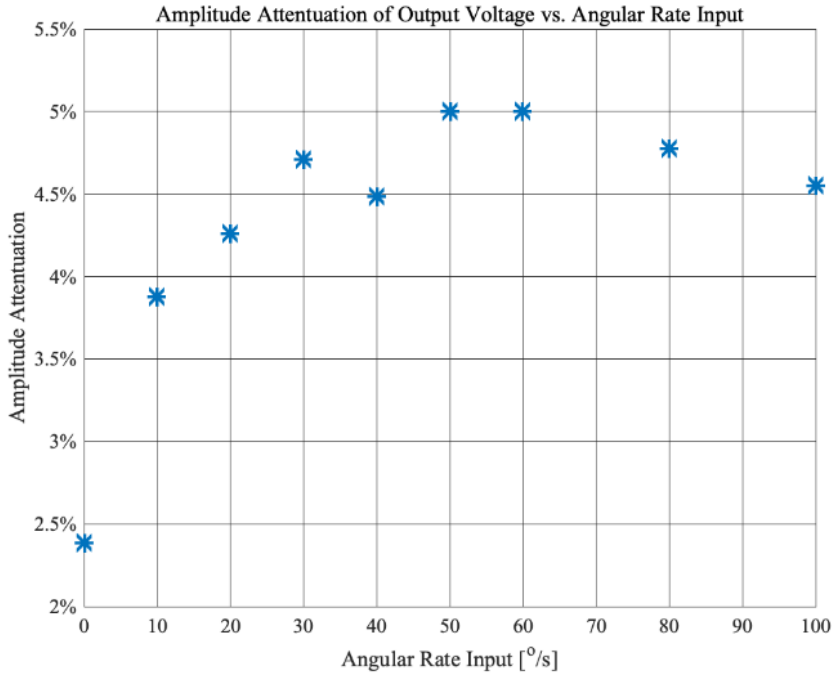

Figure 7.11(a): Percentage output voltage amplitude attenuation vs. angular rate input. For a given input angular rate value, sense mode's output voltage amplitude will be attenuated when the temperature is changed from -20ºC to 60ºC. The dots in this figure show the percentage of amplitude attenuation when the system's temperature is changed. Such simulation is repeated for different angular rate input values ranging from $0\,^{\circ}/\mathrm{s}$ to $100\,^{\circ}/\mathrm{s}$. The result shows that the mean value of amplitude attenuation is 4.3% (-0.88dB).

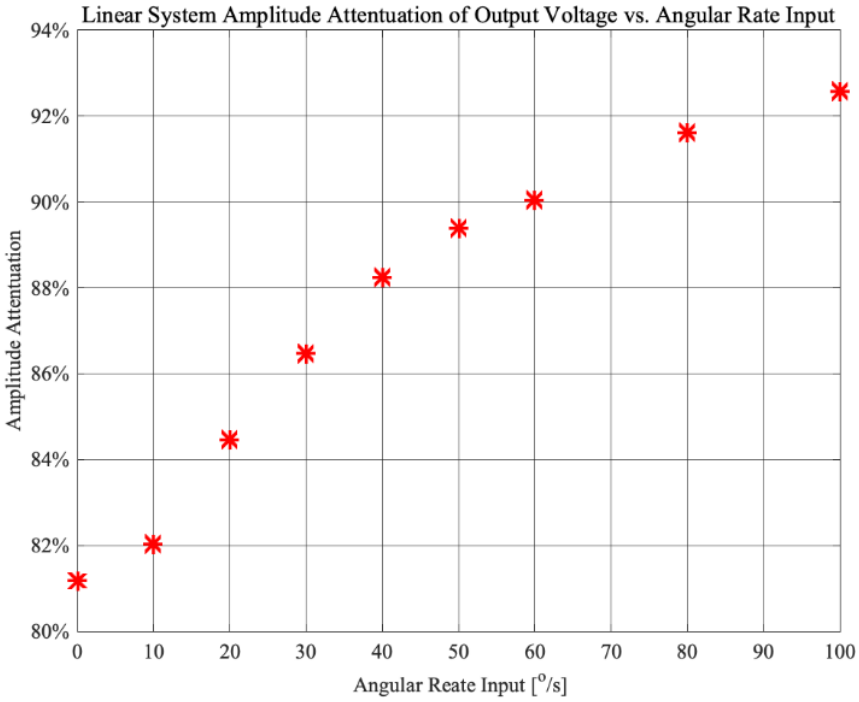

Figure 7.11(b): Percentage output voltage amplitude attenuation vs. angular rate input of a MEMS gyroscope without nonlinear feedback control and mode matching. As a comparison, a MEMS gyroscope with the same mechanical properties as the above-simulated system but without thermal drift control is run with the same simulation as in **Figure 7.11(a)**. The output voltage of sense mode at 60°C is greatly attenuated compared with the output voltage at -20°C. The result shows that the mean value of amplitude attenuation is 87.2% (-41.11dB).

To show the sensitivity of amplitude attenuation to the system's nonlinearity, the system is simulated at a constant angular rate input value of 50°/s, while the nonlinear feedback voltage V_{NL} is varied. The result shown in **Figure 7.12** suggests that amplitude attenuation dropped dramatically within the nonlinear feedback voltage range of 0-1.8V. As the nonlinearity increasea, the amplitude attenuation slowly decreases.

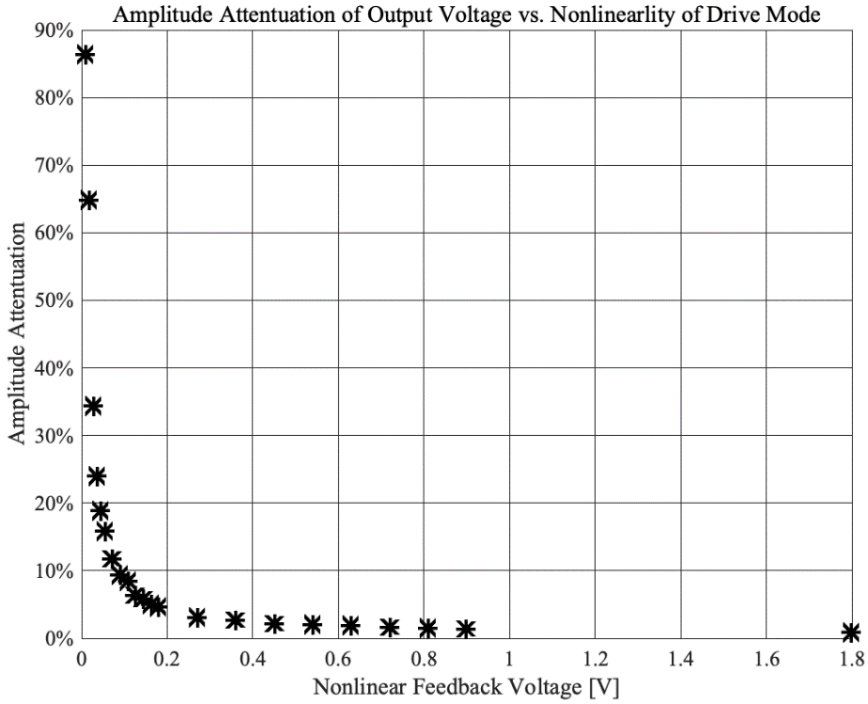

Figure 7.12: Percentage output voltage amplitude attenuation vs. nonlinear stiffness feedback voltage. At a constant angular rate input equal to 50º/s, the amplitude attenuation due to a temperature change of 60ºC is measured with different nonlinear feedback voltages. The system's nonlinearity is increased with the increasing of nonlinear feedback voltage. As shown in the figure, the amplitude attenuation is reduced greatly with the increasing of nonlinear feedback voltage in the range of 0-1.8V, which corresponds to the nonlinear stiffness value of $\kappa_e = 1.08 \times 10^{10}\ \mathrm{N/m^3}$. The amplitude attenuation is slowly reduced when the nonlinear feedback voltage continually increases after 0.2V.

7.5. Conclusion

In this chapter, we proposed a method to reduce the problems associated with frequency drifting and mode matching of vibratory MEMS gyroscopes. For the high-Q MEMS vibratory gyroscopes with Q>1M and structural resonance frequency ranges between a few kilohertz to tens of kilohertz, the bandwidths will be smaller than 0.1Hz. Therefore, the slight shift of

structural resonance frequency due to temperature variation, pressure, and packaging stress can greatly reduce the signal-to-noise ratio or possibly reduce the output signal to the noise level. However, by feeding back electrostatic forces that are proportional to the cubed displacement of the gyroscope's proof mass, the amplitude of drive mode can be maintained within 3dB of a preferred amplitude due to an effective nonlinear frequency response. With a nonlinear frequency response, the drive modes frequency can always be matched to the sense mode's resonance frequency. The gyroscope only needs to lock its sense modes' excitation frequency to its drifting sense mode's structural resonance frequency instead of the more difficult challenge of matching all three frequencies: sense mode structural resonance, drive mode structural resonance, and drive modes' excitation signal. Moreover, the cost of achieving high Q can be significantly decreased through velocity feedback to achieve an effective high Q. Our results show that when the temperature is changed by 80ºC, the displacement amplitude of the drive mode decreases by -0.4dB due to our nonlinear feedback, which is 22 times smaller than the change in amplitude without nonlinear feedback. For an input angular rate ranges from 0 to 100 º/s, the output voltage of sense mode is attenuated when the temperature is changed by 80ºC, with a mean value of an attenuation of 4.3% (-0.88dB). The mean attenuation value is 20.3 times smaller than without the nonlinear feedback and mode-matching. Our results suggest that the amplitude attenuation can be greatly reduced within the 1.8V nonlinear feedback voltage range, corresponding to the nonlinear stiffness coefficient value of $\kappa_e = 1.08 \times 10^{10}\ \mathrm{N/m^3}$. Keeping increasing the nonlinear feedback voltage will slowly reduce the amplitude attenuation.

Chapter 8

Conclusion and Future Work

In conclusion, this dissertation has proposed a comprehensive method to address the performance change of MEMS devices caused by systemic discrepancies arising from process variation and temperature fluctuation. The study has demonstrated the effectiveness of artificially increasing the quality factor (Q) to mitigate these factors impact and reduce the device's cost.

The research has highlighted the significant influence of process variation on the performance of MEMS devices, leading to a mismatch between excitation and resonance frequencies. Additionally, temperature fluctuations have been shown to induce changes in device geometry, material properties, and packaging stress, resulting in drift in the electromechanical properties of MEMS. Previous efforts to reduce drift sensitivity have been explored, such as temperature-dependent drive frequencies, temperature-insensitive structural designs, and thermal encapsulation.

To address the resonance frequency mismatch caused by process variation, this study proposes the generation of an electrostatic force that adjusts the stiffness of the device based on the displacement of the proof mass. Furthermore, to achieve a high Q, an artificial electrostatic feedback force proportional to the proof mass's negative velocity has been employed to produce a negative damping effect, restoring energy lost per vibratory cycle. Additionally, an artificial electrostatic feedback force that is proportional to the displacement cubed has been utilized to ensure a consistently strong sensing signal during drift, expanding the range of frequencies within 3dB of the desired amplitude.

Simulation results have validated the effectiveness of the proposed approach in tuning the effective stiffness, Q, and nonlinearity of the device by adjusting the gain of the feedback circuit. The application of these technologies to a low-cost and temperature-stable MEMS gyroscope has demonstrated a significant reduction in output amplitude attenuation, even in the presence of a temperature variation of 80°C. The output amplitude of the gyro with feedback control exhibited only a 0.4dB attenuation, which is 94.4dB smaller compared to the gyro without feedback control.

In summary, this dissertation has successfully proposed and verified a method to solve the problem of output amplitude instability caused by process variation and thermal drift. The application of electrostatic feedback force to tune the device's effective stiffness, quality factor, and nonlinearity has shown promising results. However, there are several avenues for future research and improvement in this field:

- Further investigation and optimization of the electrostatic feedback force mechanism to enhance its effectiveness in addressing process variation and temperature-induced drift.
- Exploration of alternative feedback control mechanisms or hybrid approaches to further improve the stability and performance of MEMS devices.
- Experimental validation and characterization of the proposed method using real-world MEMS devices and application-specific scenarios.
- Study the impact of other environmental factors, such as humidity and pressure, on the performance of MEMS devices and develop mitigation strategies.
- Development of advanced fabrication techniques and materials to minimize process variation and enhance the stability of MEMS devices.

- Examination of the scalability and manufacturability of the proposed method to ensure its practical implementation in mass production.

By pursuing these avenues of research, it is anticipated that the proposed method will continue to evolve and contribute to the advancement of MEMS technology, enabling the development of more reliable and cost-effective MEMS devices in various applications.

Bibliography

[1] D. Joachim and Liwei Lin, “Selective polysilicon deposition for frequency tuning of MEMS resonators,” in *Technical Digest. MEMS 2002 IEEE International Conference. Fifteenth IEEE International Conference on Micro Electro Mechanical Systems (Cat. No.02CH37266)*, Jan. 2002, pp. 727–730. doi: 10.1109/MEMSYS.2002.984373.

[2] R. Melamud *et al.*, “Composite flexural-mode resonator with controllable turnover temperature,” in *2007 IEEE 20th International Conference on Micro Electro Mechanical Systems (MEMS)*, Jan. 2007, pp. 199–202. doi: 10.1109/MEMSYS.2007.4433054.

[3] J. Cho, T. Nagourney, A. Darvishian, and K. Najafi, “Ultra conformal high aspect-ratio small-gap capacitive electrode formation technology for 3D micro shell resonators,” in *2017 IEEE 30th International Conference on Micro Electro Mechanical Systems (MEMS)*, Jan. 2017, pp. 1169–1172. doi: 10.1109/MEMSYS.2017.7863623.

[4] D. Joachim and L. Lin, “Characterization of selective polysilicon deposition for MEMS resonator tuning,” *J. MICROELECTROMECHANICAL Syst.*, vol. 12, no. 2, pp. 193–200, Apr. 2003, doi: 10.1109/JMEMS.2003.809967.

[5] A. H. Behbahani, D. Kim, P. Stupar, J. DeNatale, and R. T. M’Closkey, “Tailored Etch Profiles for Wafer-Level Frequency Tuning of Axisymmetric Resonators,” *J. Microelectromechanical Syst.*, vol. 26, no. 2, pp. 333–343, Apr. 2017, doi: 10.1109/JMEMS.2017.2667582.

[6] M. A. Abdelmoneum, M. M. Demirci, Yu-Wei Lin, and C. T. . -C. Nguyen, “Location-dependent frequency tuning of vibrating micromechanical resonators via laser trimming,” in *Proceedings of the 2004 IEEE International Frequency Control Symposium and Exposition, 2004.*, Aug. 2004, pp. 272–279. doi: 10.1109/FREQ.2004.1418464.

[7] J. Chang, J. Kim, B.-K. Min, S. J. Lee, and L. Lin, “In-Situ Frequency Tuning of Electrostatically Actuated Vibrating Nano Structures Using Focused Ion Beam,” in *IMECE2006*, Microelectromechanical Systems, Nov. 2006, pp. 139–144. doi: 10.1115/IMECE2006-16080.

[8] C. Chen *et al.*, “A Novel Mechanical Frequency Tuning Method Based on Mass-Stiffness Decoupling for MEMS Gyroscopes,” *Micromachines*, vol. 13, no. 7, 2022, doi: 10.3390/mi13071052.

[9] X. Zhao, B. Zhou, R. Zhang, and Z. Chen, “Research on Laser Trimming of Silicon MEMS Vibratory Gyroscopes,” *Integr. Ferroelectr.*, vol. 129, no. 1, pp. 37–44, Jan. 2011, doi: 10.1080/10584587.2011.576898.

[10] Z. X. Hu, B. J. Gallacher, J. S. Burdess, S. R. Bowles, and H. T. D. Grigg, “A systematic approach for precision electrostatic mode tuning of a MEMS gyroscope,” *J. Micromechanics Microengineering*, vol. 24, no. 12, p. 125003, Oct. 2014, doi: 10.1088/0960-1317/24/12/125003.

[11] R. Jackson and R. Ramadoss, “A MEMS-based electrostatically tunable circular microstrip patch antenna,” *J. Micromechanics Microengineering*, vol. 17, no. 1, p. 1, Nov. 2006, doi: 10.1088/0960-1317/17/1/001.

[12] Xiaoguang Liu, L. P. B. Katehi, W. J. Chappell, and D. Peroulis, “A 3.4 – 6.2 GHz Continuously tunable electrostatic MEMS resonator with quality factor of 460–530,” in *2009 IEEE MTT-S International Microwave Symposium Digest*, Jun. 2009, pp. 1149–1152. doi: 10.1109/MWSYM.2009.5165905.

[13] F. Pistorio, M. M. Saleem, and A. Somà, “A Dual-Mass Resonant MEMS Gyroscope Design with Electrostatic Tuning for Frequency Mismatch Compensation,” *Appl. Sci.*, vol. 11, no. 3, 2021, doi: 10.3390/app11031129.

[14] A. Norouzpour-Shirazi, M. Hodjat-Shamami, R. Tabrizian, and F. Ayazi, “Dynamic tuning of MEMS resonators via electromechanical feedback,” *IEEE Trans. Ultrason. Ferroelectr. Freq. Control*, vol. 62, no. 1, pp. 129–137, Jan. 2015, doi: 10.1109/TUFFC.2014.006570.

[15] B. Yang, L. Wu, C. Lu, and G. Wang, “A Digital Mode-Matching Control System Based on Feedback Calibration for a MEMS Gyroscope,” *J. Sens.*, vol. 2019, p. 9894367, Feb. 2019, doi: 10.1155/2019/9894367.

[16] S. Sonmezoglu, S. E. Alper, and T. Akin, “An Automatically Mode-Matched MEMS Gyroscope With Wide and Tunable Bandwidth,” *J. Microelectromechanical Syst.*, vol. 23, no. 2, pp. 284–297, Apr. 2014, doi: 10.1109/JMEMS.2014.2299234.

[17] Z. X. Hu, B. J. Gallacher, J. S. Burdess, C. P. Fell, and K. Townsend, “Precision mode matching of MEMS gyroscope by feedback control,” in *SENSORS, 2011 IEEE*, Oct. 2011, pp. 16–19. doi: 10.1109/ICSENS.2011.6126998.

[18] M. Heaney, “Electrical Conductivity and Resistivity,” 2003, pp. 7–1 to 7.

[19] K. Shirai, “Temperature Dependence of Young’s Modulus of Silicon,” *Jpn. J. Appl. Phys.*, vol. 52, Aug. 2013, doi: 10.7567/JJAP.52.088002.

[20] G. Liu, F. Yang, X. Bao, and T. Jiang, “Robust Optimization of a MEMS Accelerometer Considering Temperature Variations,” *Sensors*, vol. 15, no. 3, pp. 6342–6359, Mar. 2015, doi: 10.3390/s150306342.

[21] L. Sang *et al.*, “Strain-enhanced high Q-factor GaN micro-electromechanical resonator,” *Sci. Technol. Adv. Mater.*, vol. 21, no. 1, pp. 515–523, Jan. 2020, doi: 10.1080/14686996.2020.1792257.

[22] W. Chen, W. Jia, Y. Xiao, Z. Feng, and G. Wu, “A Temperature-Stable and Low Impedance Piezoelectric MEMS Resonator for Drop-in Replacement of Quartz Crystals,” *IEEE Electron Device Lett.*, vol. 42, no. 9, pp. 1382–1385, Sep. 2021, doi: 10.1109/LED.2021.3094319.

[23] G. Li *et al.*, “Ultra-low thermal expansion coefficient of PZB/β-eucryptite composite glass for MEMS packaging,” *Ceram. Int.*, vol. 46, no. 6, pp. 8385–8390, Apr. 2020, doi: 10.1016/j.ceramint.2019.12.071.

[24] Y. Kim, H. Lee, X. Zhang, and S. Park, “Optimal Material Properties of Molding Compounds for MEMS Package,” *IEEE Trans. Compon. Packag. Manuf. Technol.*, vol. 4, no. 10, pp. 1589–1597, Oct. 2014, doi: 10.1109/TCPMT.2014.2351574.

[25] M. -H. Tsai, Y. -C. Liu, K. -C. Liang, and W. Fang, “Monolithic CMOS—MEMS Pure Oxide Tri-Axis Accelerometers for Temperature Stabilization and Performance Enhancement,” *J. Microelectromechanical Syst.*, vol. 24, no. 6, pp. 1916–1927, Dec. 2015, doi: 10.1109/JMEMS.2015.2452270.

[26] A. Kourani, E. Hegazi, and Y. Ismail, “RF MEMS reference oscillator platform with ±0.5ppm frequency stability for wireless handsets,” in *2015 International Symposium on Signals, Circuits and Systems (ISSCS)*, Jul. 2015, pp. 1–4. doi: 10.1109/ISSCS.2015.7203982.

[27] Y. -C. Liu, M. -H. Tsai, W. -C. Chen, M. -H. Li, S. -S. Li, and W. Fang, “Temperature-Compensated CMOS-MEMS Oxide Resonators,” *J. Microelectromechanical Syst.*, vol. 22, no. 5, pp. 1054–1065, Oct. 2013, doi: 10.1109/JMEMS.2013.2263091.

[28] Z. Wang, Z. Yi, M. Qin, and Q. -A. Huang, “Low-Drift MEMS Thermal Wind Sensor With Symmetric Packaging Using Plastic Injection Molding Process,” *IEEE Trans. Instrum. Meas.*, vol. 70, pp. 1–8, 2021, doi: 10.1109/TIM.2021.3066175.

[29] P. Xu *et al.*, “ZRO Drift Reduction of MEMS Gyroscopes via Internal and Packaging Stress Release,” *Micromachines*, vol. 12, no. 11, 2021, doi: 10.3390/mi12111329.

[30] A. Hajjam, A. Logan, and S. Pourkamali, “Doping-Induced Temperature Compensation of Thermally Actuated High-Frequency Silicon Micromechanical Resonators,” *J. Microelectromechanical Syst.*, vol. 21, no. 3, pp. 681–687, Jun. 2012, doi: 10.1109/JMEMS.2012.2185217.

[31] R. Melamud *et al.*, “Temperature-Insensitive Composite Micromechanical Resonators,” *J. Microelectromechanical Syst.*, vol. 18, no. 6, pp. 1409–1419, Dec. 2009, doi: 10.1109/JMEMS.2009.2030074.

[32] W. Jia, W. Chen, Y. Xiao, Z. Wu, and G. Wu, “A Micro-Oven-Controlled Dual-Mode Piezoelectric MEMS Resonator With ±400 PPB Stability Over −40 to 80 °C Temperature Range,” *IEEE Trans. Electron Devices*, vol. 69, no. 5, pp. 2597–2603, May 2022, doi: 10.1109/TED.2022.3159287.

[33] K. Sundaresan, G. K. Ho, S. Pourkamali, and F. Ayazi, “Electronically Temperature Compensated Silicon Bulk Acoustic Resonator Reference Oscillators,” *IEEE J. Solid-State Circuits*, vol. 42, no. 6, pp. 1425–1434, Jun. 2007, doi: 10.1109/JSSC.2007.896521.

[34] S. -R. Chiu *et al.*, “Active thermal compensation of MEMS based gyroscope,” in *SENSORS, 2012 IEEE*, Oct. 2012, pp. 1–4. doi: 10.1109/ICSENS.2012.6411164.

[35] J. Cui, G. Yan, and Q. Zhao, “Enhanced temperature stability of scale factor in MEMS gyroscope based on multi parameters fusion compensation method,” *Measurement*, vol. 148, p. 106947, Dec. 2019, doi: 10.1016/j.measurement.2019.106947.

[36] G. Wu *et al.*, “Wafer-Level Vacuum-Packaged High-Performance AlN-on-SOI Piezoelectric Resonator for Sub-100-MHz Oscillator Applications,” *IEEE Trans. Ind. Electron.*, vol. 65, no. 4, pp. 3576–3584, Apr. 2018, doi: 10.1109/TIE.2017.2748041.

[37] S. Zaliasl *et al.*, “A 3 ppm 1.5 × 0.8 mm 2 1.0 μA 32.768 kHz MEMS-Based Oscillator,” *IEEE J. Solid-State Circuits*, vol. 50, no. 1, pp. 291–302, Jan. 2015, doi: 10.1109/JSSC.2014.2360377.

[38] Z.-F. Zhou and Q.-A. Huang, “Comprehensive Simulations for Ultraviolet Lithography Process of Thick SU-8 Photoresist,” *Micromachines*, vol. 9, no. 7, 2018, doi: 10.3390/mi9070341.

[39] K. Racka-Szmidt, B. Stonio, J. Żelazko, M. Filipiak, and M. Sochacki, “A Review: Inductively Coupled Plasma Reactive Ion Etching of Silicon Carbide,” *Materials*, vol. 15, no. 1, 2022, doi: 10.3390/ma15010123.

[40] Z. Chen, W. Tian, X. Zhang, and Y. Wang, “Effect of deposition parameters on surface roughness and consequent electromagnetic performance of capacitive RF MEMS switches: a review,” *J. Micromechanics Microengineering*, vol. 27, no. 11, p. 113003, Oct. 2017, doi: 10.1088/1361-6439/aa8917.

[41] I. Kriegel, F. Scotognella, and L. Manna, “Plasmonic doped semiconductor nanocrystals: Properties, fabrication, applications and perspectives,” *Plasmonic Doped Semicond.*

Nanocrystals Prop. Fabr. Appl. Perspect., vol. 674, pp. 1–52, Feb. 2017, doi: 10.1016/j.physrep.2017.01.003.

[42] C. R. Stoldt, C. Carraro, W. R. Ashurst, M. C. Fritz, D. Gao, and R. Maboudian, "Novel Low-Temperature CVD Process for Silicon Carbide MEMS," in *Transducers '01 Eurosensors XV*, E. Obermeier, Ed., Berlin, Heidelberg: Springer Berlin Heidelberg, 2001, pp. 956–959.

[43] G. Samudrala, K. Chakrabarty, P. A. Baker, B. S. Tucker, Y. K. Vohra, and S. A. Catledge, "Selective Deposition of Hard Boron-Carbon Microstructures on Silicon," *Materials*, vol. 14, no. 6, 2021, doi: 10.3390/ma14061397.

[44] C. G. Courcimault and M. G. Allen, "High-Q mechanical tuning of MEMS resonators using a metal deposition -annealing technique," in *The 13th International Conference on Solid-State Sensors, Actuators and Microsystems, 2005. Digest of Technical Papers. TRANSDUCERS '05.*, Jun. 2005, pp. 875-878 Vol. 1. doi: 10.1109/SENSOR.2005.1496557.

[45] J.-O. Carlsson and P. M. Martin, "Chapter 7 - Chemical Vapor Deposition," in *Handbook of Deposition Technologies for Films and Coatings (Third Edition)*, P. M. Martin, Ed., Boston: William Andrew Publishing, 2010, pp. 314–363. doi: 10.1016/B978-0-8155-2031-3.00007-7.

[46] Z. Li and H. Li, "A New Type of Resonator Designed for Plasma Chemical Vapor Deposition," *Appl. Mech. Mater.*, vol. 121–126, Oct. 2011, doi: 10.4028/www.scientific.net/AMM.121-126.642.

[47] D. M. Mattox, "Physical vapor deposition (PVD) processes," *Met. Finish.*, vol. 100, pp. 394–408, Jan. 2002, doi: 10.1016/S0026-0576(02)82043-8.

[48] A. Baptista, F. Silva, J. Porteiro, J. Míguez, and G. Pinto, “Sputtering Physical Vapour Deposition (PVD) Coatings: A Critical Review on Process Improvement and Market Trend Demands,” *Coatings*, vol. 8, no. 11, 2018, doi: 10.3390/coatings8110402.

[49] J. Singh and D. E. Wolfe, “Review Nano and macro-structured component fabrication by electron beam-physical vapor deposition (EB-PVD),” *J. Mater. Sci.*, vol. 40, no. 1, pp. 1–26, Jan. 2005, doi: 10.1007/s10853-005-5682-5.

[50] D. Zhan *et al.*, “Confined Chemical Etching for Electrochemical Machining with Nanoscale Accuracy,” *Acc. Chem. Res.*, vol. 49, no. 11, pp. 2596–2604, Nov. 2016, doi: 10.1021/acs.accounts.6b00336.

[51] N. Soin and Burhanudin Y. Majlis, “KOH etching process of perfect square MEMS corrugated diaphragm,” presented at the Proc.SPIE, Jan. 2006, p. 60371Z. doi: 10.1117/12.637586.

[52] Meltem Erdamar, Karthikeyan Shanmugasundaram, Paul Roman, Paul Mumbauer, Maria Klimkiewicz, and Jerzy Ruzyllo, “Deep lateral anhydrous HF/methanol etching for MEMS release processes,” *J. MicroNanolithography MEMS MOEMS*, vol. 7, no. 3, p. 033014, Jul. 2008, doi: 10.1117/1.2959177.

[53] A. Ababneh, H. Kreher, and U. Schmid, “Etching behaviour of sputter-deposited aluminium nitride thin films in H3PO4 and KOH solutions,” *Microsyst. Technol.*, vol. 14, no. 4, pp. 567–573, Apr. 2008, doi: 10.1007/s00542-007-0450-x.

[54] Y. Tao, Y. Pan, S. Jin, Y. Jia, K. Yang, and H. Luo, “Trimming of Imperfect Cylindrical Fused Silica Resonators by Chemical Etching,” *Sensors*, vol. 19, no. 16, p. 3596, Aug. 2019, doi: 10.3390/s19163596.

[55] E. S. Hung and S. D. Senturia, “Extending the travel range of analog-tuned electrostatic actuators,” *J. Microelectromechanical Syst.*, vol. 8, no. 4, pp. 497–505, Dec. 1999, doi: 10.1109/84.809065.

[56] S G Adams, F M Bertsch, K A Shaw, P G Hartwell, F C Moon, and N C MacDonald, “Capacitance based tunable resonators,” *J. Micromechanics Microengineering*, vol. 8, no. 1, p. 15, Mar. 1998, doi: 10.1088/0960-1317/8/1/003.

[57] D. A. Horsley, R. Horowitz, and A. P. Pisano, “Microfabricated electrostatic actuators for hard disk drives,” *IEEEASME Trans. Mechatron.*, vol. 3, no. 3, pp. 175–183, Sep. 1998, doi: 10.1109/3516.712113.

[58] H. Torun, K. K. Sarangapani, and F. L. Degertekin, “Spring constant tuning of active atomic force microscope probes using electrostatic spring softening effect,” *Appl. Phys. Lett.*, vol. 91, no. 25, p. 253113, Dec. 2007, doi: 10.1063/1.2827190.

[59] K. Schwab, “Spring constant and damping constant tuning of nanomechanical resonators using a single-electron transistor,” *Appl. Phys. Lett.*, vol. 80, no. 7, pp. 1276–1278, Feb. 2002, doi: 10.1063/1.1449533.

[60] I. Y. Park, C. W. Lee, H. S. Jang, Y. S. Oh, and B. J. Ha, “Capacitive sensing type surface micromachined silicon accelerometer with a stiffness tuning capability,” in *Proceedings MEMS 98. IEEE. Eleventh Annual International Workshop on Micro Electro Mechanical Systems. An Investigation of Micro Structures, Sensors, Actuators, Machines and Systems (Cat. No.98CH36176*, Jan. 1998, pp. 637–642. doi: 10.1109/MEMSYS.1998.659832.

[61] B. Krijnen and D. M. Brouwer, “Flexures for large stroke electrostatic actuation in MEMS,” *J. Micromechanics Microengineering*, vol. 24, no. 1, p. 015006, Nov. 2013, doi: 10.1088/0960-1317/24/1/015006.

[62] C. Guo and G. K. Fedder, “A quadratic-shaped-finger comb parametric resonator,” *J. Micromechanics Microengineering*, vol. 23, no. 9, p. 095007, Aug. 2013, doi: 10.1088/0960-1317/23/9/095007.

[63] B. Borovic, A. Q. Liu, D. Popa, H. Cai, and F. L. Lewis, “Open-loop versus closed-loop control of MEMS devices: choices and issues,” *J. Micromechanics Microengineering*, vol. 15, no. 10, p. 1917, Aug. 2005, doi: 10.1088/0960-1317/15/10/018.

[64] D. Zhu, M. J. Tudor, and S. P. Beeby, “Strategies for increasing the operating frequency range of vibration energy harvesters: a review,” *Meas. Sci. Technol.*, vol. 21, no. 2, p. 022001, Dec. 2009, doi: 10.1088/0957-0233/21/2/022001.

[65] J.-C. Chiou, L.-J. Shieh, and Y.-J. Lin, “CMOS-MEMS prestress vertical cantilever resonator with electrostatic driving and piezoresistive sensing,” *J. Phys. Appl. Phys.*, vol. 41, no. 20, p. 205102, Sep. 2008, doi: 10.1088/0022-3727/41/20/205102.

[66] P.-H. Kao, C.-L. Dai, C.-C. Hsu, and C.-C. Wu, “Manufacture of Micromirror Arrays Using a CMOS-MEMS Technique,” *Sensors*, vol. 9, no. 8, pp. 6219–6231, 2009, doi: 10.3390/s90806219.

[67] K. B. Lee and Y.-H. Cho, “A triangular electrostatic comb array for micromechanical resonant frequency tuning,” *Sens. Actuators Phys.*, vol. 70, no. 1, pp. 112–117, Oct. 1998, doi: 10.1016/S0924-4247(98)00122-8.

[68] B. Morgan and R. Ghodssi, “Vertically-Shaped Tunable MEMS Resonators,” *J. Microelectromechanical Syst.*, vol. 17, no. 1, pp. 85–92, Feb. 2008, doi: 10.1109/JMEMS.2007.910251.

[69] S. G. Adams, F. M. Bertsch, K. A. Shaw, P. G. Hartwell, N. C. MacDonald, and F. C. Moon, “Capacitance Based Tunable Micromechanical Resonators,” in *Proceedings of the*

International Solid-State Sensors and Actuators Conference - TRANSDUCERS '95, Jun. 1995, pp. 438–441. doi: 10.1109/SENSOR.1995.717233.

[70] S. Sonmezoglu, S. E. Alper, and T. Akin, "An Automatically Mode-Matched MEMS Gyroscope With Wide and Tunable Bandwidth," *J. Microelectromechanical Syst.*, vol. 23, no. 2, pp. 284–297, Apr. 2014, doi: 10.1109/JMEMS.2014.2299234.

[71] J. He, J. Xie, X. He, L. Du, and W. Zhou, "Analytical study and compensation for temperature drifts of a bulk silicon MEMS capacitive accelerometer," *Sens. Actuators Phys.*, vol. 239, pp. 174–184, Mar. 2016, doi: 10.1016/j.sna.2016.01.026.

[72] L. Chen *et al.*, "A Temperature Drift Suppression Method of Mode-Matched MEMS Gyroscope Based on a Combination of Mode Reversal and Multiple Regression," *Micromachines*, vol. 13, no. 10, 2022, doi: 10.3390/mi13101557.

[73] E. Courjon, S. Ballandras, W. Daniau, T. Baron, J. B. Moulet, and T. Signamarcheix, "LiTaO3/silicon composite wafers for the fabrication of low loss low TCF high coupling resonators for filter applications," in *2015 Joint IEEE International Symposium on the Applications of Ferroelectric (ISAF), International Symposium on Integrated Functionalities (ISIF), and Piezoelectric Force Microscopy Workshop (PFM)*, May 2015, pp. 215–217. doi: 10.1109/ISAF.2015.7172709.

[74] D. Petit *et al.*, "Thermally stable oscillator at 2.5 GHz using temperature compensated BAW resonator and its integrated temperature sensor," in *2008 IEEE Ultrasonics Symposium*, Nov. 2008, pp. 895–898. doi: 10.1109/ULTSYM.2008.0216.

[75] V. Yantchev *et al.*, "Parametric study of resonant TC-SAW piston-mode configurations," in *2017 IEEE International Ultrasonics Symposium (IUS)*, Sep. 2017, pp. 1–4. doi: 10.1109/ULTSYM.2017.8091695.

[76] R. Tabrizian, M. Pardo, and F. Ayazi, “A 27 MHz temperature compensated MEMS oscillator with sub-ppm instability,” in *2012 IEEE 25th International Conference on Micro Electro Mechanical Systems (MEMS)*, Feb. 2012, pp. 23–26. doi: 10.1109/MEMSYS.2012.6170084.

[77] H. Zhang, X. Wei, Y. Gao, and E. Cretu, “Frequency characteristics and thermal compensation of MEMS devices based on geometric anti-spring,” *J. Micromechanics Microengineering*, vol. 30, no. 8, p. 085014, Jun. 2020, doi: 10.1088/1361-6439/ab9203.

[78] H. Zhang, X. Wei, Y. Gao, and E. Cretu, “Analytical Study and Thermal Compensation for Capacitive MEMS Accelerometer With Anti-Spring Structure,” *J. Microelectromechanical Syst.*, vol. 29, no. 5, pp. 1389–1400, Oct. 2020, doi: 10.1109/JMEMS.2020.3011949.

[79] J. He, W. Zhou, H. Yu, X. He, and P. Peng, “Structural Designing of a MEMS Capacitive Accelerometer for Low Temperature Coefficient and High Linearity,” *Sensors*, vol. 18, no. 2, 2018, doi: 10.3390/s18020643.

[80] Kyung Il Lee, H. Takao, K. Sawada, and M. Ishida, “Analysis and experimental verification of thermal drift in a constant temperature control type three-axis accelerometer for high temperatures with a novel composition of Wheatstone bridge,” in *17th IEEE International Conference on Micro Electro Mechanical Systems. Maastricht MEMS 2004 Technical Digest*, Jan. 2004, pp. 241–244. doi: 10.1109/MEMS.2004.1290567.

[81] J. Zhou, A. -p. Qiu, Y. Zhao, G. -m. Xia, X. -h. Yu, and Z. -h. Xue, “Thermal drift optimization for silicon microgyroscope,” in *2016 IEEE SENSORS*, Nov. 2016, pp. 1–3. doi: 10.1109/ICSENS.2016.7808716.

[82] Y. Mo, J. Yang, B. Peng, G. Xie, and B. Tang, “Design and verification of a structure for isolating stress in sandwich MEMS accelerometer,” *Microsyst. Technol.*, vol. 27, no. 5, pp. 1943–1950, May 2021, doi: 10.1007/s00542-020-04980-w.

[83] B. Kim *et al.*, “Using MEMS to Build the Device and the Package,” in *TRANSDUCERS 2007 - 2007 International Solid-State Sensors, Actuators and Microsystems Conference*, Jun. 2007, pp. 331–334. doi: 10.1109/SENSOR.2007.4300135.

[84] J. Chen, Q. Lu, J. Bai, X. Xu, Y. Yao, and W. Fang, “A Temperature Control Method for Microaccelerometer Chips Based on Genetic Algorithm and Fuzzy PID Control,” *Micromachines*, vol. 12, no. 12, 2021, doi: 10.3390/mi12121511.

[85] P. Peng, W. Zhou, H. Yu, B. Peng, H. Qu, and X. He, “Investigation of the Thermal Drift of MEMS Capacitive Accelerometers Induced by the Overflow of Die Attachment Adhesive,” *IEEE Trans. Compon. Packag. Manuf. Technol.*, vol. 6, no. 5, pp. 822–830, May 2016, doi: 10.1109/TCPMT.2016.2521934.

[86] Y. Wang *et al.*, “A zero TCF band 13 SAW duplexer,” in *2015 IEEE International Ultrasonics Symposium (IUS)*, Oct. 2015, pp. 1–4. doi: 10.1109/ULTSYM.2015.0092.

[87] Z. Wang, Z. Yi, M. Qin, and Q. -A. Huang, “Low-Drift MEMS Thermal Wind Sensor With Symmetric Packaging Using Plastic Injection Molding Process,” *IEEE Trans. Instrum. Meas.*, vol. 70, pp. 1–8, 2021, doi: 10.1109/TIM.2021.3066175.

[88] L. L. Mercado, Tien-Yu Tom Lee, Shun-Meen Kuo, V. Hause, and C. Amrine, “Thermal solutions for discrete and wafer-level RF MEMS switch packages,” *IEEE Trans. Adv. Packag.*, vol. 26, no. 3, pp. 318–326, Aug. 2003, doi: 10.1109/TADVP.2003.817962.

[89] Y. Wang, R. Cao, C. Li, and R. N. Dean, “Concepts, Roadmaps and Challenges of Ovenized MEMS Gyroscopes: A Review,” *IEEE Sens. J.*, vol. 21, no. 1, pp. 92–119, Jan. 2021, doi: 10.1109/JSEN.2020.3012484.

[90] R. L. Kubena *et al.*, “Co-integration of a quartz OCXO and Si MEMS inertial sensors for improved navigational accuracy,” in *2016 IEEE International Frequency Control Symposium (IFCS)*, May 2016, pp. 1–6. doi: 10.1109/FCS.2016.7563590.

[91] L. C. Ortiz *et al.*, “Thermal effects of ovenized clocks on episeal encapsulated inertial measurement units,” in *2018 IEEE Micro Electro Mechanical Systems (MEMS)*, Jan. 2018, pp. 980–983. doi: 10.1109/MEMSYS.2018.8346722.

[92] A. Mahmoud, T. Mukherjee, and G. Piazza, “Investigating Long-Term Stability of Wide Bandwidth Surface Acoustic Waves Gyroscopes Using a Monolithically Integrated Micro-Oven,” in *2020 IEEE 33rd International Conference on Micro Electro Mechanical Systems (MEMS)*, Jan. 2020, pp. 252–254. doi: 10.1109/MEMS46641.2020.9056180.

[93] M. Li *et al.*, “Temperature Bias Drift Phase-Based Compensation for a MEMS Accelerometer with Stiffness-Tuning Double-Sided Parallel Plate Capacitors,” *Nanomanufacturing Metrol.*, vol. 6, no. 1, p. 22, Jun. 2023, doi: 10.1007/s41871-023-00202-9.

[94] T. Zhang, Z. Ma, Y. Jin, Z. Ye, X. Zheng, and Z. Jin, “Temperature drift compensation of a tuned low stiffness MEMS accelerometer based on double-sided parallel plates,” in *2022 IEEE 17th International Conference on Nano/Micro Engineered and Molecular Systems (NEMS)*, Apr. 2022, pp. 249–252. doi: 10.1109/NEMS54180.2022.9791155.

[95] R. Fontanella, D. Accardo, E. Caricati, S. Cimmino, and D. De Simone, “An extensive analysis for the use of back propagation neural networks to perform the calibration of

MEMS gyro bias thermal drift," in *2016 IEEE/ION Position, Location and Navigation Symposium (PLANS)*, Apr. 2016, pp. 672–680. doi: 10.1109/PLANS.2016.7479760.

[96] T. Zhang, Z. Ma, Y. Jin, Z. Ye, X. Zheng, and Z. Jin, "A Stiffness-tunable MEMS Accelerometer with In-operation Drift Compensation," in *2022 IEEE International Conference on Manipulation, Manufacturing and Measurement on the Nanoscale (3M-NANO)*, Aug. 2022, pp. 113–116. doi: 10.1109/3M-NANO56083.2022.9941622.

[97] Y. Zhai, T. Xu, G. Xu, X. Cao, C. Yang, and H. Li, "Improvement and compensation of temperature drift of scale factor of a SOI-based MEMS differential capacitive accelerometer," *Meas. Sci. Technol.*, vol. 34, no. 8, p. 085113, May 2023, doi: 10.1088/1361-6501/acc9d8.

[98] M. Zhu *et al.*, "Temperature Drift Compensation for High-G MEMS Accelerometer Based on RBF NN Improved Method," *Appl. Sci.*, vol. 9, no. 4, 2019, doi: 10.3390/app9040695.

[99] Y. Feng, X. Li, and X. Zhang, "An Adaptive Compensation Algorithm for Temperature Drift of Micro-Electro-Mechanical Systems Gyroscopes Using a Strong Tracking Kalman Filter," *Sensors*, vol. 15, no. 5, pp. 11222–11238, 2015, doi: 10.3390/s150511222.

[100] B. Qi, S. Shi, L. Zhao, and J. Cheng, "A Novel Temperature Drift Error Precise Estimation Model for MEMS Accelerometers Using Microstructure Thermal Analysis," *Micromachines*, vol. 13, no. 6, 2022, doi: 10.3390/mi13060835.

[101] S. Chong *et al.*, "Temperature drift modeling of MEMS gyroscope based on genetic-Elman neural network," *Mech. Syst. Signal Process.*, vol. 72–73, pp. 897–905, May 2016, doi: 10.1016/j.ymssp.2015.11.004.

[102] D. Yang, J. Woo, S. Lee, J. Mitchell, A. D. Challoner, and K. Najafi, “A Micro Oven-Control System for Inertial Sensors,” *J. Microelectromechanical Syst.*, vol. 26, no. 3, pp. 507–518, Jun. 2017, doi: 10.1109/JMEMS.2017.2692770.

[103] M. -H. Li, C. -Y. Chen, C. -S. Li, C. -H. Chin, and S. -S. Li, “A Monolithic CMOS-MEMS Oscillator Based on an Ultra-Low-Power Ovenized Micromechanical Resonator,” *J. Microelectromechanical Syst.*, vol. 24, no. 2, pp. 360–372, Apr. 2015, doi: 10.1109/JMEMS.2014.2331497.

[104] J. Clark, O. Misiats, and S. Sayed, “Electrical Control of Effective Mass, Damping, and Stiffness of MEMS Devices,” *IEEE Sens. J.*, vol. PP, pp. 1–1, Dec. 2016, doi: 10.1109/JSEN.2016.2640290.

[105] S. H. Ahmed, S. Hussain, S. Rehman, S. K. Abbas, and S. A. Sheikh, “Stability analysis of forced duffing oscillator (FDO),” in *2016 19th International Conference on Computer and Information Technology (ICCIT)*, Dec. 2016, pp. 145–149. doi: 10.1109/ICCITECHN.2016.7860185.

[106] J. Liu *et al.*, “Consideration of Thermo-Vacuum Stability of a MEMS Gyroscope for Space Applications,” *Sensors*, vol. 20, no. 24, 2020, doi: 10.3390/s20247172.

[107] V. M. N. Passaro, A. Cuccovillo, L. Vaiani, M. De Carlo, and C. E. Campanella, “Gyroscope Technology and Applications: A Review in the Industrial Perspective,” *Sensors*, vol. 17, no. 10, 2017, doi: 10.3390/s17102284.

[108] C. Acar, A. R. Schofield, A. A. Trusov, L. E. Costlow, and A. M. Shkel, “Environmentally Robust MEMS Vibratory Gyroscopes for Automotive Applications,” *IEEE Sens. J.*, vol. 9, no. 12, pp. 1895–1906, Dec. 2009, doi: 10.1109/JSEN.2009.2026466.

[109] Z. Xinfeng, F. Jingjing, L. Zhipeng, and Z. Mengtong, “MEMS Gyroscopes Development and Application Overview on Intelligent Vehicles,” in *2020 Chinese Control And Decision Conference (CCDC)*, Aug. 2020, pp. 53–59. doi: 10.1109/CCDC49329.2020.9164093.

[110] Rui Guan, Chunhua He, D. Liu, Q. Zhao, Z. Yang, and G. Yan, “A temperature control system used for improving resonant frequency drift of MEMS gyroscopes,” in *10th IEEE International Conference on Nano/Micro Engineered and Molecular Systems*, Apr. 2015, pp. 397–400. doi: 10.1109/NEMS.2015.7147452.

[111] I. P. Prikhodko, A. A. Trusov, and A. M. Shkel, “Compensation of drifts in high-Q MEMS gyroscopes using temperature self-sensing,” *Sens. Actuators Phys.*, vol. 201, pp. 517–524, Oct. 2013, doi: 10.1016/j.sna.2012.12.024.

[112] I. P. Prikhodko, B. R. Simon, G. Sharma, S. A. Zotov, A. A. Trusov, and A. M. Shkel, “High and Moderate-Level Vacuum Packaging of Vibratory MEMS,” *Int. Symp. Microelectron.*, vol. 2013, no. 1, pp. 000705–000710, Jan. 2013, doi: 10.4071/isom-2013-WP42.

[113] X. Wang and H. Cao, “Temperature drift modeling and compensation of micro-electro-mechanical system gyroscope based on improved support vector machine algorithms,” *Int. J. Distrib. Sens. Netw.*, vol. 16, no. 3, p. 1550147720908195, Mar. 2020, doi: 10.1177/1550147720908195.

[114] S. Kaji *et al.*, “A <100 PPB/K Frequency-Matching Temperature Stability MEMS Rate Integrating Gyroscope Enabled by Donut-Mass Structure,” in *2020 IEEE 33rd International Conference on Micro Electro Mechanical Systems (MEMS)*, Jan. 2020, pp. 263–266. doi: 10.1109/MEMS46641.2020.9056333.

[115] S. E. Alper and T. Akin, “A single-crystal silicon symmetrical and decoupled MEMS gyroscope on an insulating substrate,” *J. Microelectromechanical Syst.*, vol. 14, no. 4, pp. 707–717, Aug. 2005, doi: 10.1109/JMEMS.2005.845400.

[116] D. Lemmerhirt *et al.*, “Improved Scale-Factor and Bias Stability of Ovenized Inertial Sensors in an Environmentally-Stabilized Inertial Measurement Unit (eIMU),” in *2019 IEEE International Symposium on Inertial Sensors and Systems (INERTIAL)*, Apr. 2019, pp. 1–4. doi: 10.1109/ISISS.2019.8739649.

[117] J. Jia, X. Ding, Y. Gao, and H. Li, “Automatic Frequency Tuning Technology for Dual-Mass MEMS Gyroscope Based on a Quadrature Modulation Signal,” *Micromachines*, vol. 9, no. 10, 2018, doi: 10.3390/mi9100511.

[118] D. Keymeulen *et al.*, “Tuning of MEMS devices using evolutionary computation and open-loop frequency response,” presented at the 2005 IEEE Aerospace Conference, IEEE, 2005, pp. 1–8.

[119] D. Kim and R. M’Closkey, “Real-time tuning of MEMS gyro dynamics,” presented at the Proceedings of the 2005, American Control Conference, 2005., IEEE, 2005, pp. 3598–3603.

[120] C. C. Painter and A. M. Shkel, “Active structural error suppression in MEMS vibratory rate integrating gyroscopes,” *IEEE Sens. J.*, vol. 3, no. 5, pp. 595–606, 2003.

[121] S. Park, R. Horowitz, S. K. Hong, and Y. Nam, “Trajectory-switching algorithm for a MEMS gyroscope,” *IEEE Trans. Instrum. Meas.*, vol. 56, no. 6, pp. 2561–2569, 2007.

[122] C. He *et al.*, “A MEMS vibratory gyroscope with real-time mode-matching and robust control for the sense mode,” *IEEE Sens. J.*, vol. 15, no. 4, pp. 2069–2077, 2014.

[123] X. Wang, Y. Zhang, C. Yang, and H. Li, “Analysis and experiment of drive mode of silicon micro-gyroscope based on digital phased-locked loop control,” *Dongnan Daxue Xuebao Ziran Kexue BanJournal Southeast Univ. Nat. Sci. Ed.*, vol. 43, pp. 747–752, Jul. 2013, doi: 10.3969/j.issn.1001-0505.2013.04.014.

[124] C. Li, B. Yang, X. Guo, and L. Wu, “A Digital Calibration Technique of MEMS Gyroscope for Closed-Loop Mode-Matching Control,” *Micromachines*, vol. 10, no. 8, 2019, doi: 10.3390/mi10080496.

[125] B. J. Gallacher, J. Hedley, J. S. Burdess, A. J. Harris, and M. E. McNie, “Multimodal tuning of a vibrating ring using laser ablation,” *Proc. Inst. Mech. Eng. Part C J. Mech. Eng. Sci.*, vol. 217, no. 5, pp. 557–576, May 2003, doi: 10.1243/095440603765226858.

[126] C. H. Ahn *et al.*, “Geometric compensation of (100) single crystal silicon disk resonating gyroscope for mode-matching,” in *2013 Transducers & Eurosensors XXVII: The 17th International Conference on Solid-State Sensors, Actuators and Microsystems (TRANSDUCERS & EUROSENSORS XXVII)*, Jun. 2013, pp. 1723–1726. doi: 10.1109/Transducers.2013.6627119.

[127] J. Giner, D. Maeda, K. Ono, A. M. Shkel, and T. Sekiguchi, “MEMS Gyroscope With Concentrated Springs Suspensions Demonstrating Single Digit Frequency Split and Temperature Robustness,” *J. Microelectromechanical Syst.*, vol. 28, no. 1, pp. 25–35, Feb. 2019, doi: 10.1109/JMEMS.2018.2881209.

[128] X. Ding, Z. Ruan, J. Jia, L. Huang, H. Li, and L. Zhao, “In-Run Mode-Matching of MEMS Gyroscopes Based on Power Symmetry of Readout Signal in Sense Mode,” *IEEE Sens. J.*, vol. 21, no. 21, pp. 23806–23817, Nov. 2021, doi: 10.1109/JSEN.2021.3112915.

[129] Y. Zhou, J. Ren, M. Liu, T. Zhou, and Y. Su, “An In-Run Automatic Mode-Matching Method for N = 3 MEMS Disk Resonator Gyroscope,” *IEEE Sens. J.*, vol. 21, no. 24, pp. 27601–27611, Dec. 2021, doi: 10.1109/JSEN.2021.3126321.

[130] C. Li *et al.*, “An FPGA-Based Interface System for High-Frequency Bulk-Acoustic-Wave Microgyroscopes With In-Run Automatic Mode-Matching,” *IEEE Trans. Instrum. Meas.*, vol. 69, no. 4, pp. 1783–1793, Apr. 2020, doi: 10.1109/TIM.2019.2914295.

[131] S. Sung, W. -T. Sung, C. Kim, S. Yun, and Y. J. Lee, “On the Mode-Matched Control of MEMS Vibratory Gyroscope via Phase-Domain Analysis and Design,” *IEEEASME Trans. Mechatron.*, vol. 14, no. 4, pp. 446–455, Aug. 2009, doi: 10.1109/TMECH.2009.2023985.

[132] F. Yesil, S. E. Alper, and T. Akin, “An automatic mode matching system for a high Q-factor MEMS gyroscope using a decoupled perturbation signal,” in *2015 Transducers - 2015 18th International Conference on Solid-State Sensors, Actuators and Microsystems (TRANSDUCERS)*, Jun. 2015, pp. 1148–1151. doi: 10.1109/TRANSDUCERS.2015.7181131.

[133] N. G. Sharma, T. Sundararajan, and S. S. Gautam, “Identification of limiting damping mechanisms in a high quality factor hybrid resonator of space application gyroscope,” *Adv. Space Res.*, vol. 69, no. 3, pp. 1662–1679, Feb. 2022, doi: 10.1016/j.asr.2021.11.031.

[134] W. Zhao, Y. Rong, C. Li, Y. Wang, X. Cai, and X. Yu, “High Precision Hemispherical Resonator Gyroscopes With Oven Control Systems,” *IEEE Sens. J.*, vol. 21, no. 6, pp. 7388–7401, Mar. 2021, doi: 10.1109/JSEN.2021.3050206.

[135] W. Zhao, H. Yang, L. Song, X. Yu, F. Liu, and Y. Su, “Researched on the bias stability of the HRG affected by the temperature and the standing wave azimuth,” *Meas. Control*, vol. 53, no. 9–10, pp. 1730–1738, Nov. 2020, doi: 10.1177/0020294020952465.

[136] W. Liang *et al.*, “Whispering gallery mode optical gyroscope,” in *2016 IEEE International Symposium on Inertial Sensors and Systems*, Feb. 2016, pp. 89–92. doi: 10.1109/ISISS.2016.7435552.

[137] Y. V. Filatov, A. S. Kukaev, E. V. Shalymov, and V. Y. Venediktov, “Future gyros on the base of whispering gallery mode resonators,” in *2017 Progress In Electromagnetics Research Symposium - Spring (PIERS)*, May 2017, pp. 3085–3089. doi: 10.1109/PIERS.2017.8262285.

[138] T. Amrane, J. Jager, T. Jager, V. Calvo, and J. Leger, “TOWARDS A FULLY INTEGRATED OPTICAL GYROSCOPE USING WHISPERING GALLERY MODES RESONATORS,” presented at the INTERNATIONAL CONFERENCE ON SPACE OPTICS-ICSO 2014, Z. Sodnik, B. Cugny, and N. Karafolas, Eds., 2014. doi: 10.1117/12.2304206.

[139] A. B. Matsko, W. Liang, A. A. Savchenkov, V. S. Ilchenko, and L. Maleki, “Fundamental limitations of sensitivity of whispering gallery mode gyroscopes,” *Spec. Issue Mem. Profr. VB Braginsky*, vol. 382, no. 33, pp. 2289–2295, Aug. 2018, doi: 10.1016/j.physleta.2017.09.028.

[140] J. Clark, “Self-Calibration and Performance Control of MEMS with Applications for IoT,” *Sensors*, vol. 18, no. 12, 2018, doi: 10.3390/s18124411.